

THESIS

DIAGNOSTICS AND CHARACTERIZATION OF DIRECT INJECTION OF LIQUIFIED  
PETROLEUM GAS FOR DEVELOPMENT OF SPRAY MODELS AT ENGINE-LIKE CONDITIONS

Submitted by

Manav Sharma

Department of Mechanical Engineering

In partial fulfillment of the requirements

For the Degree of Master of Science

Colorado State University

Fort Collins, Colorado

Fall 2023

Master's Committee:

Advisor: Bret Windom

Azer Yalin  
Dylan Yost

Copyright by Manav Sharma 2023

All Rights Reserved

## ABSTRACT

### DIAGNOSTICS AND CHARACTERIZATION OF DIRECT INJECTION OF LIQUIFIED PETROLEUM GAS FOR DEVELOPMENT OF SPRAY MODELS AT ENGINE-LIKE CONDITIONS

Research within the realm of internal combustion (IC) engines is concentrated on enhancing fuel efficiency and curbing tailpipe emissions, particularly CO<sub>2</sub> and regulated pollutants. Promising solutions encompass the utilization of direct injection (DI) and alternative fuels, with liquefied petroleum gas (LPG) standing out as a notable candidate. LPG presents a pragmatic and economical option for fueling the heavy-duty transportation sector in the United States. However, widespread adoption hinges on achieving energy conversion efficiencies in LPG engines comparable to those in diesel engine platforms.

The overarching goal of this research is to address fundamental limitations to achieving or surpassing near-diesel efficiencies in heavy-duty on-road liquefied petroleum gas engines. Owing to substantial differences in physical properties compared to traditional fuels, an enhanced understanding and modeling of LPG sprays become imperative.

This work conducts an experimental and numerical analysis of direct-injected propane and iso-octane, serving as surrogates for LPG and gasoline, respectively, under diverse engine-like conditions. The overall objective is to establish a baseline for the fuel delivery system required in future high-efficiency DI-LPG heavy-duty engines. Propane, emulating LPG, undergoes injection across various engine-like conditions, encompassing early and late injections, as well as boosted engines, using a range of direct injectors available in both research and commercial domains. Optical diagnostics, including high-speed schlieren and planar Mie scattering imaging, were performed to study the spray penetration, liquid and vapor phase regions, and mixing of propane and to characterize bulk and the plume-specific spray behavior of propane. The study also investigates the influence of injector geometry on spray performance.

Iso-octane was used as a surrogate for gasoline, and propane was used to compare LPG's behavior with more conventional DI fuel. The experimental results and high-fidelity internal nozzle-flow simulations

were then used to define best practices in computational fluid dynamics (CFD) Lagrangian spray models. Optical imaging revealed that, unlike iso-octane, propane's spray propagation was fed by its flash boiling, spray collapse, and a high degree of vaporization, resulting in a direct proportionality of propane's penetration length to temperature. These unique attributes categorize propane as an unconventional spray, necessitating corrections to injection and breakup models to replicate under-expanded jet dynamics and emulate flash boiling-driven spray development across various research and commercial injectors.

## ACKNOWLEDGMENTS

I express my profound gratitude to my advisor, Dr. Bret Windom, for his unwavering support across academic, professional, and personal domains, particularly during challenging periods. His confidence in my abilities and intellectual guidance have profoundly shaped my identity as an academic and researcher. Throughout our collaboration, I have not only matured as an engineer but also gained invaluable insights into various facets of life. Dr. Windom serves as an enduring role model, inspiring me to maximize opportunities and grow from diverse experiences.

I also acknowledge Dr. Azer Yalin and Dr. Dylan Yost for their commitment to serving on my committee and providing invaluable guidance throughout my research. The depth of knowledge acquired from them in Laser Physics and Diagnostics has significantly enriched my academic journey, and their constructive feedback has substantially enhanced the quality of this document. Dr. Daniel Olsen and Dr. Ciprian Dumitache merit acknowledgment for their support in the research project and facilitation of my academic success.

Special appreciation goes to Dr. Lorenzo Nocivelli and Dr. Katherine Asztalos at Argonne National Lab for their collaborative efforts on this project. Their diligent work on the spray models has paved the way for the development of a high-efficiency engine, and I am grateful for their contribution to the success of my research.

The completion of my degree, including defending and writing my thesis, was a formidable journey, and I am indebted to my friends Miguel Valles Castro, Jake Kolb, Arturo Eduardo Reinaldo Quintero Castillo, Dr. Siddhesh Bhoite, Bilal Khan, and Harvinder Singh Virk for their unwavering support, accountability, and guidance in finding the right balance to successfully conclude my Master's degree.

The lab, particularly Powerhouse, became a second home during my academic pursuit, with coworkers evolving into a supportive family. I extend gratitude to the Chemical Energy Conversion Laboratory group, as well as other students at Powerhouse, including Colin Slunecka, Toluwalase Fosudo, Andrew Zdanowicz, Reece Churchill, Niko Landin, Dr. Diego Bestel, and Parneeth Lokini, for engaging

in intellectually stimulating conversations. I thank my fellow lab mates, Brye Windell, Anthony Adam Graves, Alex Leuker, Andrew Zdanowicz, Iris Kessler, and Reece Churchill, for assisting in data collection, collaborative research, and providing valuable insights. The camaraderie and support within the lab have truly fostered a sense of belonging. Special appreciation goes to Erin Kelley, Mark James, and Kirk Evans for their prompt and comprehensive assistance with unconventional requests for my research.

Gratitude is also extended to Dr. Eleana Estanol, Dr. Schatte, Dr. Hoenig, Michael, David Youngs, and Cyndy for their guidance in maintaining equilibrium between academic pursuits and overall well-being. Thanks to Amanda Lager Gleason, CSU Mechanical Engineering Department, and CSU Health Network for pivotal roles in helping me achieve my goals and offering support when needed the most.

My parents, Sanjay Sharma and Neelam Sharma, deserve heartfelt appreciation for unwavering mental, emotional, and financial support throughout my academic journey. Their belief in my potential as a researcher and academic has been a constant source of motivation to strive for excellence. I extend thanks to my sisters and friends, Deepika Sharma and Ayushi Sharma, for their continual support and readiness to assist whenever needed. Gratitude is extended to my non-human companions, including my dog Blacky for companionship and tolerating my attempts to teach him about my research and wave optics, the Nd:YAG laser for working day and night and becoming a constant focus of care and attention just like a baby, and the powerhouse.

Finally, my deepest appreciation goes to my Maa for her unconditional love and unwavering faith in my abilities, which have been a cornerstone of my academic achievements.

## DEDICATION

*“To my beloved Maa, whose enduring memories are eternally cherished. And to my parents whose hard work laid the foundation of my success.”*

## TABLE OF CONTENTS

<b>ABSTRACT .....</b>	<b>ii</b>
<b>ACKNOWLEDGMENTS .....</b>	<b>iv</b>
<b>DEDICATION .....</b>	<b>vi</b>
<b>CHAPTER 1 - Introduction .....</b>	<b>1</b>
1.1. Significance .....	1
1.2. Background .....	2
1.2.1. Liquid Petroleum Gas as an Alternative Fuel .....	2
1.2.2. Injection Techniques .....	3
1.2.3. Direct Injection Methodologies .....	4
1.2.4. Injection Regimes .....	5
1.2.4.1. Conventional injection regime .....	6
1.2.4.2. Flash-boiling injection regime .....	7
1.2.4.3. DI Injection Regimes .....	8
1.3. Current Research.....	9
1.3.1. Engine and Fuel Research.....	9
1.3.2. Spray Morphology .....	9
1.3.2.1. Jet Expansion .....	10
1.3.2.2. Multi Jet Injectors .....	12
1.3.3. Imaging Techniques.....	16
1.3.3.1. Schlieren .....	18
1.3.3.2. Mie Scattering.....	21
1.3.3.3. Laser Induced Fluorescence.....	24
1.4. Gaps In Current Research .....	27
1.5. Project Objectives .....	30
<b>CHAPTER 2 - Methods .....</b>	<b>31</b>
2.1. Experimental .....	31
2.1.1. Test Chamber HPSC .....	31
2.1.1.1. Setup .....	31
2.1.1.2. Injectors and Designs.....	33
2.1.1.3. Injection Systems.....	34
2.1.1.4. Electronic Signals .....	36
2.1.1.5. Controls and Measurements.....	37
2.1.1.6. Test Conditions .....	40
2.1.2. Injection Testing .....	42
2.1.2.1. Setup and Methods and Data Outputs.....	42
2.2. Optical Diagnostics .....	43
2.2.1. High-Speed Schlieren Imaging .....	43
2.2.2. Planar Mie Scattering Imaging .....	46
2.2.3. Planar Laser Induced Fluorescence .....	48
2.3. Numerical Spray Simulations .....	51
2.3.1. Nozzle-Flow Simulation Setup .....	52
2.3.2. Lagrangian Spray Simulation Setup .....	53
2.3.3. Numerical Spray Processing .....	54
<b>CHAPTER 3 - Results and Discussion .....</b>	<b>57</b>
3.1. Experimental Spray Visualization Techniques Results .....	57
3.1.1. Experimental High-Speed Schlieren Results .....	57
3.1.2. Experimental Planar Mie Scattering Results .....	62

3.1.3. Injection Rate Testing .....	69
3.1.3.1. Current Profile Selection.....	69
3.1.4. Multi-Injector Testing .....	70
3.1.4.1. Spray G .....	72
3.1.4.2. Delphi-5 hole .....	73
3.2. Numerical Spray Simulation Results .....	78
3.2.1. Lagrangian Spray Simulation Results.....	80
3.2.1.1. Spray G .....	80
3.2.1.2. Delphi 5 hole.....	90
CHAPTER 4 - Conclusions and Future work.....	96
4.1. Conclusions.....	96
4.2. Future Work .....	97
BIBLIOGRAPHY .....	98

## CHAPTER 1 - INTRODUCTION

### 1.1. Significance

Due to a growing awareness of environmental challenges associated with fossil fuels, recent adjustments in global greenhouse gas emissions standards, and the rapid depletion of fossil fuel reserves, significant efforts are underway to advance combustion technology and explore alternative transportation solutions. The establishment of the "Framework Convention on Climate Change" by the United Nations has heightened concerns about CO<sub>2</sub> emissions [1]. While the passenger vehicle industry is swiftly moving toward electrification, challenges such as the substantial upfront cost and inadequate charging infrastructure remain significant hurdles in the heavy-duty sector [2]. In response, automotive companies are giving priority to hybrid and diesel vehicles to meet emission regulations and enhance fuel efficiency simultaneously [1], [3].

Various combustion strategies and post-treatment systems have been extensively researched for spark-ignition engines in light of these developments. Among the potential clean fuels for spark-ignition engines, liquefied petroleum gas (LPG) has gained recognition as a promising alternative in numerous studies [1], [4], [5]. However, the combustion and exhaust emissions of alternative fuels, including LPG, differ from conventional diesel fuel due to distinct physical and chemical properties. Despite being a hydrocarbon, LPG has significantly different values of boiling point, viscosity, and density which can alter the way LPG performs in traditional engine architecture [6], [7].

A fundamental understanding of the impact of physical and chemical properties on combustion and the formation of exhaust substances is essential for effective combustion control with different alternative fuels and their blends with conventional fuel. To comprehend ignition, combustion, and product formation processes, it is imperative to initially classify spray development and mixture formation processes. The volatility and viscosity of the fuel play crucial roles in influencing spray breakup and vaporization processes [8].

## **1.2. Background**

Research in internal combustion (IC) engines is dedicated to enhancing fuel efficiency and mitigating tailpipe emissions, including CO<sub>2</sub> and other regulated pollutants. Promising solutions include fuels like LPG, which stands out as a practical and cost-effective option for powering the heavy-duty transportation sector in the United States.

### ***1.2.1. Liquid Petroleum Gas as an Alternative Fuel***

Liquefied petroleum gas (LPG), primarily consisting of propane and butane, emerges as a byproduct of natural gas processing and liquid petroleum refining. Despite being the largest exporter, the United States maintains a substantial surplus of LPG. In terms of average commodity prices from 2019, LPG costs approximately 40% less than gasoline and diesel per gasoline gallon equivalent [9]. With a significantly higher H:C (hydrogen to carbon) ratio compared to diesel and gasoline, LPG has the potential to reduce greenhouse gas emissions if equivalent energy conversion efficiencies can be attained.

Moreover, LPG presents combustion advantages over many traditional fuels, boasting a higher-octane rating (RON ranging from 95-109.4 for a variety of global LPG blends vs. 84-93 for gasoline) and faster flame speeds. Stored as a liquid at moderate pressures, LPG exhibits significantly higher energy densities compared to compressed natural gas (CNG) (~27 MJ/L for LPG at 350 psi vs. 9 MJ/L for CNG at 3,600 psi) [10]–[12]. These characteristics imply that LPG would need fewer updates to the existing refueling infrastructure than CNG. There is also a notable interest in blending LPG with renewable dimethyl ether (DME) to further diminish the fuel's environmental impact.

Given these attributes, LPG emerges as a practical, economical, and more sustainable solution for fueling the heavy-duty transportation sector in the United States. However, for widespread adoption, energy conversion efficiencies for LPG engines must reach levels comparable to or higher than those observed in diesel engine platforms. The overarching goal of this research is to address fundamental limitations to achieve near-diesel efficiencies in heavy-duty on-road LPG engines, with a particular focus on the crucial role of LPG injection techniques in the development of LPG engines.

### 1.2.2. Injection Techniques

In response to the global imperative for more fuel-efficient vehicles, significant strides in design enhancements have been made to deliver cars with heightened efficiency. One noteworthy technological progression is the widespread implementation of Gasoline Direct Injection (GDI). Traditionally, the prevalent design for internal combustion engines was Port Fuel Injected (PFI), where fuel is sprayed into the intake ports to mix with incoming air as shown in Figure 1.1 (left). Many contemporary vehicles still adhere to this engine design, featuring fuel injectors mounted in the intake manifold, and the air/fuel mixture drawn into the cylinder head as the intake valve opens. In contrast, GDI engines position fuel injectors in the cylinder head as seen in Figure 1.1 (right), allowing direct spraying of fuel into the cylinder, where subsequent air/fuel mixing occurs [1], [4], [13], [14].

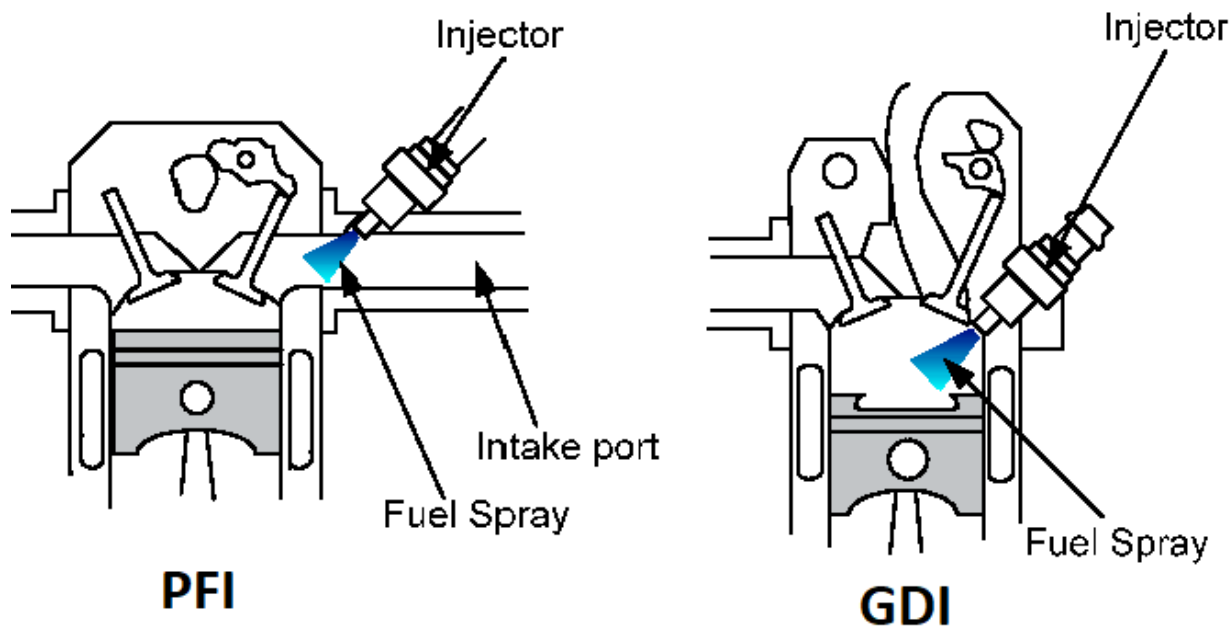


Figure 1.1: Schematic of Port Fuel Injection (left) and Gasoline Direct Injection (right) [14].

The GDI system offers several advantages over the PFI design, with superior fuel economy standing out as the most significant. Enhanced performance is another benefit, as the system combines higher injection pressures with precise fuel delivery into the piston cylinders. In GDI systems, finely atomized fuel promotes nearly instantaneous ignition, facilitated by sophisticated computer controls enabling multiple injections and fuel metering, contributing to both performance and efficiency. The GDI

engine's fuel systems demand a higher level of sophistication in hardware selection, including fuel injectors capable of withstanding elevated temperatures and pressures, as well as high-pressure fuel pumps. These injectors, often featuring multiple holes, play a crucial role in delivering precise amounts of fuel into the cylinder, with injector placement influencing overall system efficiency. Depending on the desired spray pattern, injectors can be side-mounted or positioned at the top-dead center of the cylinder.

Recent strides in high-pressure Gasoline Direct Injection (GDI) fueling systems have enhanced their viability. The combined use of direct injection (DI) and propane-fueling technologies presents a promising avenue for achieving significantly heightened efficiency and reduced emissions. Nonetheless, the effective implementation of DI necessitates a comprehensive understanding of the mechanisms governing fuel spray [4].

To further enhance performance, many GDI engines are paired with turbochargers, amplifying power delivery. Turbochargers utilize exhaust gases to drive a turbine, powering an air compressor that propels increased levels of oxygenated air into the cylinders, fostering a higher rate of fuel burn. The combination of turbochargers with direct injection technology is gaining traction in light-duty vehicles, with global automakers forecasting growth in this trend. The swift adoption of GDI technology by car manufacturers and the anticipated expansion in new vehicle production underscore the assurance that GDI vehicles will swiftly constitute a substantial percentage of the automotive industry worldwide [1], [4], [13]–[15].

### ***1.2.3. Direct Injection Methodologies***

In direct-injected gasoline engines, the fuel injection systems play a crucial role in achieving an optimal fuel vapor distribution—whether homogeneous or with a certain degree of stratification—while mitigating undesired effects like wall wetting. Therefore, characterizing the fuel injection systems and understanding how the fuel vaporizes and disperses in the combustion chamber is essential for investigating and enhancing the combustion process.

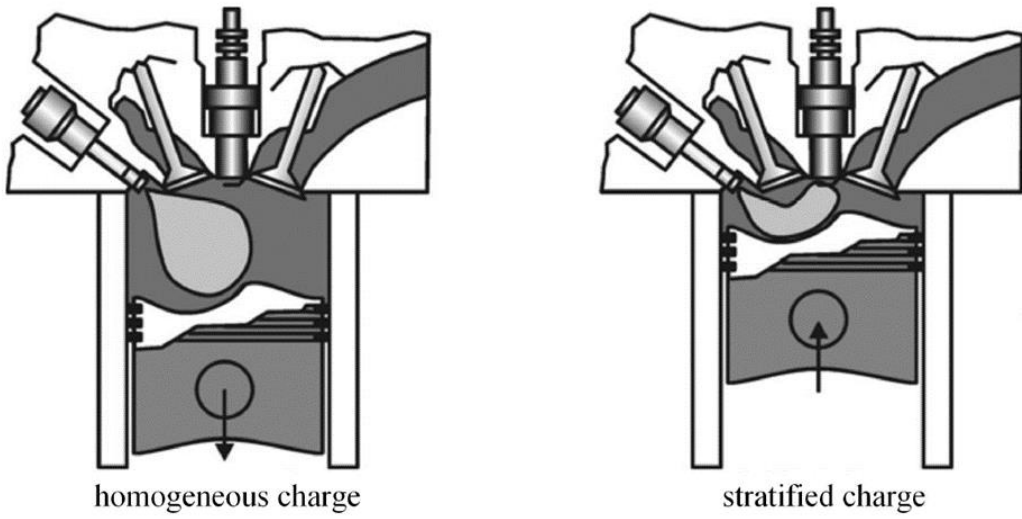


*Figure 1.2: Operating modes of a modern DISI engine: homogeneous (early injection - left); and stratified-charge mode (late injection - right) [16], [17].*

To attain robust performance across a diverse range of load-speed scenarios in DISI engines, as well as to simultaneously achieve various design objectives, different operational modes may be employed. These modes encompass homogeneous early injection and stratified charge preparation strategies [16]. The former is primarily utilized to meet stringent emission targets, while the latter enhances fuel economy by enabling the engine to operate in a globally lean manner, thereby avoiding throttling and pumping losses during part-load conditions. In the case of homogeneous charge preparation, fuel is introduced early in the induction stroke, as depicted in Figure 1.2. This early injection strategy can be implemented in both full-load (unthrottled, naturally aspirated or boosted) and part-load/idle (throttled, sub atmospheric intake) operations. Given the lower chamber pressures during the latter operational mode, a relatively modest injection pressure (e.g., 50 bar) is typically sufficient. Conversely, in the stratified-charge mode, fuel is injected during the compression stroke. Due to the higher chamber pressure at this injection timing, a significantly elevated injection pressure (e.g., over 100 bar) is necessary for effective charge preparation [17], [18].

#### **1.2.4. Injection Regimes**

Numerous research papers propose that direct injection (DI) alternative fuels, such as LPG, harbor the potential for additional engine performance benefits [15], [19]. However, these advantages cannot be

fully harnessed in a direct injection spark ignition (DISI) vehicle until the engine design is specifically optimized for LPG.

#### *1.2.4.1. Conventional injection regime*

In modern direct fuel injection systems, a highly pressurized liquid fuel undergoes rapid acceleration through the injector nozzle before being discharged into the combustion chamber. This procedure induces a notable decrease in the local pressure of the fluid along the injector nozzle. Due to the extremely brief time-scale associated with this process, it can be idealized as an adiabatic expansion phenomenon. In the context of conventional injection, the depressurized fuel exiting the injector remains in a liquid state prior to breakup. The isenthalpic process of  $1'-2'$ , as illustrated in Figure 1.3, characterizes the classical fuel injection process from the fuel rail to the nozzle exit. Subsequently, the injected liquid fuel undergoes primary and secondary atomization processes [17].

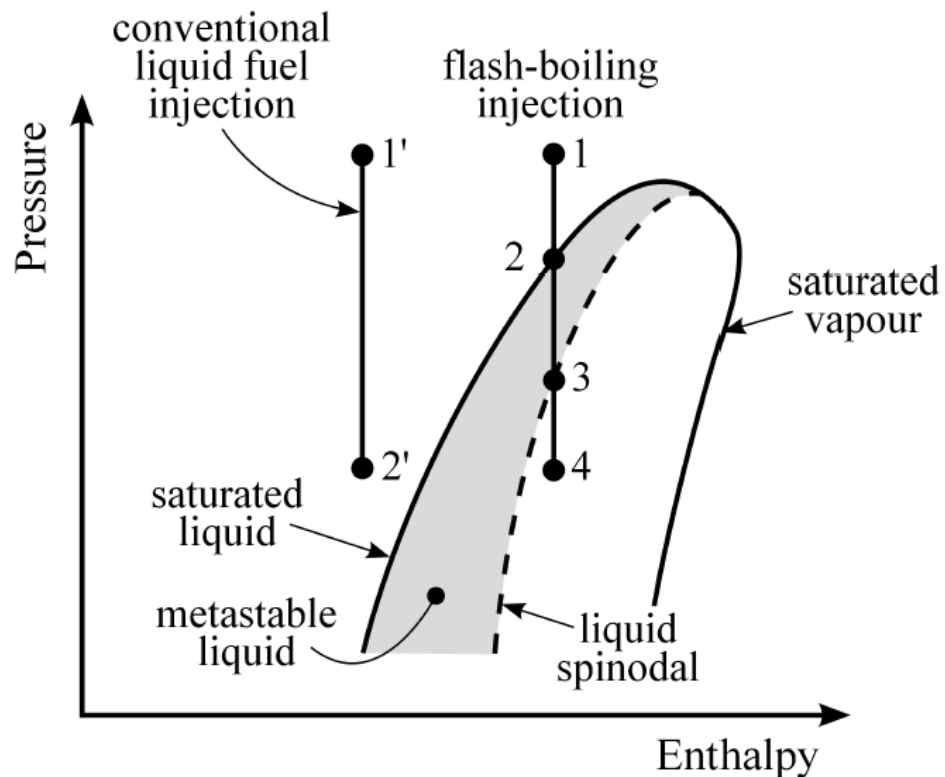


*Figure 1.3: Conventional and flash boiling fuel injection regimes indicated on an indicative pressure-enthalpy phase diagram [17], [20].*

In conventional injection scenarios, the depressurized fuel exiting the injector exists in a liquid state before undergoing breakup. The isenthalpic process, denoted as 1'-2' in Figure 1.3, outlines the traditional fuel injection journey from the fuel rail to the nozzle exit. Following this, the injected liquid fuel proceeds through primary and secondary atomization processes.

#### *1.2.4.2. Flash-boiling injection regime*

The phenomenon known as "flashing" in fuel injection systems is commonly characterized by an explosively rapid phase change process resulting from a sudden depressurization of fuel along the injector nozzle [21]. This occurs when a liquid fuel experiences swift depressurization well below its corresponding vapor pressure, leading to a state of superheated liquid. In this scenario, a portion of the liquid fuel undergoes a transition to a vapor phase, inducing a significant temperature drop in the remaining liquid fuel. This dynamic process is best elucidated by examining the enthalpy-pressure diagram illustrated in Figure 1.3.

The liquid fuel, initially sub-cooled or compressed and represented as point 1, undergoes an adiabatic expansion process as it passes through the nozzle orifice. As the accelerating liquid enters the metastable region, between points 2 and 3, vapor nuclei form and grow due to fuel vaporization at the bubble interface. In this region, the nucleation rate increases with pressure drop, reaching its pinnacle on the liquid spinodal curve (point 3). This curve delineates the thermodynamic limit to which the fluid can be stably superheated without undergoing evaporation [22]. Beyond this point, the liquid phase becomes unstable, initiating a rapid phase transition process. Ultimately, the formation of the flashing spray phenomena is concluded through spray atomization [20], [22], [23].

$$PR = \frac{p_{sat}(T_{liquid})}{p_{chamber}} \quad (1.1)$$

The intensity of the flash-boiling phenomenon is typically assessed using the flashing ratio (PR), defined as the ratio of the liquid's saturation pressure to the pressure into which the liquid is discharged, as shown in Equation (1.1).

Alternatively, another parameter commonly used to measure the extent of superheat is the degree of superheat (DS), as seen in references [24], [25]. This parameter, Equation (1.2), is defined as the temperature difference between the liquid's temperature and its corresponding saturation value at the pressure within the chamber.

$$DS = T_{liquid} - T_{sat}(p_{chamber}) \quad (1.2)$$

#### 1.2.4.3. DI Injection Regimes

Figure 1.4 illustrates these fuel injection conditions overlaid onto the saturation curves of iso-octane and propane, serving as surrogates for conventional gasoline and LPG. As depicted in Figure 1.4a, iso-octane falls within the conventional spray regime (where the chamber pressure exceeds the saturation pressure of the injectant) across a broad spectrum of injection conditions, encompassing full-load homogeneous and stratified modes. Due to propane's significantly higher vapor pressure compared to iso-octane (37.6 bar for propane vs. 0.78 bar for iso-octane at 90°C), it undergoes flash-boiling across a substantial portion of the DISI operating range. As evident in Figure 1.4b, the corresponding spray operates within the flash-boiling regime for the majority of engine-relevant conditions [17].

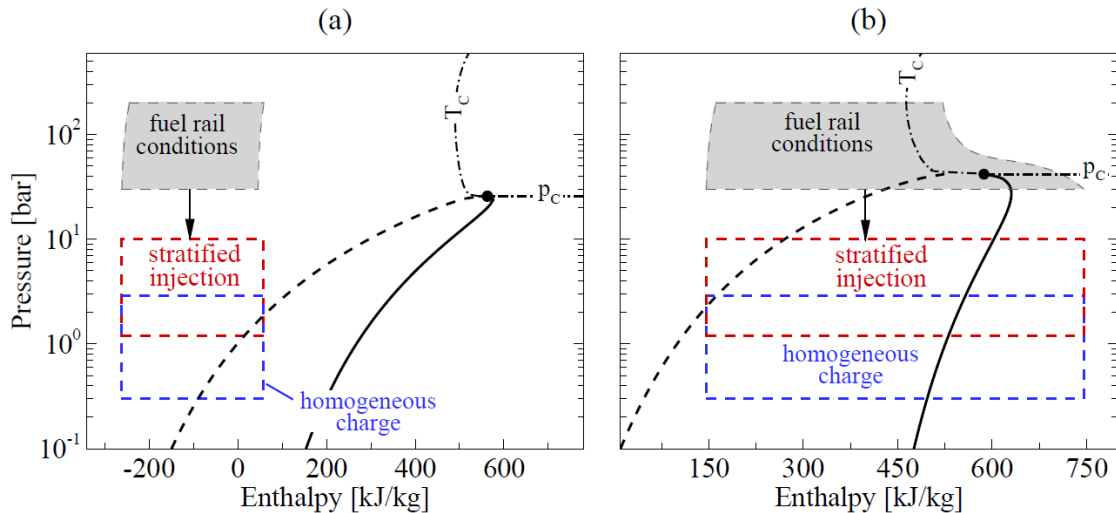


Figure 1.4: Plausible fuel injection conditions (250–390 K and 30–200 bar) and chamber pressures (0.3–10 bar) under different DISI operating modes for both naturally-aspirated and boosted engines superimposed onto the saturation curves of (a) iso-octane and (b) propane in a pressure–enthalpy diagram [17].

### **1.3. Current Research**

#### ***1.3.1. Engine and Fuel Research***

Throughout the review, it has been indicated that LPG possesses several advantageous combustion properties that, with appropriate engine modifications, can lead to high energy conversion efficiencies. The research octane number (RON) of LPG, ranging from 95 to 112 depending on the relative fractions of propane and butane, allows for the use of higher compression ratios and/or boost pressures than gasoline engines. This, in turn, enables greater break mean effective pressures (BMEPs). LPG exhibits flame speeds comparable to gasoline, surpassing those of CNG, facilitating dilute (high EGR combustion) and contributing to higher allowable BMEP before the onset of destructive knock.

Moreover, LPG can be directly injected into the combustion cylinder as a liquid, providing charge cooling similar to direct-injected spark ignition (DISI) gasoline engines. This allows for injection strategies that result in stratified charges, offering an additional means of controlling autoignition in the end gas (i.e., the unburned gas ahead of the flame). Due to its higher vapor pressure, LPG sprays have shorter penetration than gasoline, avoiding wall wetting and subsequent fuel-rich combustion responsible for high particulate matter emissions observed in DISI gasoline engines during cold operation [9].

For example, Kim et al. [1] employed four different injection schemes for forming stratified mixtures and two ignition schemes (single charge ignition and multi-charge ignition) to simultaneously reduce harmful emissions and fuel consumption. Experimental results indicated that fully stratified injection strategies showed an approximately 18% improvement in thermal efficiency, though combustion fluctuation was observed due to stratification. Furthermore, simultaneous reductions in NO<sub>x</sub> (nitric oxide) and CO (carbon monoxide) emissions were observed compared to homogeneous stoichiometric combustion.

#### ***1.3.2. Spray Morphology***

Traditional injectors often feature more than one nozzle, such as the 8-hole axisymmetric symmetric injector like the ECN Spray-G injector [26]–[29], commonly used in various studies and shown in Figure 1.5. If we focus on a single nozzle, it can be regarded as a converging-diverging nozzle, akin to those used

in rockets. The geometry, specifically the diameter, and other physical conditions of the environment, coupled with the properties of the fluid used, can exert a crucial impact on jet behavior. This, in turn, significantly influences the overall spray behavior, as well as the mixing and distribution of the charge within the engine cylinder.

The jet expansion phenomena generally play a negligible role for incompressible fuels like iso-octane and gasoline, along with many other traditional fuels. However, for a fuel like propane, characterized by high compressibility and flash boiling capacity, the design of the nozzle and the jet expansion phenomenon become dominant factors shaping the spray behavior [29].

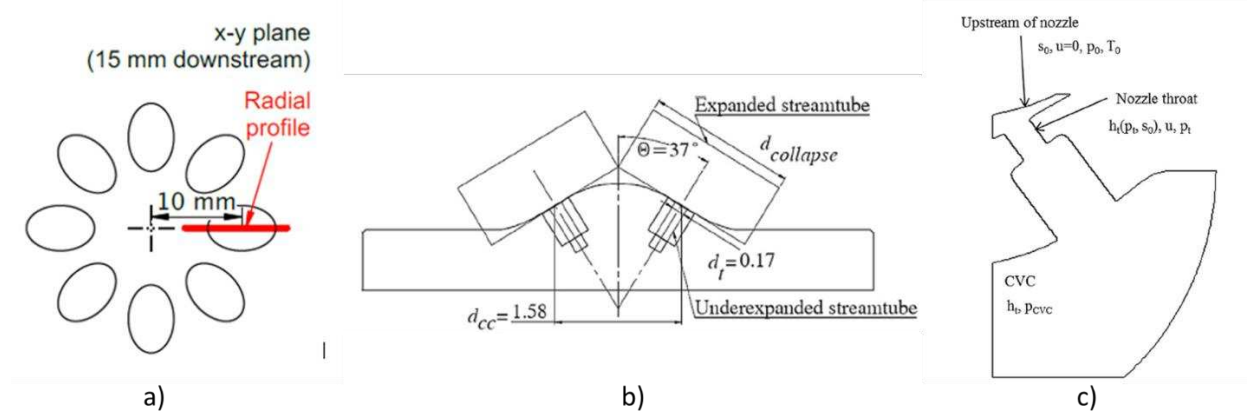


*Figure 1.5: A simplified view of the ECN Spray G injector showing a) top view of the cross-section showing 8 holes, b) a cross-section with two of the outermost holes in the symmetrical, 8-hole pattern, and c) the thermodynamic properties of the flow through one hole [28], [29].*

### 1.3.2.1. Jet Expansion

Expansion in an injector is the conversion of the elastic potential energy resulting from fuel pressurization into kinetic energy during the injection process. The behavior of this expansion process is primarily influenced by pressure—both the pressure of the exhaust and the pressure of the external environment into which it is released. The critical aspect is to design the nozzle shape to achieve the desired spray pattern.

In an ideal nozzle, the exit pressure ( $P_{exit}$ ) matches the ambient pressure of the external atmosphere ( $P_{amb}$ ), resulting in a perfectly expanded flow. However, achieving this ideal scenario is only possible at a specific atmospheric pressure for a fixed-geometry nozzle.

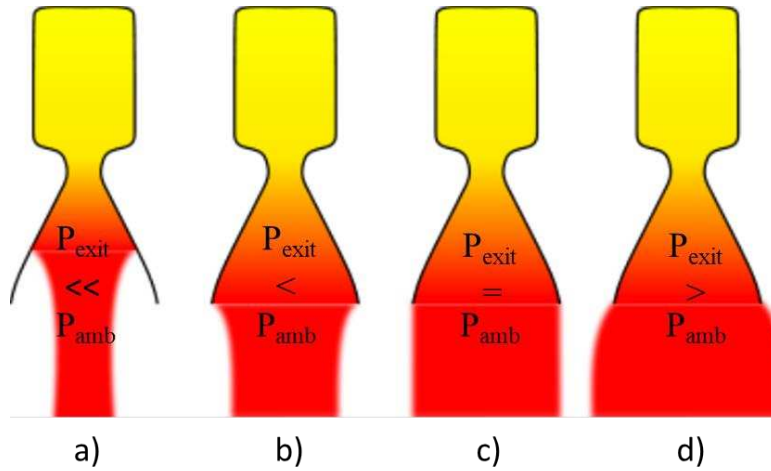


*Figure 1.6: Nozzles can be (left to right): a) grossly overexpanded, b) overexpanded, c) ambient, and d) under expanded [30].*

In the first scenario, Figure 1.6a and Figure 1.6b, where the external pressure surpasses the exit pressure, the condition is termed overexpanded. When an overexpanded flow traverses a nozzle, the higher atmospheric pressure causes it to compress inward and separate from the nozzle walls. This "pinching" of the flow leads to a reduction in jet diameter. Conversely, in the situation where atmospheric pressure is lower than the exit pressure, Figure 1.6 d), it is referred to as under expanded. In this case, the flow continues to expand outward beyond the nozzle exit [30], [31]. Both of these phenomena significantly impact the behavior of the jet as it propagates.

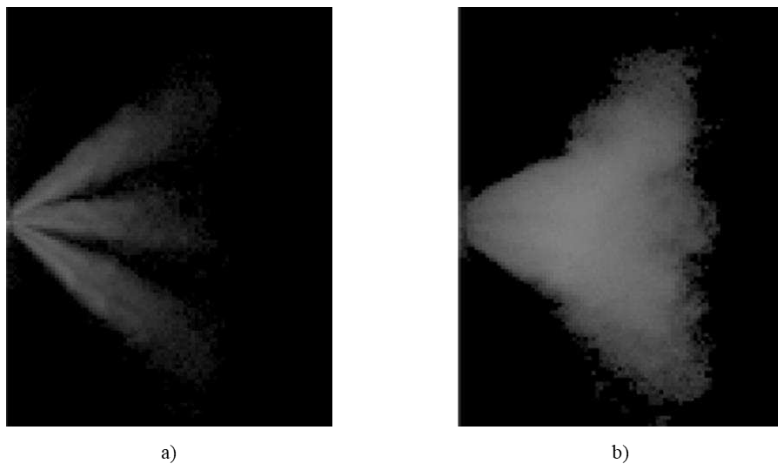


*Figure 1.7: Mie-scattered images of the liquid phase of propane at high flashing ratio at 500  $\mu$ s ASI with a)  $P_{cvc} = 1000$  kPa, and b)  $P_{cvc} = 300$  kPa [29].*

In the experimental analyses conducted by Lacey et al. [29], as depicted in Figure 1.7, noteworthy observations emerge regarding the behavior of the propane spray under varying chamber pressures. When the chamber pressure is elevated (Figure 1.7a), the propane spray demonstrates a distinct characteristic of non-underexpanded behavior. This is visually apparent as individual streams emanate from the nozzle and undergo a gradual expansion. Conversely, under conditions of low chamber pressure (Figure 1.7b), a singular plume with a notably enlarged diameter becomes evident, representing a clear instance of an underexpanded jet. These visual insights provide valuable empirical evidence for the influence of chamber pressure on the expansion dynamics of propane sprays. Given that most GDI injectors feature multiple nozzles, understanding how these multiple jets interact with each other becomes crucial to the study.

### 1.3.2.2. *Multi Jet Injectors*

Several studies [13], [29], [32]–[35] have utilized optical imaging of the liquid and vapor phases to analyze the overall behavior of these sprays. Mojtabi et al. [35] documented spray development of gasoline RON 95 for chamber pressures ranging from 0.969 to 0.3 bar at a fixed temperature of 60°C, as shown in Figure 1.8. As the pressure decreases, individual spray streams collapse inward toward the spray axis. At 0.4 bar, the individual spray streams become indistinguishable, forming a tulip shape with recirculation zones around the stream tips. This phenomenon is similar to spray shapes observed in previous studies [36], [37]. Further reduction in cell pressure to 0.3 bar results in an increase in spray width, accompanied by a cloud of fine spray surrounding the main spray body. A decrease in spray density suggests increased vaporization due to flash boiling.

Research on spray formation from pressure-swirl injectors has sought to explain the reasons behind spray collapse. Delay et al. [38] used fluorescent particle image velocimetry to show that interaction between the spray and surrounding air led to the formation of vortices on the inside and outside of the spray cone. The inner vortex pulled in air from the outside, dragging small droplets with it, causing the edge of the spray to curve and eventually collapse. Similar work by Allocca et al. [39] using the phase Doppler technique observed the same phenomenon. A recirculation zone is visible around the spray tip, and the aerodynamic

effects responsible for spray collapse involve interaction between the fuel spray and surrounding air, leading to the formation of recirculation zones and the eventual collapse of individual streams [35], [36].

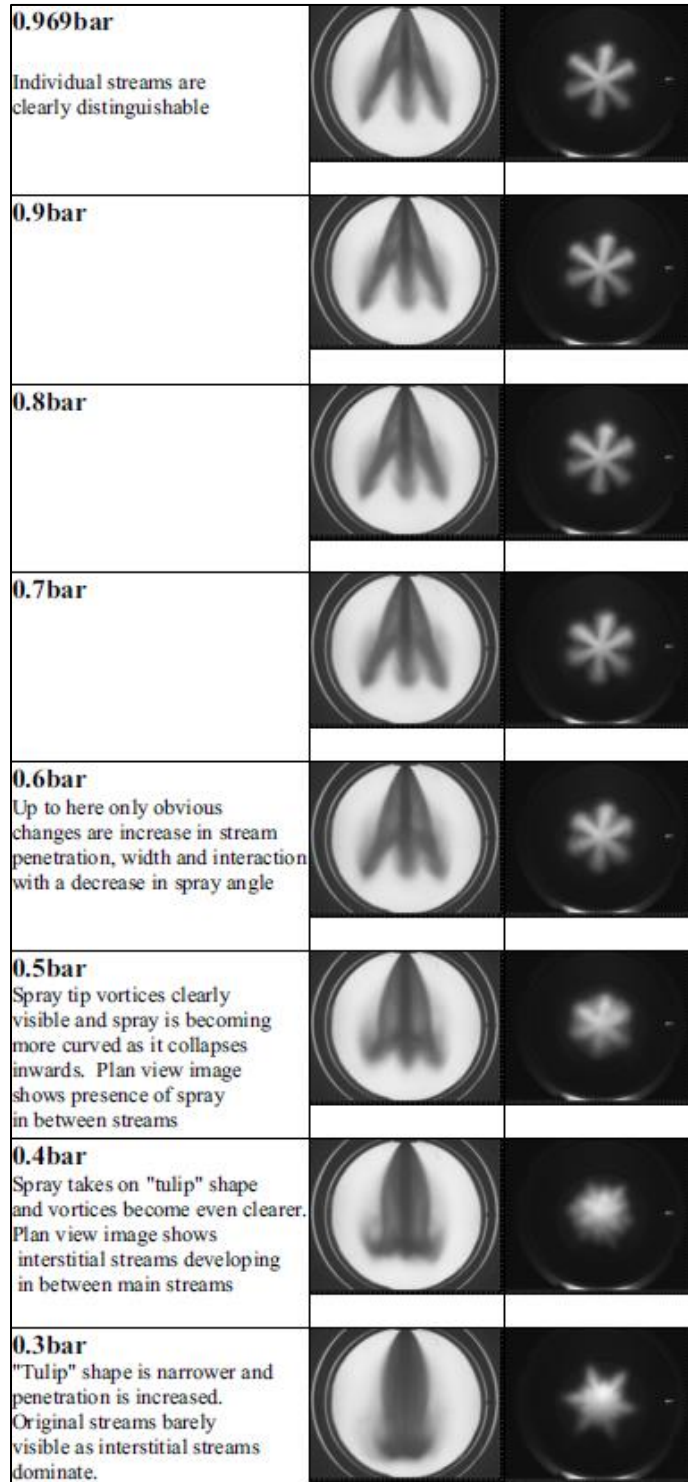
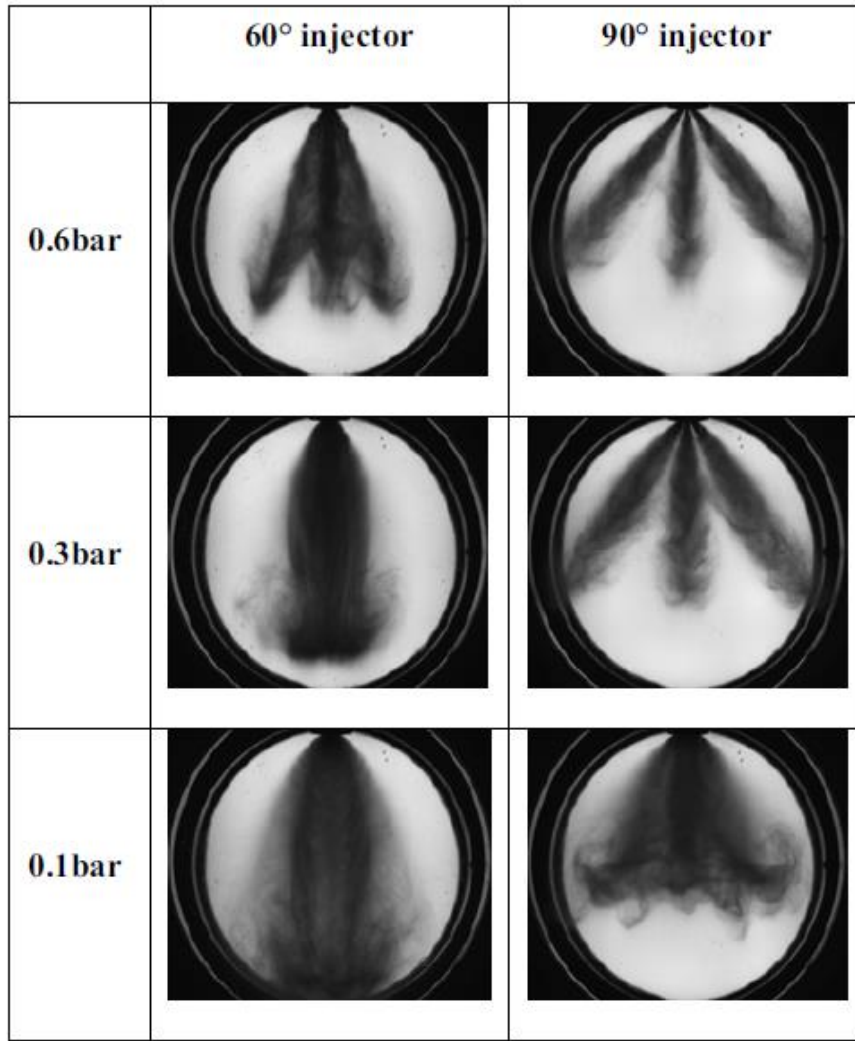


Figure 1.8: Spray pattern evolution with reduction of ambient/chamber pressure for gasoline RON 95 at 120 bar and 60°C at 2 ms after start of spray (ASOS) [35].

Mojtabi et al. [35] proposed that the presence of spray between the main streams results from the interaction between individual streams as the spray collapses inward. This interaction, characterized by the distance at which the individual streams join, increases with rising superheat, as observed in the side images in Figure 1.8. Another contributing factor to the interaction between streams is the formation of vortices due to aerodynamic interaction between the fuel spray and surrounding air. While toroidal vortices form on the inside and outside of the cone in a pressure-swirl injector, in a multi-hole injector, vortices form around each spray stream, leading to interaction between neighboring streams as vortices transport droplets from one stream to another. This transfer intensifies with increasing flash boiling. Therefore, the heightened visible stream interaction with increased superheat likely results from a combination of individual streams bending inward and interacting with each other due to vortex interaction. Varying the ambient pressure in the chamber alters the fuel's boiling point, changing the degree of superheat and affecting spray penetration, cone angle, and shape [35].

To explore whether a change in nozzle geometry and spray pattern could lead to variations in spray characteristics, Mojtabi et al. [35] tested two injectors—one with a nominal cone angle of  $60^\circ$  and the other with a nominal cone angle of  $90^\circ$ . They observed (as shown in Figure 1.9) that the  $90^\circ$  injector, with its increased cone angle, has reduced axial penetration compared to the  $60^\circ$  injector. At 0.3 bar, the spray from the  $60^\circ$  injector is fully collapsed, while for the  $90^\circ$  injector, spray streams are just beginning to turn inward. The authors concluded that the spray from the  $60^\circ$  injector collapses earlier than the  $90^\circ$  injector as the chamber pressure decreases. This is attributed to the closer proximity of spray streams for the  $60^\circ$  injector, causing earlier interaction and collapse with a lower degree of superheat. Figure 1.9 also reveals that as the chamber pressure is further reduced, the variation in penetration for the  $90^\circ$  injector spray is smaller than for the  $60^\circ$  injector, resulting in a wider tulip shape for the  $90^\circ$  injector. Similar observations were made with increased fuel temperature, suggesting that injectors with larger spray stream angles exhibit more robust fuel spray penetration to increases in superheat [35].



*Figure 1.9: Spray pattern evolution. Injector comparison, 120 bar, Fuel: Gasoline RON 95 at 60°C. 2 ms ASOS [35].*

Similarly, Lacey et al. [29] observed that propane consistently exhibited a flashing ratio above unity for the tested conditions corresponding to GDI engine operation, indicating continuous flash-boiling. However, significant plume interaction and spray collapse occurred only under specific conditions. The paper also emphasizes the crucial role of factors such as the distance between nozzle holes, nozzle diameter, and over-expanded jet diameter in influencing the spray structure and propagation. When expansion is substantial, adjacent spray plumes can interfere with each other, and in extreme cases, this plume-to-plume interaction results in severe spray collapse.

The consistent observation in the literature indicates that as the degree of superheat increases, whether through elevated fuel temperature or decreased ambient pressure, individual spray streams collapse inward toward the injector axis, leading to a reduction in the diameter of the spray footprint. Once fully collapsed, the individual streams become invisible between the main stream locations. Subsequently, these streams expand away from the injector axis radially, causing an increase in the diameter of the spray footprint. These trends were also evident across the range of temperatures studied at a fixed pressure. This suggests that the mechanisms driving the changes in the spray are influenced by a combination of temperature and pressure, particularly in relation to the boiling point of the fuel [29].

### **1.3.3. Imaging Techniques**

One highly valuable form of information is the spatial distribution of the fuel, both in the form of droplets initially and as vapor later in the preignition phase of the engine cycle. Numerous studies, such as those conducted by Lacey et al. [4], [13], [29], [40] and Mizia et al. [41]–[43], employ a Constant Volume Spray Chamber, as illustrated in the figure, to optically investigate the behavior of fuel sprays under conditions similar to those in an internal combustion engine. Various imaging techniques have been employed throughout the literature to analyze and record spray behavior, including Raman scattering [44], photography [45], laser light scattering [46], and two-wavelength laser absorption/scattering [47].

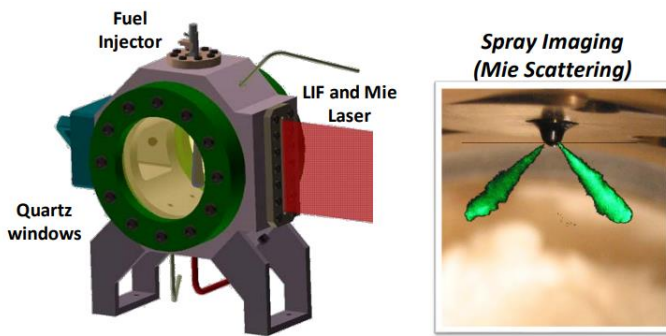


*Figure 1.10: HPSC design and Mie scattering images of diesel pilot fuel injection [41].*

Li et al. [48] conducted a characterization of multiple fuel sprays, including propane, using diffuse background illumination (DBI). Their findings revealed that under specific conditions, propane displays

liquid spray collapse induced by flash boiling when the ambient pressure is below 3.0 bar, as depicted in Figure 1.11.

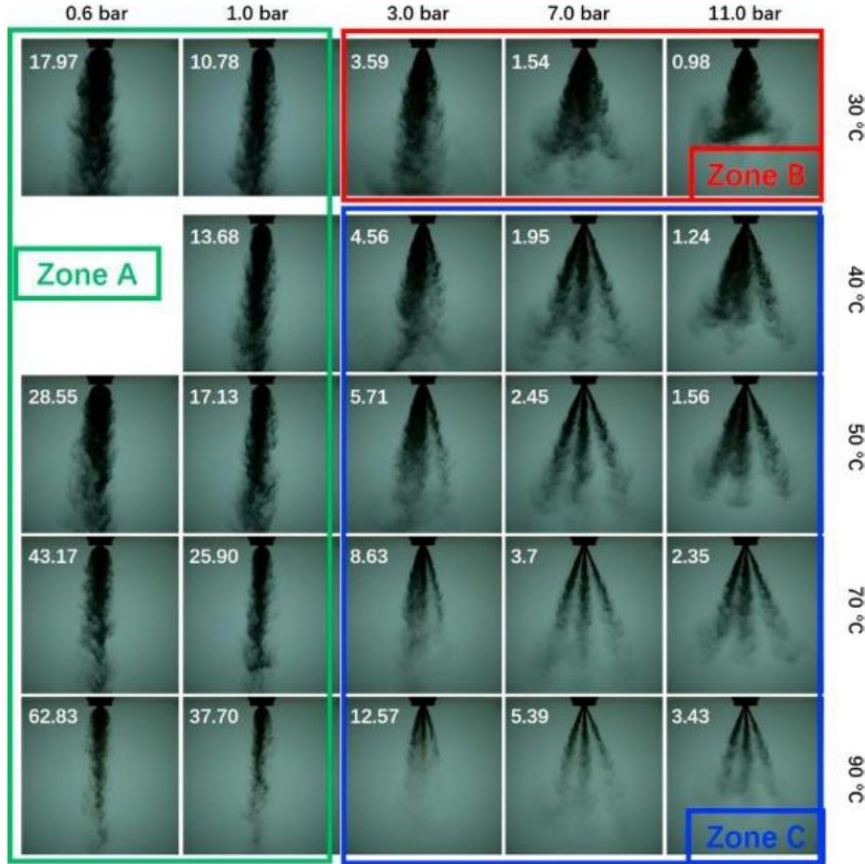


*Figure 1.11: Temporal evolution of propane spray under different conditions [48].*

In Melton's [49] research, diesel fuel droplets and vapor were simultaneously visualized through their fluorescence at widely separated wavelengths. By introducing small amounts (<1%) of the appropriate organic additive into diesel fuels or synthetic mixtures with similar properties, they induced a purple fluorescence ( $\lambda_{\text{max}} = 380$  nm) from the vapor and a blue-green fluorescence ( $\lambda_{\text{max}} = 470$  nm) from the droplets. Through suitable laser excitation, filter selection, and diode-array detection, real-time, in situ measurements were collected, separately capturing the injected fuel and its vapor. They employed two cameras with filters transmitting wavelengths corresponding to monomer and exciplex emission to image the fluorescence from the spray. The collected images provided insights into the vapor and liquid phase fuel distribution. The imaging system effectively captured the spray development of the vapor and liquid

phase over time after the start of injection. Additionally, the study analyzed the influences of injection pressure and ambient conditions on the location and relative abundance of liquid and vapor phase fuel.

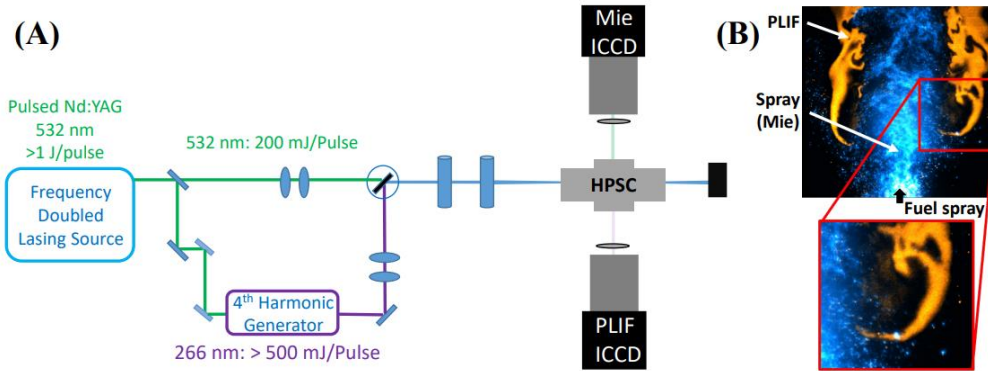


*Figure 1.12: (A) Optical configuration for simultaneous PLIF/Mie scattering measurements, and (B) resulting images [50].*

Figure 1.12 depicts the optical setup for simultaneous Mie scattering and planar laser-induced fluorescence (PLIF) measurement techniques, utilized by Alsulami et al. [50] to identify liquid/vapor phase regions in the evaporating spray. In the representative images (Figure 1.12 (B)), captured for jet fuel flames, the blue regions indicate the liquid fuel atomizing to form droplets, while the orange regions result from OH fluorescence, marking the location of the flame. By co-locating the data of fuel droplets and the flame, the team quantified the number of droplets penetrating the flame and emphasized the significance of these interactions on lean blowoff limits. Schlieren, Mie scattering, and laser-induced fluorescence imaging techniques are among the most commonly employed imaging techniques throughout the literature to gather spatial distribution of sprays. The fundamentals and applications of these techniques in the literature are detailed in the following sections.

#### 1.3.3.1. Schlieren

Schlieren photography is a technique used for capturing fluid flow, invented by the German physicist August Toepler in 1864 for studying supersonic motion. Widely employed in aeronautical engineering, it is used to photograph the flow of air around objects. The classical setup of an optical schlieren system involves a single collimated light source directed on, or from behind, a target object. Density gradients in the fluid cause variations in refractive index, distorting the collimated light beam. This

distortion leads to spatial variations in light intensity, which can be directly visualized using a shadowgraph system [51]–[53].

In a classical schlieren imaging system, a transparent object is illuminated with collimated or nearly-collimated light. Rays that are not deflected by the object proceed to their focal point, where they are blocked by a knife edge. Rays that are deflected by the object have a chance of passing the knife edge without being blocked, as illustrated in Figure 1.13 [54].

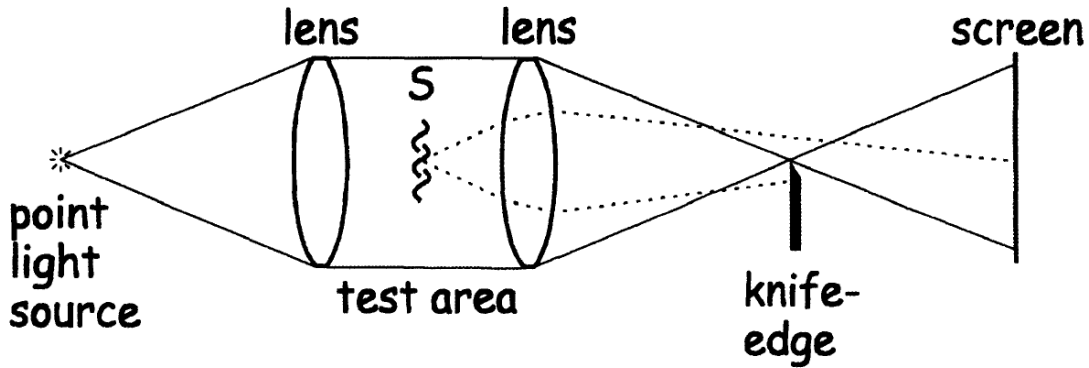


Figure 1.13: Diagram of a simple schlieren system with a point light source [54].

Consequently, a camera can be positioned after the knife edge so that the image of the object displays intensity variations caused by the deflection of rays. The outcome is a pattern of lighter and darker patches corresponding to positive and negative fluid density gradients in the direction normal to the knife edge. When a knife edge is employed, the system is commonly referred to as a schlieren system, measuring the first derivative of density in the direction of the knife edge. In cases where a knife edge is not used, the system is generally called a shadowgraph system, measuring the second derivative of density [54].

Examples of schlieren imaging to study flow patterns are depicted in Figure 1.14. The image on the left illustrates the thermal convection plume rising from an ordinary candle in still air, clearly capturing the transition from laminar to turbulent flow. This imaging technique has found applications in various fields. Figure 1.14 (right) demonstrates the use of schlieren to assess the effectiveness of wearing a mask to prevent the spread of COVID-19.



*Figure 1.14: The plume from an ordinary candle transitions from laminar to turbulent flow in this Schlieren photograph [55] (left), and NIST scientist Matthew Staymates used schlieren photography to qualitatively, and graphically, show the difference in how far a plume of breath can spread with and without a face covering (right) [56], [57].*

In the literature, this method is frequently employed for both qualitative visualization and quantitative measurement of fuel sprays, including vapor phase penetration [4], [29], [40], [58]. Illustrated in Figure 1.15, Lacey et al. [4] showcase both iso-octane and propane sprays under various engine operating conditions using schlieren imaging. In this case, schlieren effectively captures the overall global morphology of the spray, documenting the transition between non-flashing and flare-flashing sprays.

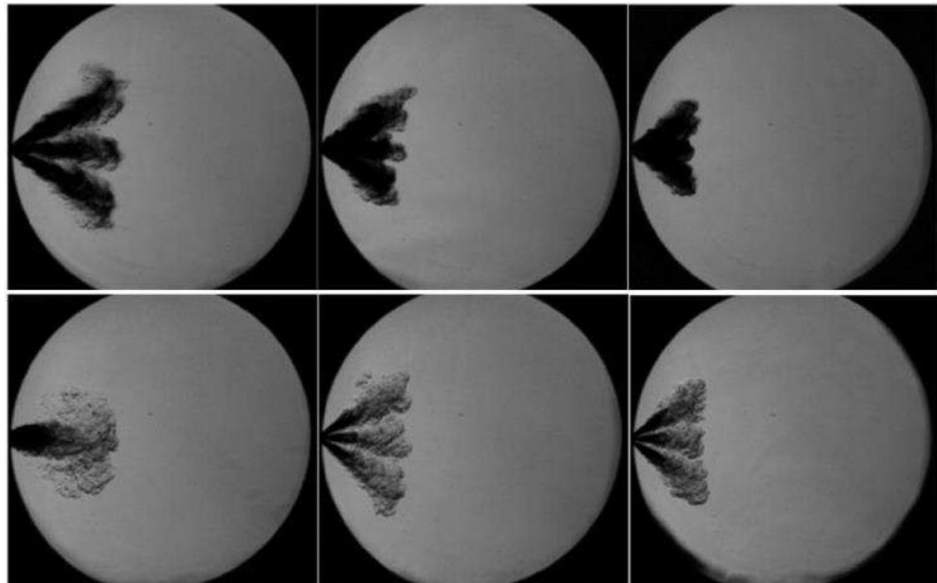


*Figure 1.15: Schlieren imaging for iso-octane (top) and propane (bottom) [4].*

### 1.3.3.2. Mie Scattering

The scattering of light can be conceptualized as the redirection of light when an electromagnetic (EM) wave, or incident light ray, encounters an obstacle or nonhomogeneity—in this context, a scattering particle. As the EM wave interacts with the discrete particle, the electron orbits within the particle's constituent molecules are periodically perturbed at the same frequency ( $v_o$ ) as the electric field of the incident wave. This perturbation leads to a periodic separation of charge within the molecule, known as an induced dipole moment. The oscillating induced dipole moment acts as a source of EM radiation, resulting in scattered light. The majority of light scattered by the particle is emitted at the identical frequency ( $v_o$ ) of the incident light, a process known as elastic scattering[59].

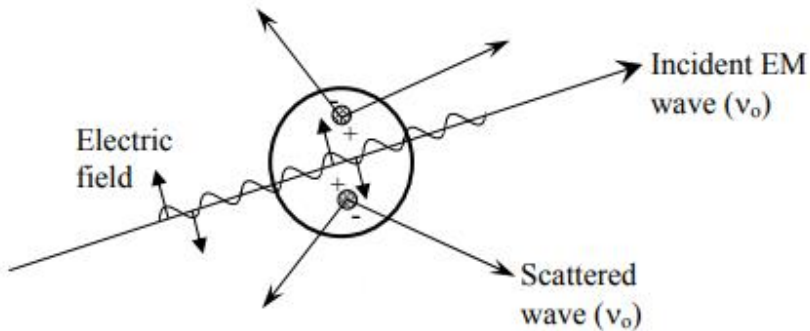
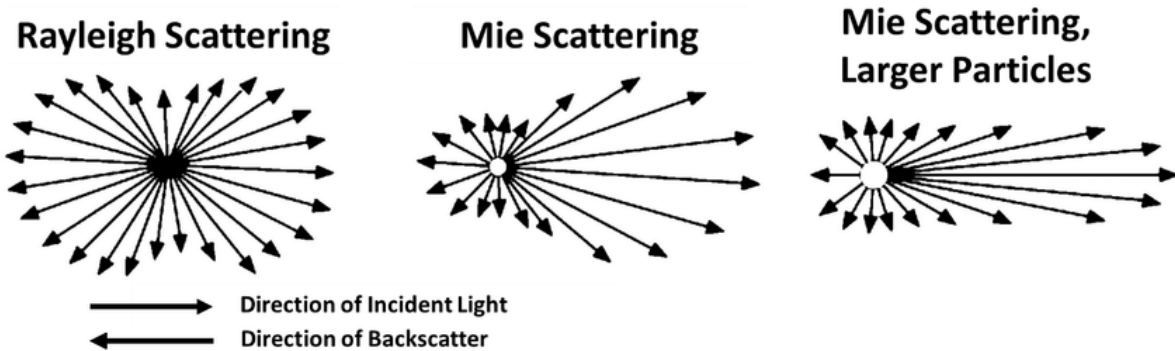


Figure 1.16: Light scattering by an induced dipole moment due to an incident EM wave [59].

In the realm of scattering techniques, Mie and Rayleigh scattering stand out as two elastic scattering methods. Mie scattering involves the elastic scattering of light by particles with a diameter similar to or larger than the wavelength of the incident light. The Mie signal is directly proportional to the square of the particle diameter, making it considerably stronger than Rayleigh scattering. It is crucial to note the pronounced angular dependency of the scattered intensity, especially for smaller particles, in successful Mie imaging experiments. On the other hand, Rayleigh scattering entails the elastic scattering of light by particles much smaller than the wavelength of the light. This makes it suitable for laser imaging in gases, as is the case with gas phase molecules. The efficiency of Rayleigh scattering varies inversely with the fourth power of the wavelength [60]–[63]. The fundamental principles of both scattering techniques are depicted in Figure 1.17.



*Figure 1.17: Mie scattering is caused by large particles while Rayleigh scattering is mainly caused by molecules [64].*

The blue color of the sky is a result of Rayleigh scattering, where gas particles in the atmosphere, being much smaller than the wavelength of visible light, scatter blue light more strongly due to its shorter wavelength. When sunlight traverses the atmosphere, its blue component is prominently Rayleigh scattered by atmospheric gases, creating a blue sky. During sunrises and sunsets, the impact of Rayleigh scattering intensifies, altering the transmitted light spectrum. In contrast, cloud particles, being comparable in size to the wavelengths of visible light, exhibit Mie scattering, resulting in white or grey appearances.

Mie scattering imaging has been widely employed in previous studies to assess liquid penetration through a medium. Illuminating a spray with a specific light wavelength causes the liquid region to scatter light in all directions, while vapor regions remain unilluminated.

Mie scattering phenomena are frequently examined through two distinct approaches: planar Mie scattering and global Mie scattering. Planar Mie scattering concentrates on the observation of scattered light within a specific plane, achieved by illuminating particles with a laser sheet as shown in the top row of Figure 1.18. This method is commonly applied in fluid mechanics techniques such as planar laser-induced fluorescence and particle image velocimetry, providing detailed insights into structures or particles within a defined cross-sectional area. In contrast, global Mie scattering involves illuminating particles from various angles, capturing scattered light in all directions as shown in the bottom row of Figure 1.18. This approach, more versatile and applicable across diverse scientific fields, offers a comprehensive understanding of particle scattering behavior in three-dimensional space. While planar Mie scattering is well-suited for

specific applications like flow visualization, global Mie scattering finds broader utility in areas such as aerosol science, astronomy, and particle characterization. The former excels in detailing information within a singular plane, while the latter provides a holistic perspective, collecting data from multiple directions for a more complete analysis of scattering properties.

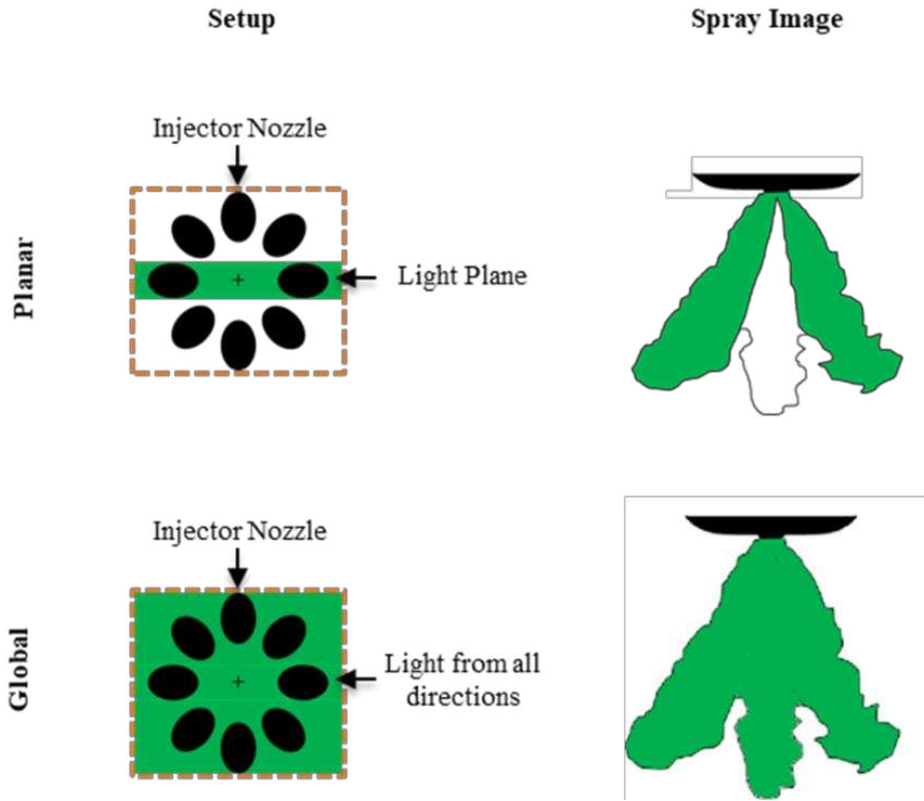


*Figure 1.18: Schematic showing various Mie setup (left column) and their consecutive spray schematic (right column) for Planar Mie (top row) and Global Mie (bottom row).*

Consequently, Mie scattering imaging proves valuable for capturing the liquid regions of a spray, as observed in various works [13], [29], [34], [65]. Lacey et al. [4] in Figure 1.19, captures global Mie images of iso-octane and propane under various conditions, providing insights into liquid spray behaviors. However, extracting plume-specific information critical for spray model validation remains challenging.

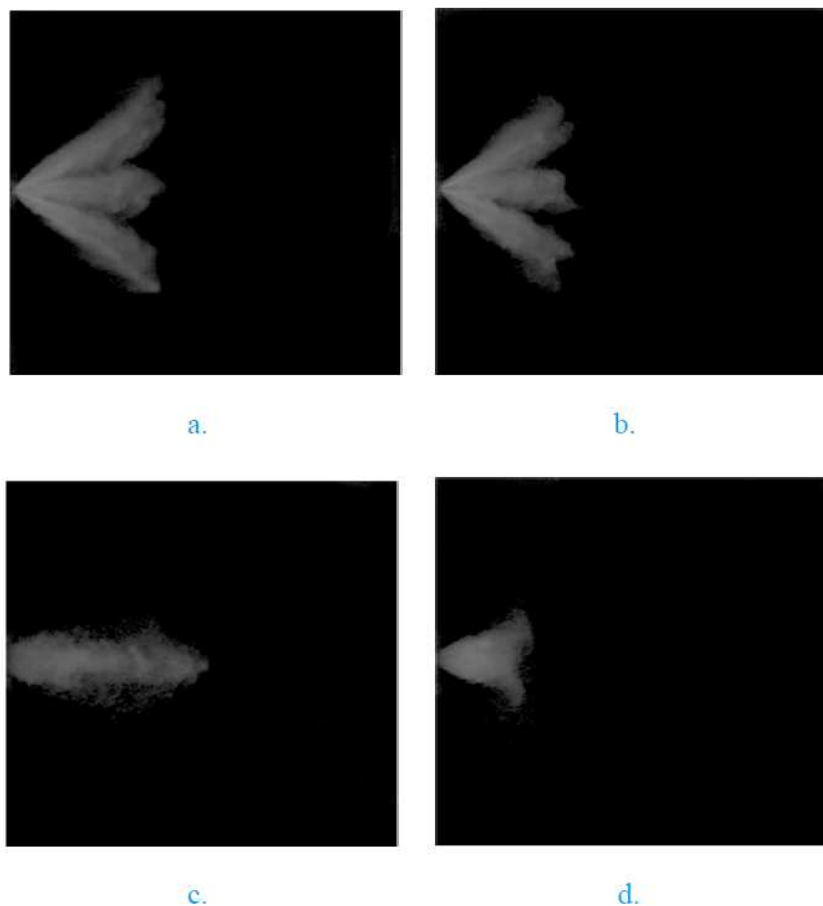


*Figure 1.19: Global Mie-scattering images of liquid cores at a CVC temperature of 298 K and at 500  $\mu$ s ASI at a CVC pressure of (a) iso-octane, 1 bar (b) iso-octane, 2.5 bar (c) propane, 1 bar (d) propane, 2.5 bar [4].*

#### 1.3.3.3. Laser Induced Fluorescence

Luminescence occurs when excited molecules emit light spontaneously to return to a lower energy state, typically the ground electronic state. If the excited and ground states share the same spin multiplicity (both singlet or both triplet states), it's called fluorescence. When the states have different spin multiplicities (triplet to singlet or singlet to triplet), it is termed phosphorescence. Fluorescence is generally faster than phosphorescence because the change in spin multiplicity is a less likely event, often referred to as a forbidden transition. Laser-induced fluorescence involves electronically exciting absorbing molecules with a laser beam of a specific wavelength. Creating a thin laser sheet from the laser beam results in planar laser-induced fluorescence, as depicted in the traditional PLIF setup shown in Figure 1.20 [66].

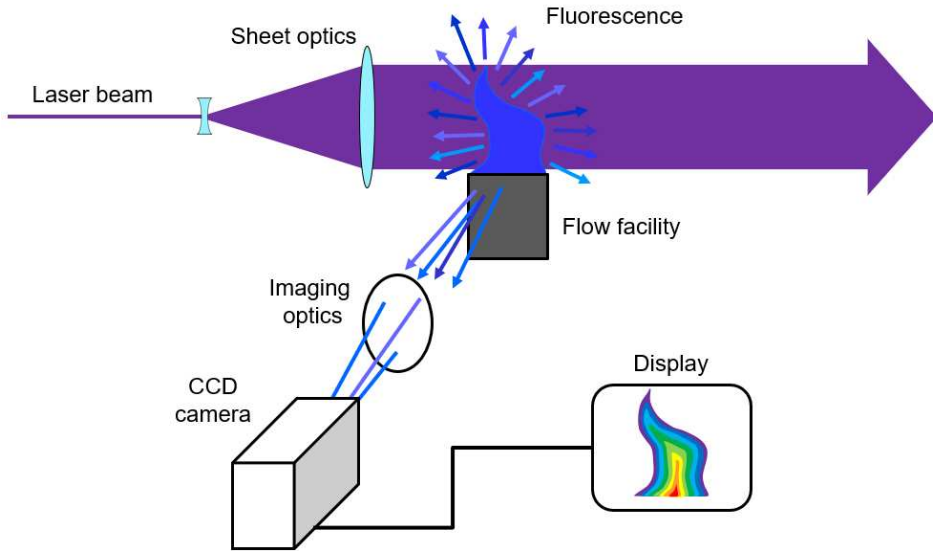


*Figure 1.20: Schematic of PLIF experimental setup [67]–[69].*

Acetone vapor luminescence has been a subject of extensive research [44], [70]–[72], with a predominant focus on fluorescence rather than phosphorescence [73]–[76]. This research, evolving with advancements in equipment, has explored a diverse range of testing conditions, spanning from near vacuum to atmospheric pressure, and employing near to mid-UV excitation [77]–[82].

Acetone stands out among fluorescing alternatives due to several advantages. Notably, its fluorescence in isobaric, isothermal flows exhibits a linear scaling with concentration and laser power under most conditions—a characteristic not shared by many fluorescing molecules [83]. At atmospheric conditions, the fluorescence yield of acetone is constrained by rapid intersystem crossing from the first excited singlet state ( $S_1$ ), responsible for fluorescence, to the first excited triplet state ( $T_1$ ), which phosphoresces (Figure 1.21). In the absence of  $O_2$ , the integrated phosphorescence emission for acetone vapor surpasses its fluorescence, with a phosphorescence yield of 1.8% compared to 0.2% for fluorescence. Phosphorescence also boasts a much longer lifetime in vapor (200  $\mu$ s versus 4 ns for fluorescence) [84].

While temporal separation of the two emissions is achievable, spectral separation proves challenging due to significant overlap of the spectra. Acetone's fluorescence, being short-lived, is minimally quenched by oxygen, unlike many other fluorescing molecules [66]. However, phosphorescence is strongly quenched by oxygen, leaving a robust fluorescence signal in the experimental conditions [84]. Additionally,

acetone's absorption of ultraviolet light (225 - 320 nm) and fluorescence in the blue (350 - 550 nm) allow for easy filtration of elastically scattered light using simple glass optics, as the absorption and emission spectra do not overlap. Lastly, acetone demonstrates lower toxicity compared to many alternative molecules, with breathing small amounts of acetone vapor posing no serious health risks, although prolonged exposure should be avoided [66].

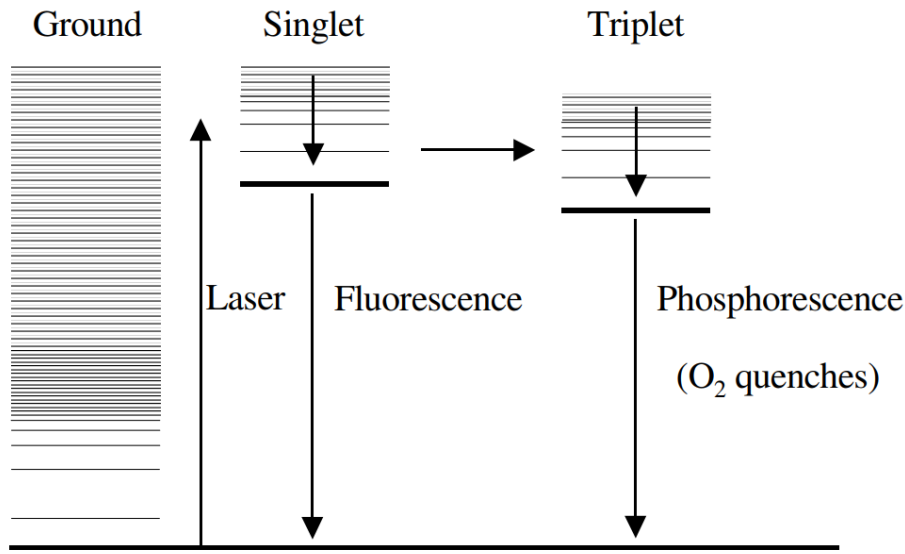


Figure 1.21: Diagram of acetone photo-physics [66].

Planar Laser-Induced Fluorescence (PLIF) stands out as a versatile technique for instantaneously mapping whole-field concentration or temperature in liquid flows. Its applications span various fields, including process engineering (mixing in stirring vessels, heating and cooling systems), biomedical engineering (drug transport in biological flows), and fluid dynamics research (turbulent mixing, heat transfer modeling, and indoor climate studies) [66].

In the realm of fluid dynamics and combustion physics, PLIF imaging proves to be a powerful tool, especially in high-pressure and high-temperature applications relevant to engines and gas turbines. Species like OH, CH, NO, NH, CN, CO, and O<sub>2</sub> radicals, as well as excitations within atomic and ionic species, are commonly investigated using PLIF measurements. This technique enables the characterization of transport properties, turbulence, temperature, pressure, and species concentrations within flames or plumes [66].

Olsen et al. [85] utilized PLIF to explore fuel jet penetration and fuel-air mixing within a static, pressurized optical engine under various engine-relevant conditions. Acetone-doped nitrogen was employed as a fuel to leverage acetone's fluorescent properties and prevent accidental combustion with natural gas. The PLIF images obtained (Figure 1.22) allowed for qualitative differentiation of various mixing conditions and computation of gas and fuel volume fractions.

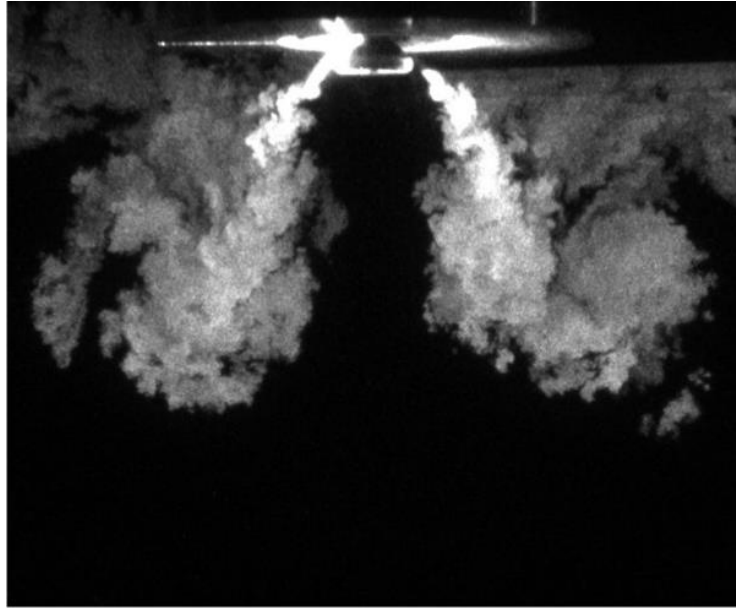


Figure 1.22: Fuel jet penetration and mixing for low pressure injection [85].

Similar to Olsen et al., numerous studies have employed PLIF to visualize flows by introducing a tracer, such as acetone, into the liquid or gas [66], [86]–[90]. However, identifying a tracer species with comparable fluid properties, including density, viscosity, saturation pressure, etc., for fuels like propane poses a challenge and warrants further investigation.

#### 1.4. Gaps In Current Research

The fuel injection systems in Gasoline Direct Injection (GDI) engines play a crucial role in achieving an optimal fuel vapor distribution, whether homogeneous or exhibiting some degree of stratification, while simultaneously preventing undesirable effects such as wall wetting. Consequently, there is a need to comprehensively characterize the fuel injection systems and analyze fuel vaporization and dispersion within the combustion chamber to enhance the combustion process. The processes of spray breakup and vaporization are influenced by the fuel's volatility and viscosity [4]. Liquefied Petroleum Gas

(LPG), owing to its distinctive physical properties—specifically, high vapor pressure, high volatility, and low viscosity—will likely necessitate adjustments to injection hardware, combustion chamber designs, and operational strategies (including injection timing, pulse duration, number of injections, etc.) to achieve efficiencies surpassing those of current state-of-the-art gasoline Direct Injection (DI) systems. Therefore, additional research is imperative to study LPG and understand its mixing processes before its integration into existing DI engines becomes viable. A more refined understanding of the mechanisms governing the fuel spray will facilitate the development of practical and high-fidelity simulations, thereby supporting the design of fuel injection systems tailored for high-efficiency LPG engines.

The incorporation of precise injection models has emerged as a pivotal tool for designing and optimizing Direct Injection (DI) fueled engines. The Lagrangian spray modeling approach proves effective in simulating engine-sized domains by treating the spray as a cloud of discrete parcels tracked in their trajectory and coupled with the gas phase [91], thus avoiding the intricate solution of liquid-gas interface dynamics. However, this approach heavily relies on semi-empirical modeling to define injection characteristics, jet evolution, and the fuel's phase change. By definition, it considers the spray as an incompressible fluid, leading to a conventional definition lacking accuracy in representing under-expanded jets, such as those observed in propane under engine-like conditions [29], [32]. To address this limitation, insights from detailed nozzle flow simulations, especially regarding the expansion of flare flashing gasoline sprays, inform the Lagrangian parcel injection model. Additional vaporization terms are introduced to enhance the model's accuracy [33]. This framework serves as the baseline for developing propane spray models, characterized by extreme volatility. Drawing from recent studies on gasoline sprays [92], the impact of flash boiling on jet breakup is further integrated by modifying characteristic droplet size reduction trends. The ultimate objective in the development of spray modeling for engine applications is to accurately predict liquid phase penetration to prevent wall wetting and appropriately represent fuel entrainment in the combustion chamber. These features are crucial for capturing the performance and emission tendencies of engine operations, typically grounded in preliminary correlation studies conducted in a constant volume inert environment.

Achieving higher efficiency in engines faces several limitations, including issues such as engine knock, misfires, adherence to low emissions limits, and the diverse chemical reactivity of Liquefied Petroleum Gas (LPG). In the United States, LPG used in vehicles is typically specified as HD-5 propane, constituting a 90% mixture of propane ( $C_3H_8$ ) with smaller or trace amounts of other gases. However, on the global market, the composition of LPG can vary significantly from the HD-5 propane specification, leading to a lack of sufficient experimental data for model validation [4], [13], [29], [40]. The principal component of LPG, propane, exhibits a propensity for flash-boiling at normal Gasoline Direct Injection (GDI) engine operation conditions compared to traditional fuels used in Direct Injection (DI) [13]. Therefore, it is crucial for spray models to capture the unique effects observed in LPG sprays. The notable differences in volatility result in a considerably higher occurrence of flash boiling in LPG sprays compared to gasoline. Consequently, the liquid/vapor penetration lengths of LPG are highly sensitive to the engine conditions at the time of fuel injection. Optimizing Direct Injection (DI) using LPG necessitates finding the ideal coupling between in-cylinder fluid motion, timed injection events, and robust spray models that are validated by experimental data capable of predicting LPG spray behaviors across a range of operating conditions [12]. As a result, this study focuses on liquid and vapor spray morphologies, as well as penetration trends, as major validation parameters to construct a reliable and accurate spray model.

To date, many studies have investigated the behavior of gasoline, diesel, a variety of surrogates, and alcohol fuels using Mie Scattering and schlieren imaging techniques to visualize spray development and species/phase distributions during cold injection and combustion events [40], [49], [93]–[97]; however, only a limited number of validated spray models [26], [98]–[100] and experimental data [4], [100], [101] are available regarding the spray dynamics of LPG at engine-relevant conditions [4], [100]. In Lacey's, Mie scattering and schlieren were applied to study [4] LPG and iso-octane sprays where global spray characteristics, including spray angle, spray liquid, and vapor penetration lengths, were presented for multiple spray/fuel and chamber conditions. While the data provides valuable information regarding the overall spray behaviors, it is challenging to extract plume-specific information, which is critical for spray model validation.

## **1.5. Project Objectives**

This work is part of a broader initiative aiming to facilitate the design of heavy-duty DI-LPG engines with energy conversion efficiencies comparable to or greater than state-of-the-art diesel engine platforms. The specific objectives include:

1. Development of an experimental setup for visualizing LPG sprays, with a particular focus on utilizing planar laser Mie scattering to map out the liquid regions within an individual plume.
2. Characterization of spray behavior under an array of engine-relevant conditions, employing various research and commercially available injectors. The goal is to support the development and tuning of DI-LPG CFD spray models for integration into full-cycle engine simulations.

## CHAPTER 2 - METHODS

In order to isolate the spray phenomena from in-cylinder flows, alternative test facilities such as a constant volume chamber are often employed. The simple operation and convenient optical access of this facility makes it attractive for controlled investigations that can be used to validate physics-based models and provide important insight into spray processes. This facility provides a fixed volume of trapped gas, which is inert and quasi-quiescent. It, therefore, allows for the study of spray phenomena isolated from the complex in-cylinder turbulence and combustion. The constant volume high-pressure spray chamber (HPSC), marked A in Figure 1a, is designed and optimized to primarily simulate conditions encountered in the combustion chamber of advanced direct injection, spark ignition engines.

### 2.1. Experimental

#### 2.1.1. Test Chamber HPSC

##### 2.1.1.1. Setup

Figure 2.1b shows the solid model of the HPSC. As shown, the HPSC is designed to allow 3 – way optical access inside the chamber using UV-grade fused silica windows (front and back windows with a diameter of 150 mm, and a 150 mm-tall square window on the side). This configuration allows for both line-of-sight and orthogonal visualization of the fuel spray.

The fuel injector was mounted vertically on the top of the chamber using a custom fuel rail and a fixture that incorporated a temperature-controlled water jacket, as seen in Figure 2.1a. The water jacket can heat the fuel to a desired temperature by utilizing a circulating pump, a 1 kW heater, a temperature controller, and a thermally insulated bath of glycol, as seen in Figure 2.1c, accurately within -0.5 to 4.7 K of error. The injector was pressurized using a ISCO 360D high-pressure syringe pump (labeled C in Figure 2.1a). The ambient pressure inside the HPSC was regulated using pressurized nitrogen gas and a vacuum pump, well within the margin of experimental error.

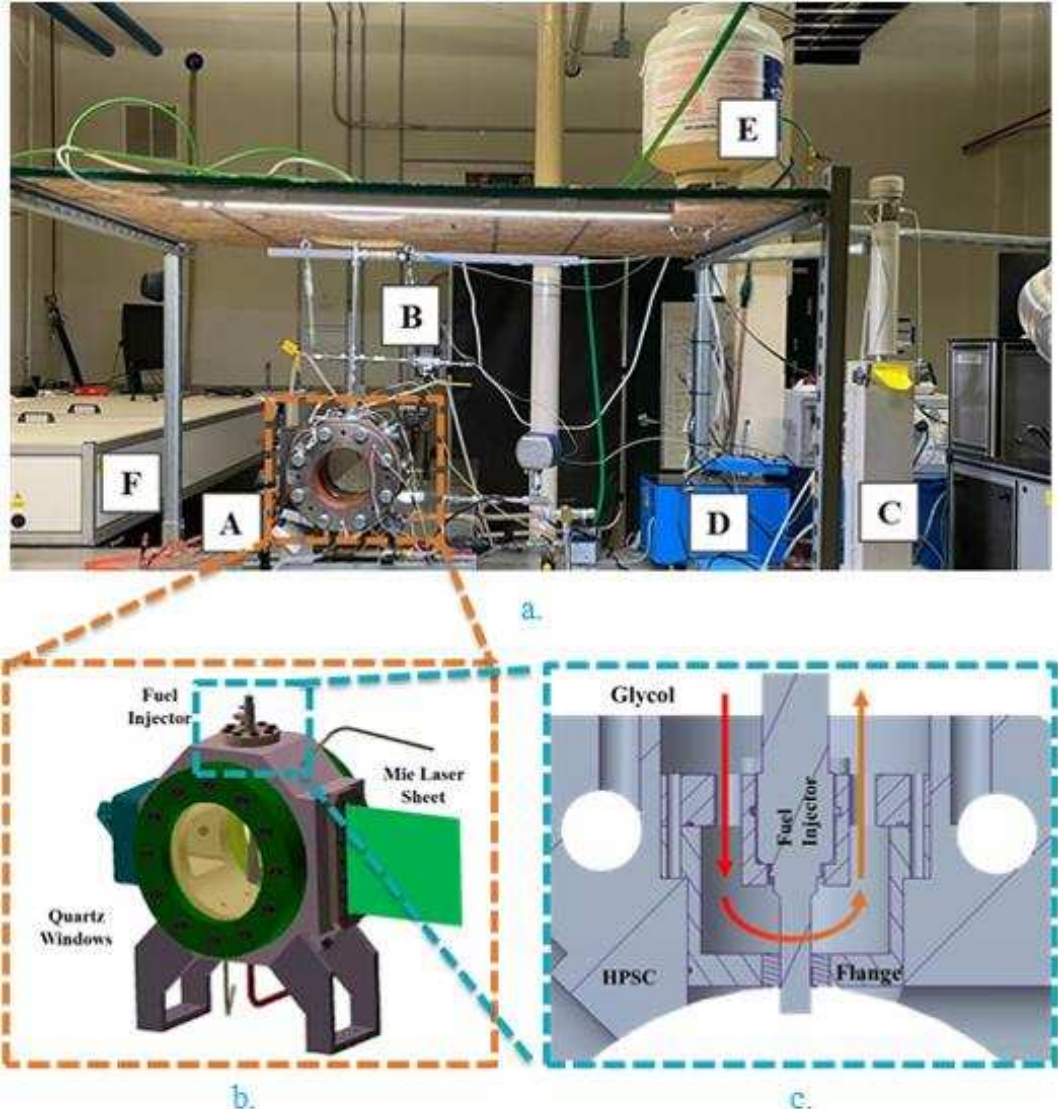


*Figure 2.1: (a) HPSC setup assembly including (A) high-pressure spray chamber, (B) Spray-G fuel injector and a custom fuel rail, (C) syringe pump, (D) large engine control module, (E) propane tank, and (F) Nd: YAG laser, (b) HPSC solid model [41], and (c) a schematic describing working of the fuel injector and the water jacket.*

The HPSC was fitted with an absolute pressure transducer and thermocouples mounted on the metal block of the chamber to monitor and acquire the instantaneous chamber conditions through a LabVIEW virtual instrument interface. The corresponding temperature was controlled via high-power-density cartridge heaters embedded in the body of the HPSC and tape heaters wrapped around the silica windows, within -5 to 10 K of error. Before each injection event, the HPSC was purged with pressurized nitrogen gas

to inhibit the oxidation of the fuel, making the ambient conditions non-reactive. A combination of o-rings and gaskets were used to seal the chamber under high ambient pressures.

### 2.1.1.2. Injectors and Designs

Four injectors including the Bosch BMW 325i EU5, Delphi 7-hole stock injector, ECN Spray-G injector, and modified 5-hole Delphi injectors have been tested at various engine-like conditions and high-speed schlieren and planar Mie imaging for propane and iso-octane fuels were carried out in the previous quarters. The data was processed and sent to Argonne National Lab for model tuning and validation.

Few other injectors: Bosch BMW 335 I injector, Bosch Jaguar Injector, and XDI +65 injector, were also tested along with the previously mentioned injectors and these injectors are shown in Figure 2.2.

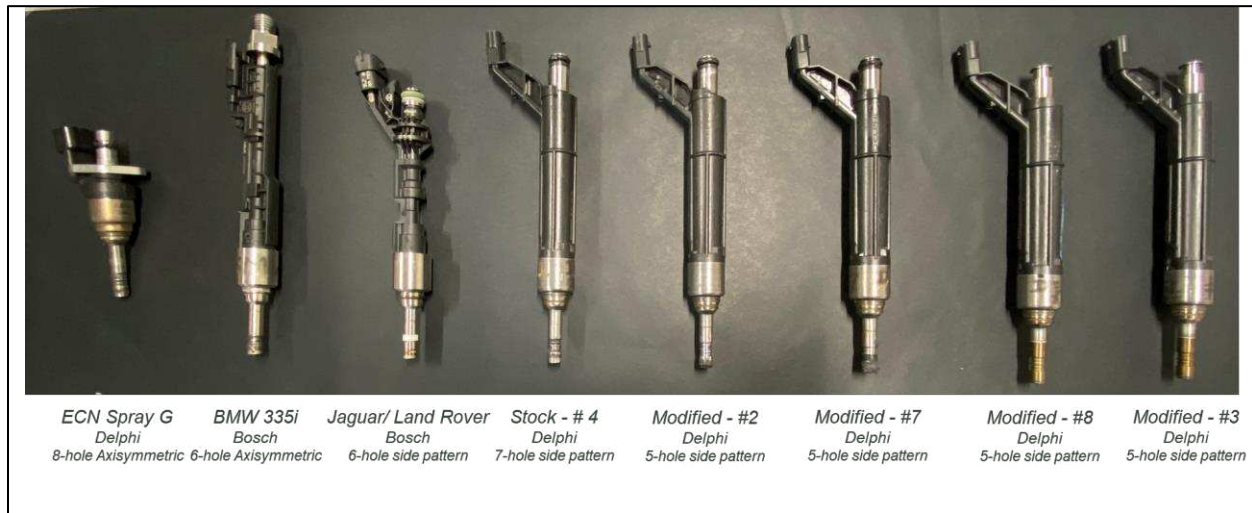


*Figure 2.2: Various injectors, and their manufacturer and hole pattern, tested in the spray chamber for injection testing.*

The Spray G fuel injector is an experimental, Delphi manufactured, axisymmetric, 8-hole, solenoid driven, GDI fuel injector. The Spray G AV67–012 DI fuel injector provided by the Engine Combustion Network (ECN) has been used extensively in prior literature and has been well characterized [28]–[31]. Since the goal of the research is to create a data base at engine like condition, a BMW 335 I EU6 Injector was purchased. This six-hole, axisymmetric injector is used in BMW 335 I, 3-liter engine, and is capable

to reach pressure up to 350 bar. Figure 2.2 shows the fuel injector purchased. Both the Bosch EU5 and EU6 injectors were chosen because of their ability to hold high pressure fuel up to 350 Bar.

### 2.1.1.3. Injection Systems

The injector was pressurized using a high-pressure syringe pump labeled C in Figure 2.1a. Once an injector was purchased, a flange design was to be modeled which will be used to install the injector to the spray chamber and can incorporate a cooling jacket design, similar to that of in Brear's work [3], to keep the injector tip at a known temperature.

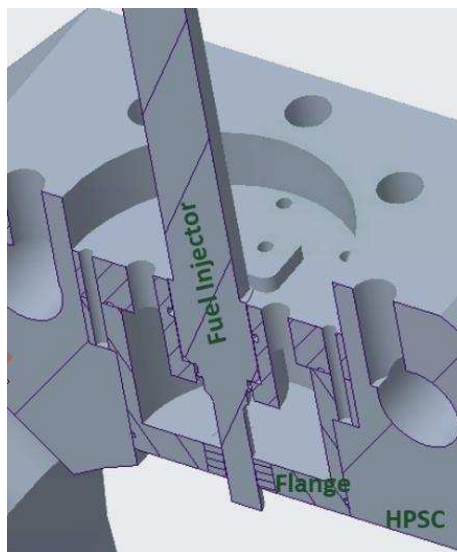


Figure 2.3: Flange Design for the Fuel Injector

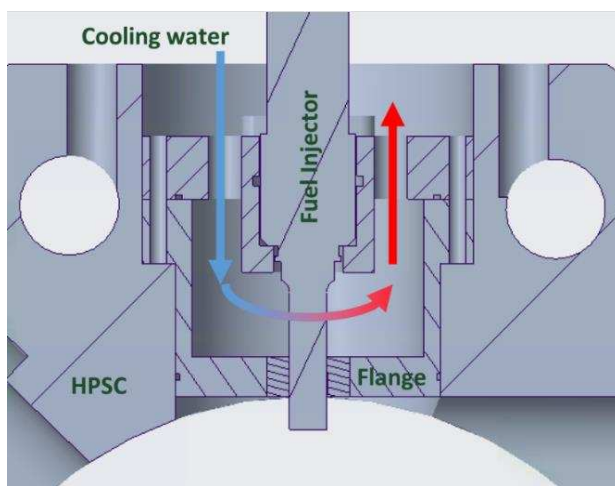
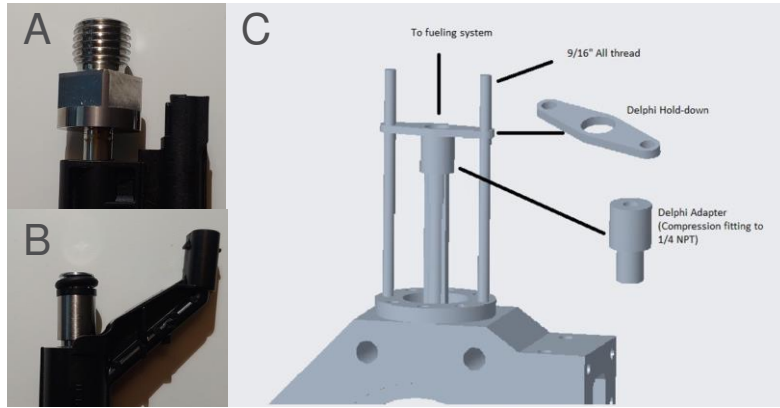


Figure 2.4: Cooling Jacket design around the Fuel Injector

Figure 2.3 shows the flange design which will be used to keep the fuel injector in place. The system will be sealed using O-rings. The design, as seen in Figure 2.4, also includes the cooling jacket. Water at a constant temperature will pumped and circulated around the metallic tip of the fuel injector to keep the fuel inside the injector at a constant temperature. The temperature around the injector tip was regulated by flowing glycol through the water jacket as shown in Figure 2.4.



*Figure 2.5: A). Bosch EU6 Injector fitting, B). Delphi injector fitting, C). Delphi Injector adapter configuration*

Since the study is now done using a Delphi 06M-906-036AE fuel injector, modification to the current HPSC fuel injector mounting system were to be made to incorporate the unique design of the Delphi injector. Shown in Figure 2.5, an adapter was designed to fit the Delphi injector inlet port. As seen in part B of Figure 2.5, the Delphi injector is a completely round shaft with an O-ring to seal the connecting adapter. An adapter was manufactured to fit the Delphi injector as well as adapt to the rest of the fueling system. This adapter is pressure tested to 5000 psi and has been able to hold pressure reliably and securely. To fit this adapter securely to the HPSC and the Delphi injector a securing bracket was designed and built. This bracket uses all thread rods and a water jet section of steel to fit on the Delphi injector. With this bracket set up, the injector as well as the cooling jacket assembly are secure and more structurally sound. A brief representation of the designed bracket can be seen in Figure 2.5, part C.

#### 2.1.1.4. Electronic Signals

The fuel injector was driven by Woodward's Large Engine Control Module (LECM), marked D in Figure 2.1a, to control the electronic injection duration. The LECM was programmed to produce an electronic injection duration of 680  $\mu$ s after the start of injection (ASI). But 870  $\mu$ s ASI was the actual injection duration that was measured using schlieren imaging synced to an oscilloscope. In the current configuration, there are two injectors being utilized for timing and control of the entire system. The Delphi injector is the main injector to be visualized with the techniques that have been mentioned before. Also being used is the Spray G injector, kindly provided by the Engine Combustion Network (ECN). ECN was kind enough to provide a current profile for the Spray G injector. Since both injectors are made by the same company, i.e., Delphi, the same current profile was used for both. As seen in Figure 2.6, current profiles for the Spray G injector are shown at different pressure/power traces, Low, Normal, and High. Most of the time the high-power waveform current profile has been used with its wide pressure range. An LECM interface has allowed for the use of the Spray G current profile to be implemented with both injectors. A current profile was recorded from an oscilloscope and measure and matches the intended current profile extremely well.

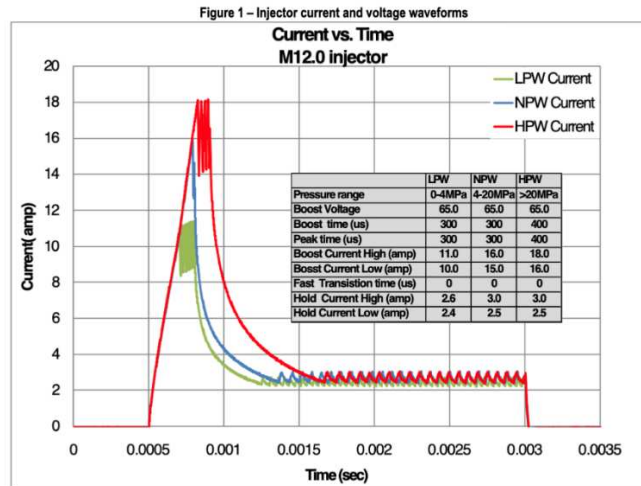
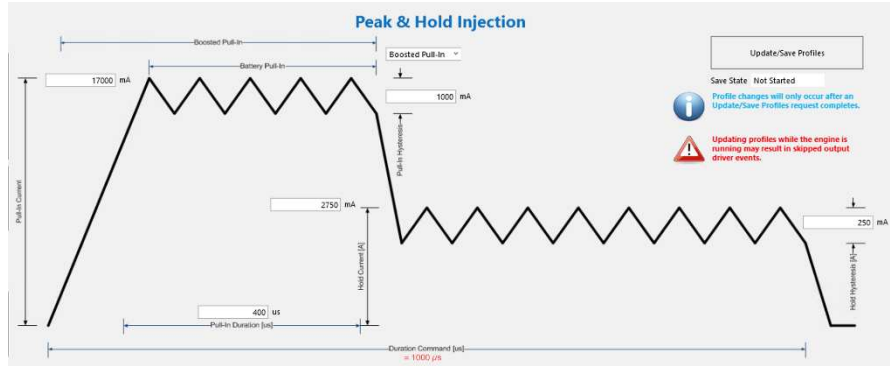


Image of driver box harness  
(here shown for 1-cylinder harness; multi cylinder harness looks similar):

Figure 2.6: Spray G Current Profile



*Figure 2.7: LECM Hold and Peak Profile Configuration*

The LECM is an adaptable engine control driver that is capable of controlling pulse width and a pseudo-RPM (to mimic an engine). The LECM is also configurable to create custom current profile as well as a large library of predefined current profiles. Figure 2.7 shows the Spray-G current profile programmed in to the LECM software. To pressurize the fuel system, a syringe pump (4) capable of reaching 300 Bar is used to pressurize the accumulator (3), which will hold an allotment of fuel before firing the injector.

#### *2.1.1.5. Controls and Measurements*

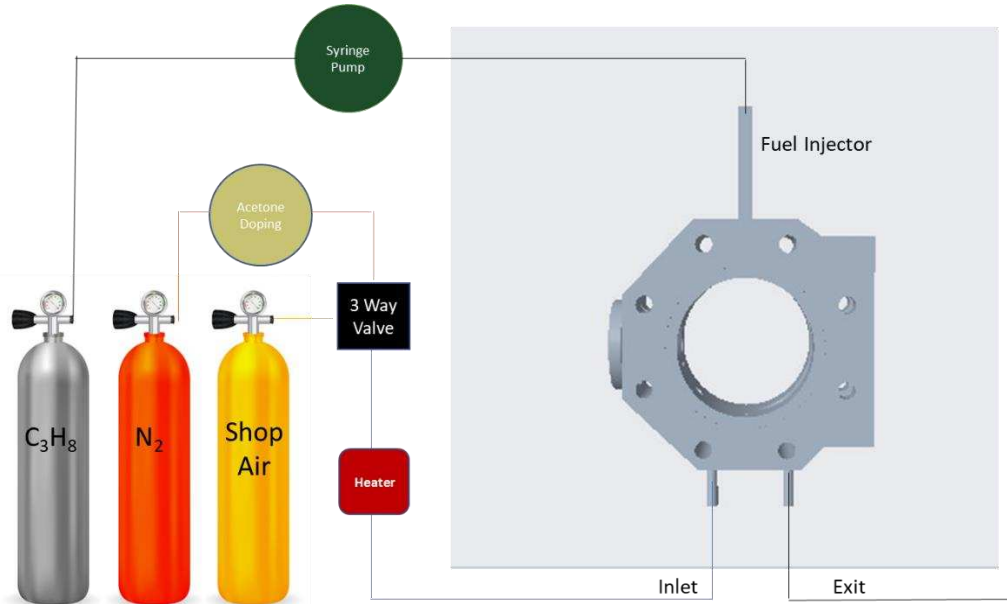


*Figure 2.8: Overview Schematic of the Fueling and Control System*

For the fueling system, the team produced the schematic shown in the Figure 2.8. To prepare the HPSC for injection, shop air and nitrogen gas will be flushed in the system to get rid of any reacting species

which might be present in the chamber. The advantages of nitrogen gas are that it will mimic the air to some extent inside the chamber, and it is also non reacting to other species involved in the experiment. The inside of the chamber will be heated by flushing shop air and nitrogen gas through a heater set at a desired temperature as shown in Figure 2.8 and Figure 2.9. Then, nitrogen will be used to pressurize the inside of the chamber to a desired pressure. Before letting the nitrogen gas in the HPSC, it will be doped with acetone which will be used to track the displacement in the nitrogen gas during injection process using acetone PLIF technique. The doping mechanism is yet to be identified. For temperature control of the HPSC block, four cartridge heaters will be used to attain the desired temperature.

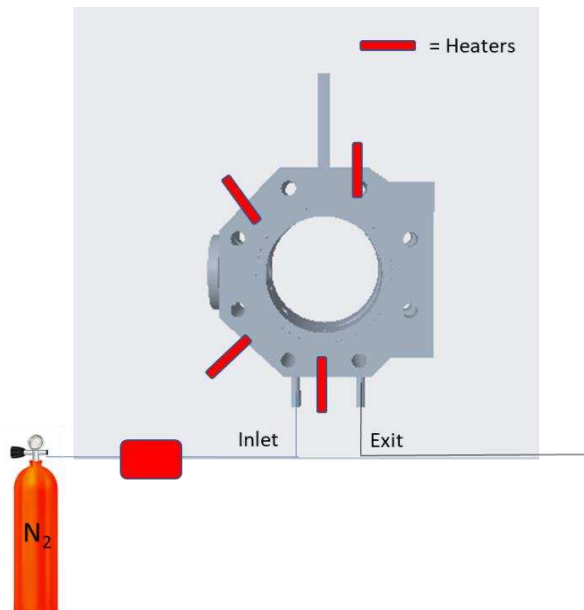


*Figure 2.9: Temperature and Pressure Control of the HPSC*

The Gas Processors Association HD-5 LPG specification states it must consist of at least 90% of propane. Therefore, for testing, propane is be used. The preliminary work for the fuel system involved the calculation of the mass per injection for a propane engine. The ALPINE project's device goal is to attain 44% efficiency in a Cummins X-15-liter, heavy duty, six-cylinder, four-stroke, and 500-horsepower engine. Through calculation it was identified that 136.2 milligrams of propane are needed per injection. This value is comparable to the mass per injection values of a heavy-duty propane engine found in the literature review [20].

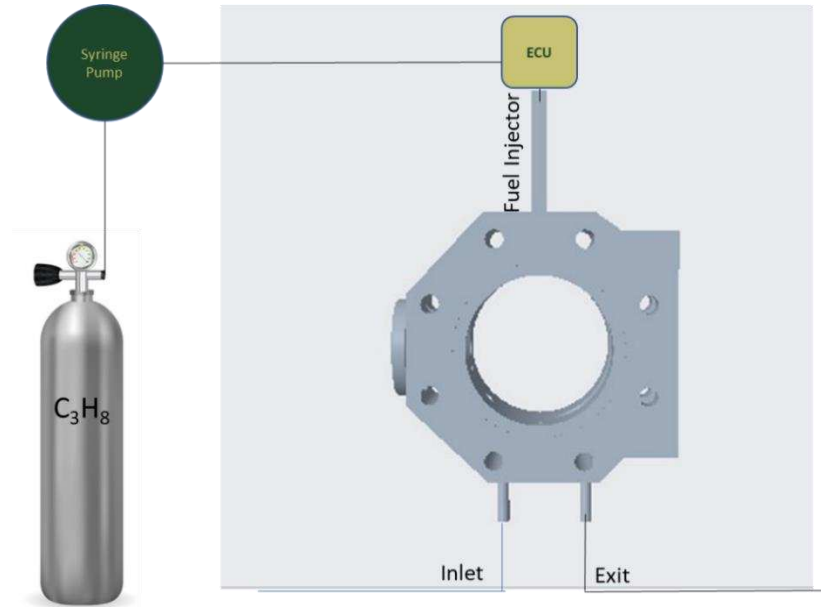


*Figure 2.10: Fueling of the HPSC*

The fuel injector was mounted vertically on the top of the chamber using a custom fuel rail and a fixture that incorporated a temperature-controlled water jacket, as seen in Figure 2.1a. The water jacket can heat the fuel to a desired temperature by utilizing a circulating pump, a 1 kW heater, a temperature controller, and a thermally insulated bath of glycol, as seen in Figure 2.1c, accurately within -0.5 to 4.7 K of error. The injector was pressurized using a ISCO 360D high-pressure syringe pump (labeled C in Figure 2.1a). The ambient pressure inside the HPSC was regulated using pressurized nitrogen gas and a vacuum pump, well within the margin of experimental error. The HPSC was fitted with an absolute pressure transducer and thermocouples mounted on the metal block of the chamber to monitor and acquire the instantaneous chamber conditions through a LabVIEW virtual instrument interface. The corresponding temperature was controlled via high-power-density cartridge heaters embedded in the body of the HPSC and tape heaters wrapped around the silica windows, within -5 to 10 K of error. Before each injection event, the HPSC was purged with pressurized nitrogen gas to inhibit the oxidation of the fuel, making the ambient conditions non-reactive. A combination of o-rings and gaskets were used to seal the chamber under high ambient pressures.

To test the controllability of the temperature around the tip of the fuel injector, as it is one of the major boundary conditions in identifying the state of the spray in computation modelling, an experiment was designed to measure the temperature gradient across the spray chamber using a k-type thermocouple with and without the cooling jacket on. From the results shown in Figure 2.11a and Figure 2.11b, it was evident that the temperature around the injector tip varied strongly from the gas temperature measured at the bottom of the chamber. These effects amplified when the cooling jacket was turned on. To minimize the error in modelling and reporting of the data, a k-type thermocouple was bent around the fuel injector tip to measure the localized temperatures as seen in Figure 2.11c.

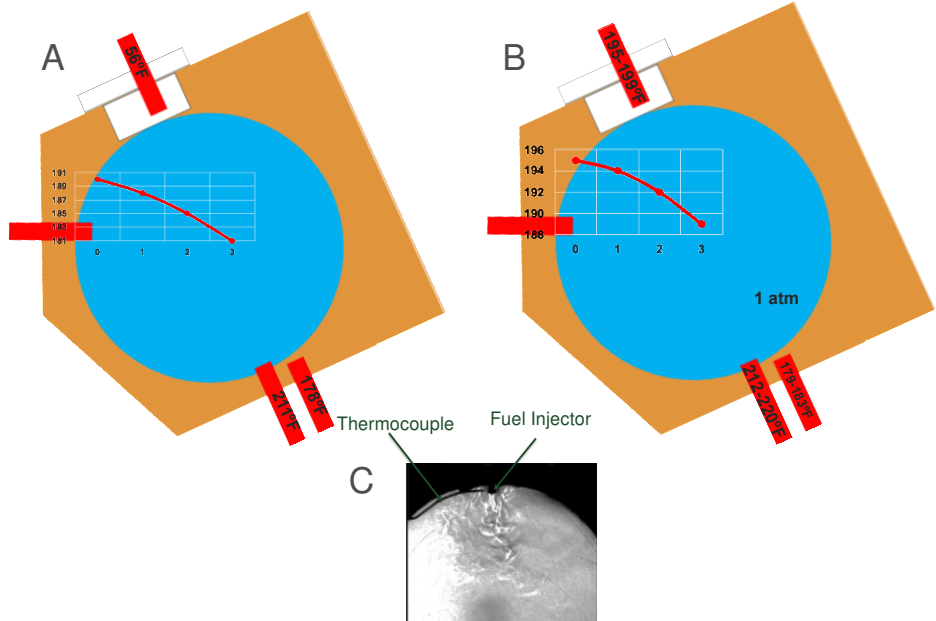


*Figure 2.11: A). Temperature Gradient in HPSC with Cooling Jacket ON, B). Temperature Gradient in HPSC with Cooling Jacket OFF, and C). Thermocouple installation around the fuel injector tip.*

#### 2.1.1.6. Test Conditions

Table 1 includes an array of test conditions specified by ECN that have been tested in prior literature and are standards within the ECN community [4], [28], [102]–[104]. These test conditions are denoted as G2, G2C, G3, and G3C. G2 conditions are representative of an early injection event creating a homogenous mixture, whereas, G3 conditions represent part-load, throttled, early injection conditions in a DI engine cylinder. Iso-octane and propane are widely used as surrogates for gasoline and LPG fuels, respectively [4],

[101], [105]. As many studies have explored the spray morphology and mixing processes of iso-octane using the ECN Spray G fuel injector, iso-octane was also used to verify the experimental setup [27], [106], [107].

*Table 1: Test matrix including Engine Combustion Network's identified experimental conditions [4], [28], [102]–[104].*

Control Parameter	Test Conditions			
	G2C	G2	G3C	G3
Fuel	Iso-octane and Propane			
Injector	Spray G – 8-hole Axisymmetric			
Electric Injection Duration [μsec]	680			
Actual Injection Duration [μsec]	870			
Ambient Temperature ( $T_{amb}$ ) [K]	293	333	293	333
Fuel Temperature ( $T_{fuel}$ ) [K]	293	363	293	363
Ambient Pressure ( $P_{amb}$ ) [Bar(a)]	0.5	0.5	1	1
Injection Pressure ( $P_{inj}$ ) [Bar(g)]	200			

As shown in Figure 2.12a, the defined testing conditions include sub-atmospheric conditions to replicate a homogenous, full-load, early injection event observed in direct injection engines, and high-pressure cases that correspond to late injections or boosted engines. These conditions are also marked on the in-cylinder pressure trace (Figure 2.12b) [13], corresponding to different regimes of engine operations. Testing was carried out at various engine relevant temperatures for iso-octane (a surrogate for CNG) and propane (surrogate of LPG).

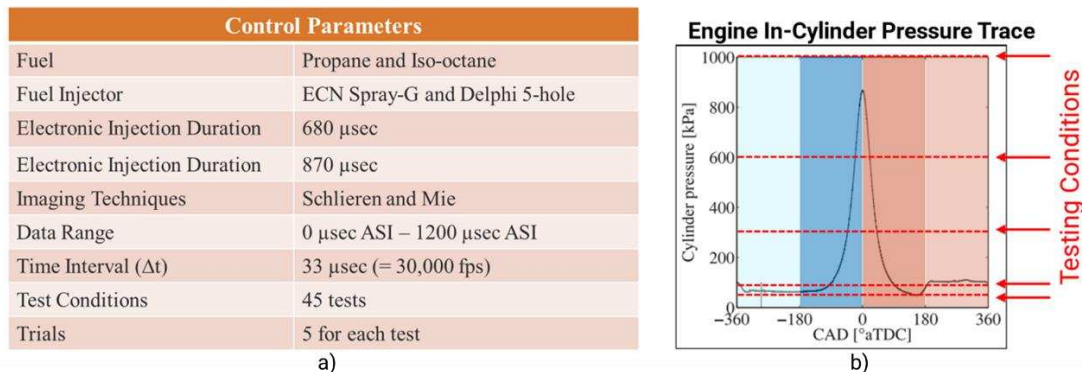


*Figure 2.12: a) Extended test matrix including Engine Combustion Network's identified experimental conditions and high-pressure engine relevant conditions. b) Testing conditions indicated on an in-cylinder pressure case to demonstrate the range and applicability of the testing conditions [13].*

## 2.1.2. Injection Testing

### 2.1.2.1. Setup and Methods and Data Outputs

*Table 2: Test Matrix of Current Profile Optimization*

Injector	Delphi 5-hole #2
Fuel	Propane
Injector Pressure	172 bar
Chamber Pressure	0.855 bar
Injection Duration	11 ms
Peak Current	10 A - 25 A
Hold Current	2 A - 15 A
Peak Duration	0 - 11 ms

To further analyze the performance of 5-hole injectors manufactured using different machining techniques, additional injection rate testing was done for an array of engine relevant conditions and timing to optimize the current profile and injection pressure. Table 2 contains the test matrix for the empirical testing for current profile optimization. As seen in Table 2, all parameters except the peak current, hold current and peak duration were held constant. Only one input of the current profile was varied at a time and the injection rates were measured at those conditions. First the peak current was optimized, then the hold current and finally the peak duration of the current profile was optimized to maximize the injection rate of propane.

Table 3 presents the test matrix to study the dependence of injection rate on injection pressure for both propane and iso-octane. Both these fuels were tested to get a relation between the flow rates of the two as many injector manufacturers only have the injection rate measured for iso-octane but not for propane. Like Table 2, Table 3 shows all the parameters that were held constant, including the current profile inputs which were kept at the optimized current and duration from previous tests, besides the injection pressure.

*Table 3: Test matrix to study the effect on injection pressure on injection rates for propane and iso-octane.*

Injector	Delphi 5-hole #4
Chamber Pressure	0.855 bar
Injection Duration	11 ms
Peak Current	15 A
Hold Current	7 A
Peak Duration	500 $\mu$ s
Fuel	Propane and Iso-octane
Injection Pressure	100 -350 bar

## 2.2. Optical Diagnostics

To compare the experimental data collected using optical diagnostics techniques and the numerical spray simulations, a set of parameters including vapor and liquid spray penetration lengths, widths, and speeds, were utilized to map out the spray morphology for an effective qualitative and quantitative comparison and model validation. These measurements were collected at engine-like conditions using imaging techniques such as high-speed Schlieren and planar Mie scattering.

### 2.2.1. High-Speed Schlieren Imaging

Schlieren imaging is a well-established, line-of-sight technique that is commonly used to visualize inhomogeneities in the refractive index of a transparent medium, created by gradients in the corresponding density field. This technique is commonly used in literature for both qualitative visualization and quantitative fuel spray measurements, such as vapor phase penetration [10], [12], [23], [32].

Figure 2.13a demonstrates a schematic of the high-speed Schlieren setup used to visualize the fuel injection events. A continuous, 200-lumen white LED was collimated through the HPSC by a 150 mm parabolic mirror of 750 mm focal length and received by an identical parabolic mirror placed in a z-type configuration. A knife-edge was used as the schlieren cut-off at the focal point of the converging mirror to amplify the contrast and intensity variations. The images were finally sized with a 50 mm plano-convex achromatic lens of 150 mm focal length and acquired using a Photron FASTCAM SA5 high-speed camera.

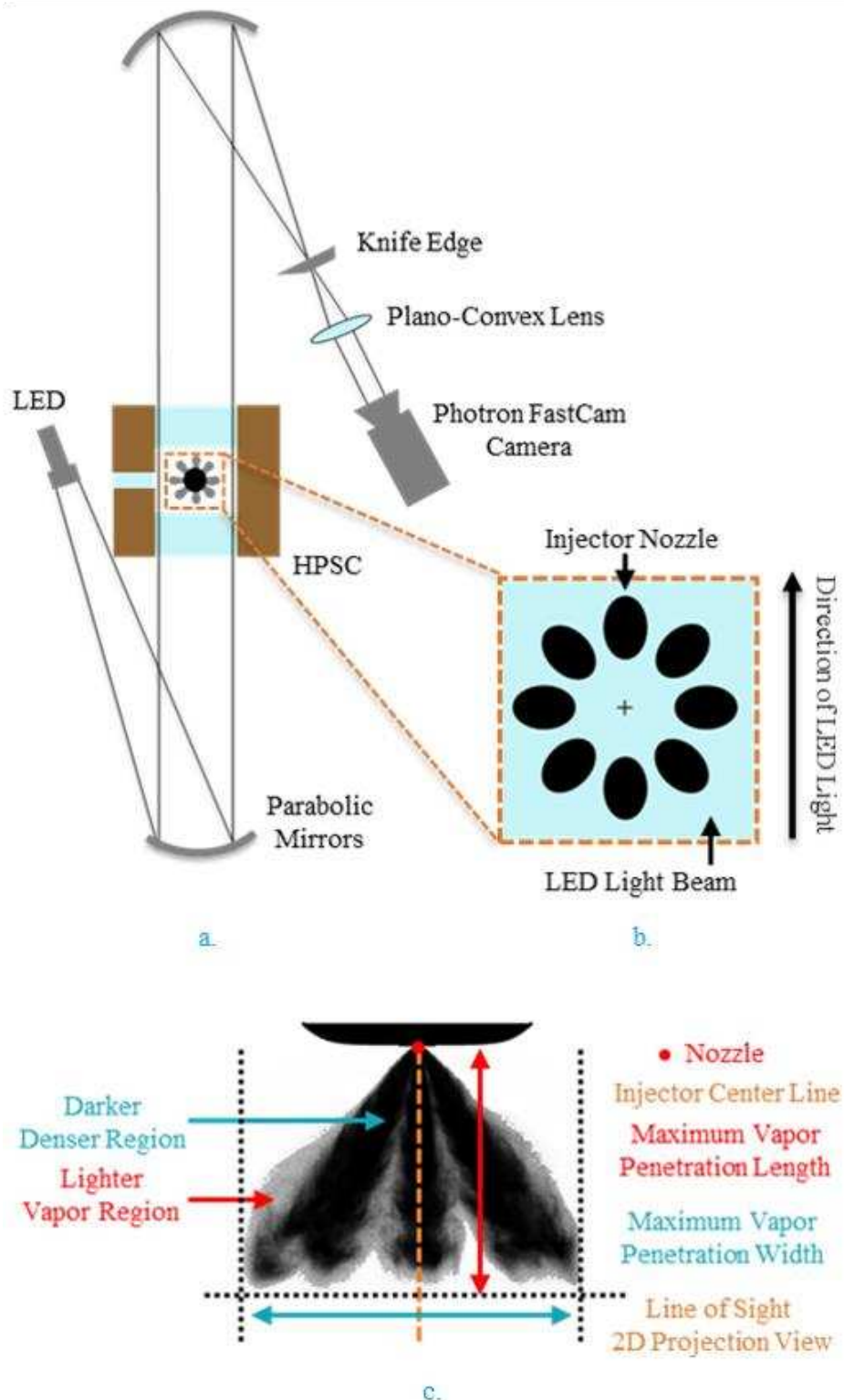


Figure 2.13: (a) Schematic of the top-view of Schlieren imaging setup, (b) Spray-G injector nozzle-alignment relative to the LED light, and (c) resulting Schlieren spray image, features, and nomenclature.

The corresponding imaging frequency was set to 30,000 frames per second, i.e., 33  $\mu$ s between frames, to record schlieren images free of undesired flow features, e.g., dynamic pressure waves. The high-speed schlieren images, with a spatial image resolution of 298  $\mu$ m/px capturing 376 x 640 pixel images, were recorded for a range of chamber and fuel conditions to study the axial vapor penetration length, width (as shown in Figure 2.13c), and penetration rate of the spray. An external delay generator was deployed to sync the Spray G injector and the Photron camera.

Schlieren images were scaled within experiment and between experiments to have a consistent light intensity for the entire data set and compensate for any light fluctuations caused by the LED. Once scaled, the background from each experiment was subtracted from the respective set of experiments, to define the boundaries of the spray clearly. However, background subtraction produced undesired artifacts in the spray core of the image, which was fixed by replacing the non-zero pixels of the image by the corresponding original raw image pixels. This helped to enhance the resolution and fix spray defects with minimal manipulation to raw data. Once processed, maximum axial vapor penetration lengths and maximum normal penetration widths, as seen in Figure 2.13c, were measured using simple edge finding algorithms in MATLAB, and plotted with respect to time. The vapor penetration speed was calculated by taking a first-order derivative with respect to time of the formally measured maximum penetration lengths. Three tests were taken for each test condition and the collected data was averaged to capitalize repeatability and increase accuracy of the measurements; the spray was imaged for 1200  $\mu$ s ASI for each condition. These measurements help to provide detailed quantitative analysis in addition to the qualitative Schlieren images characterizing the spray morphology.

It is important to note, Schlieren provides a global image of both vapor and liquid regions of the spray. Therefore, the 3-dimensional spray structure of an 8-hole injector (Figure 2.13b) is accumulated into one plane, decreasing plume-to-plume distinction and resolution. Another key feature of Schlieren is that the light intensity gradients correspond to the density gradients in the spray. This, however, becomes challenging for a multi-phase spray, for a fuel such as propane, as no clear distinction between liquid and vapor regions can be observed, as seen in Figure 2.13c. Hence, Schlieren is used as a preliminary imaging

technique to visualize the overall spray morphology but, also introduces the need for an advanced diagnostic technique to compensate for mentioned limitations of Schlieren imaging.

### ***2.2.2. Planar Mie Scattering Imaging***

Mie scattering imaging is an elastic light scattering technique used extensively in prior literature to measure liquid penetration through a medium. When a spray is exposed to a specific wavelength of light, the liquid region scatters light in all directions, but the vapor regions do not illuminate. Hence, Mie scattering imaging is often used to capture the liquid regions of the spray [12], [16], [33], [34]. Coupled with Schlieren imaging, Mie can provide a strong comparison amongst the liquid regions, high density vapor regions, and low-density vapor regions. Like Schlieren, Mie scattering captures the liquid regions of the spray globally, i.e., no clear distinction between each plume can be observed. This study utilizes planar Mie scattering to increase the plume-to-plume distinction and enhance the resolution of individual plume penetration morphology.

A custom Nd: YAG laser was used to produce a 532 nm beam with 25 ns pulse width and 7 mJ of energy per shot. The setup for Mie testing consisted of two 50 mm Nd: YAG mirrors designed to reflect 532 nm light to the height of the injector tip. The setup also included two cylindrical optics: a converging lens with a focal length of 1000 mm, and a diverging lens with a focal length of -75 mm as shown in Figure 2.14a, to create a thin laser sheet, 100  $\mu\text{m}$  thick, bisecting the front nozzle of the fuel injector as seen in Figure 2.14b. The Mie laser sheet in Figure 2.14c was used to precisely image the spray structure of the individual plumes injected by the front and back nozzles in the plane of the laser sheet, represented in Figure 2.14d. Additional optics and equipment were used to regulate and measure the energy of the laser sheet, to finely tune the amount of energy delivered to the spray.

An Andor iStar sCMOS camera was used along with a Vivitar 75-300 mm macro focusing camera lens to capture the spray image with a spatial resolution of 49  $\mu\text{m}/\text{px}$  and image size of 2560 x 2160 pixels at various instances of time, ranging from 25  $\mu\text{s}$  to 1200  $\mu\text{s}$  ASI. Similar to the schlieren timing setup, the camera, the fuel injector, and the laser were synchronized using the external delay generator triggered by

the LECM. The actual laser and camera shot timings relative to the start of injection were measured using an oscilloscope and was found to be within  $\pm 15 \mu\text{s}$ . The Andor camera was gated for 15 ns to capture the center of the laser pulse.

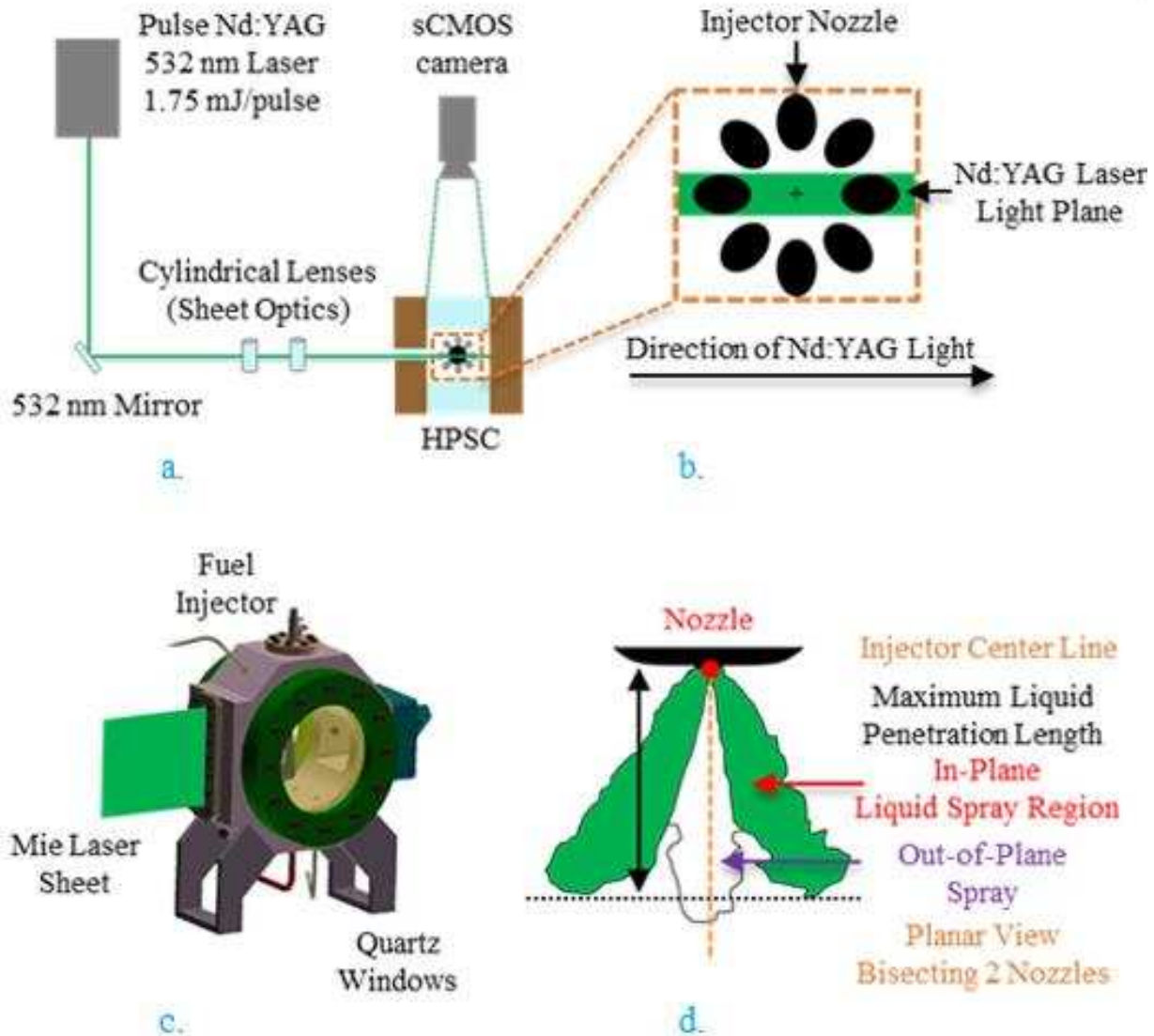


*Figure 2.14: (a) Schematic of the top-view of planar Mie scattering imaging setup, (b) Spray-G injector alignment relative to the laser sheet bisecting the front and back nozzles, (c) isometric 3-D rendering of HPSC and Mie laser sheet, and (d) schematic of corresponding Mie image with illuminated liquid spray plumes in the plane of the laser sheet, and associated nomenclature.*

The collected 16-bit Mie images were processed using a set of standard multi-step image processing techniques. It was observed that the laser energy had a gaussian distribution along the axis of injection; to address this, each Mie image was normalized to make the energy of the laser sheet constant spatially.

Minimum and maximum thresholds were set to eliminate background noise, reflections from the chamber, and secondary Mie scattered light from out of plane spray. Once processed, similar techniques to Schlieren were employed to binarize the spray image and detect edges of the individual plume, i.e., the front plume (left as seen in Figure 2.14d). It was also observed that the laser sheet attenuates as it propagates through the chamber perpendicular to the axis of injection, due to the presence of spray. This, however, did not have an impact on the measurements, as the front edge of the spray was free of this aberration and hence, was used for valuable quantitative measurements. Three iterations of each test condition were performed for all time instances. Once the front edge was defined, the corresponding pixels were calibrated, averaged over three iterations, and then plotted to obtain maximum liquid penetration lengths as a function of time.

### **2.2.3. Planar Laser Induced Fluorescence**

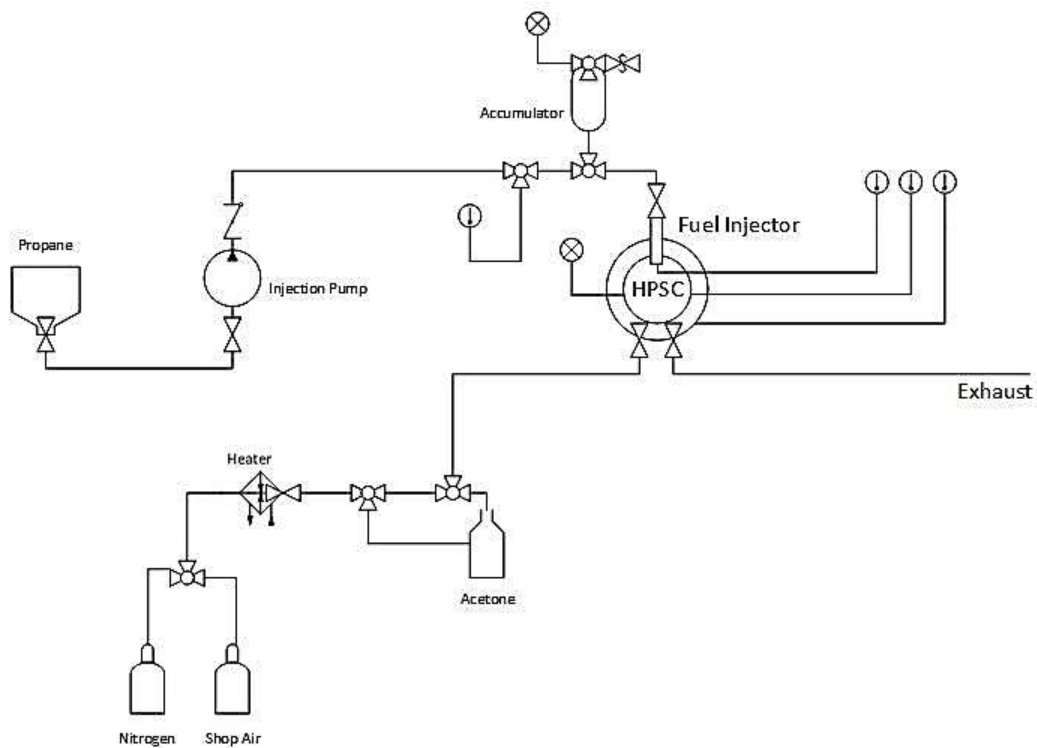


*Figure 2.15: Piping and instrumentation diagram of the high pressure spray chamber including the injection lines, chamber pressurization and temperature controls, and acetone bubble loop in the dashed rectangle.*

An acetone loop was installed in the HPSC assembly, as shown in Figure 2.15 that included an acetone bubbler which can handle high pressures and temperatures to allow for controllable doping of

acetone in nitrogen gas. Acetone doped nitrogen is required to perform planar laser-induced fluorescence imaging of the spray which will be used to quantify the planar vapor penetration lengths and plume specific data.

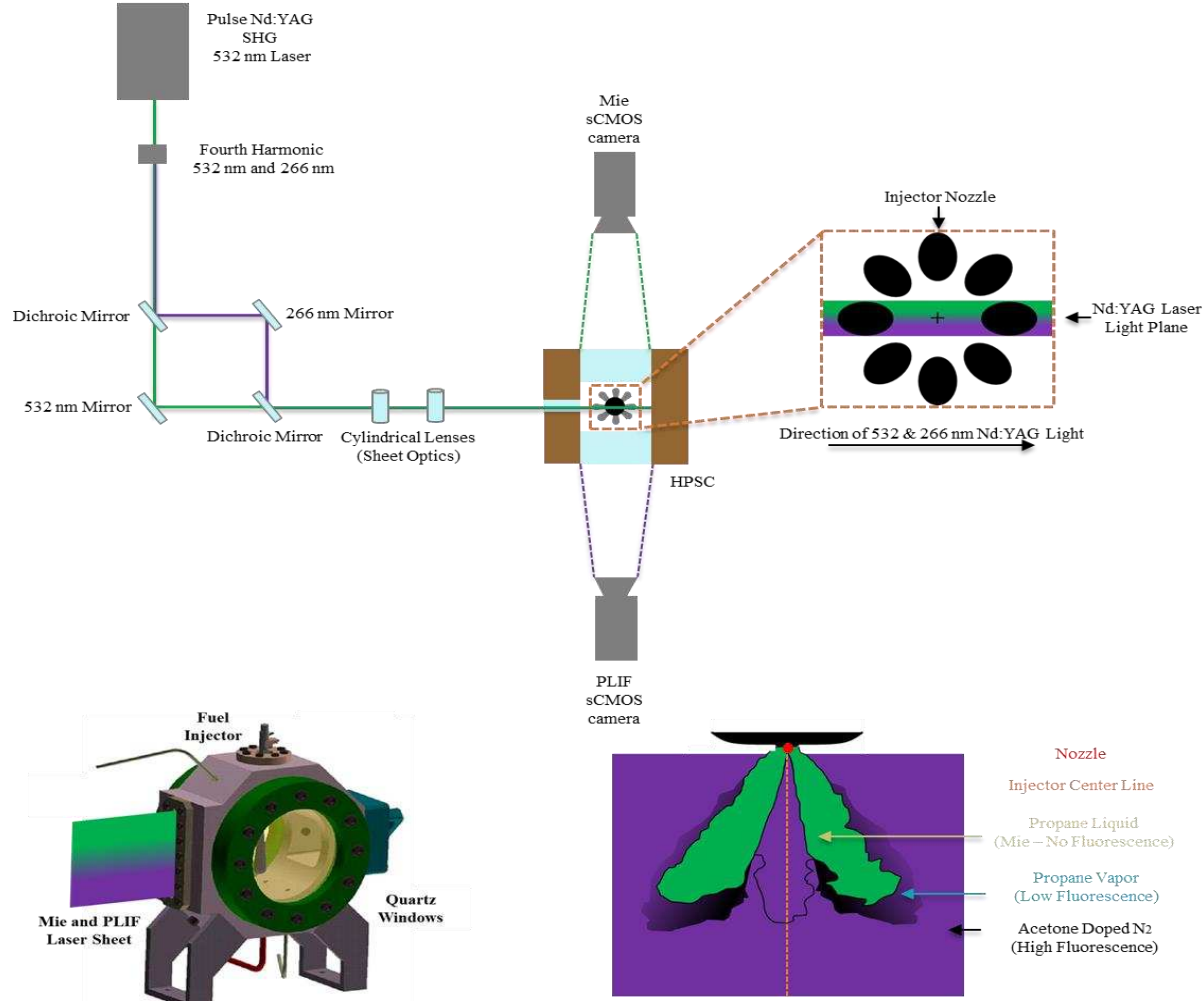


*Figure 2.16: Optical Schematic for simultaneous planar Mie scattering, and planar laser-induced fluorescence, incident laser sheet, and schematic of various planar liquid and vapor data that will be collected using PLIF and planar Mie.*

A fourth harmonic generator (FHG) has been acquired and is installed in the Planar-laser induced fluorescence setup as shown in Figure 2.16. 266 nm light is converted from 532 nm light, generating about 80 mJ light beam. HPSC setup has been updated to incorporate the acetone doping of nitrogen mechanism. The 266 nm light will fluoresce the acetone doped nitrogen gas in the chamber and help define vapor regions produced by the injector spray in the plane. PLIF will also aid in the development of spray models by utilizing the measured vapor penetration length, spray angle, and fuel mixing rates.

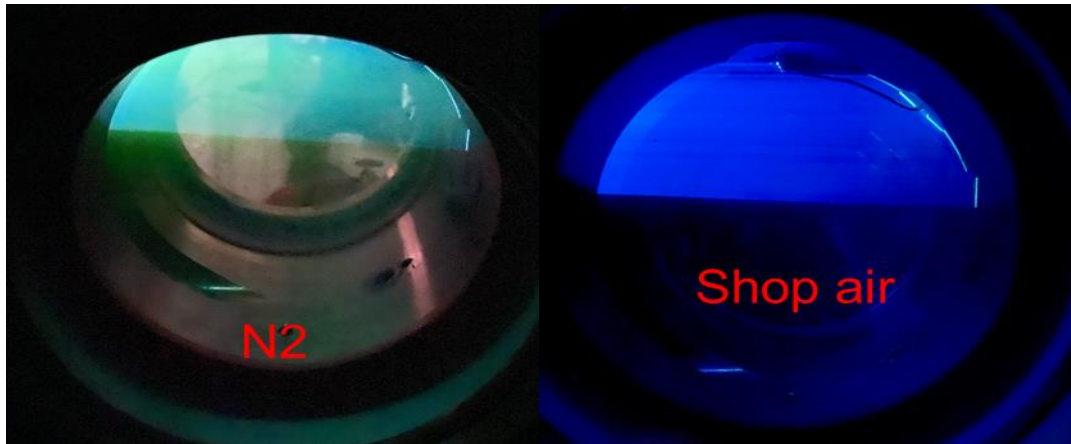


Figure 2.17: Fluorescence and phosphorescence signals captured with PLIF for acetone dope in nitrogen (left), and Fluorescence PLIF signal of acetone doped in air.

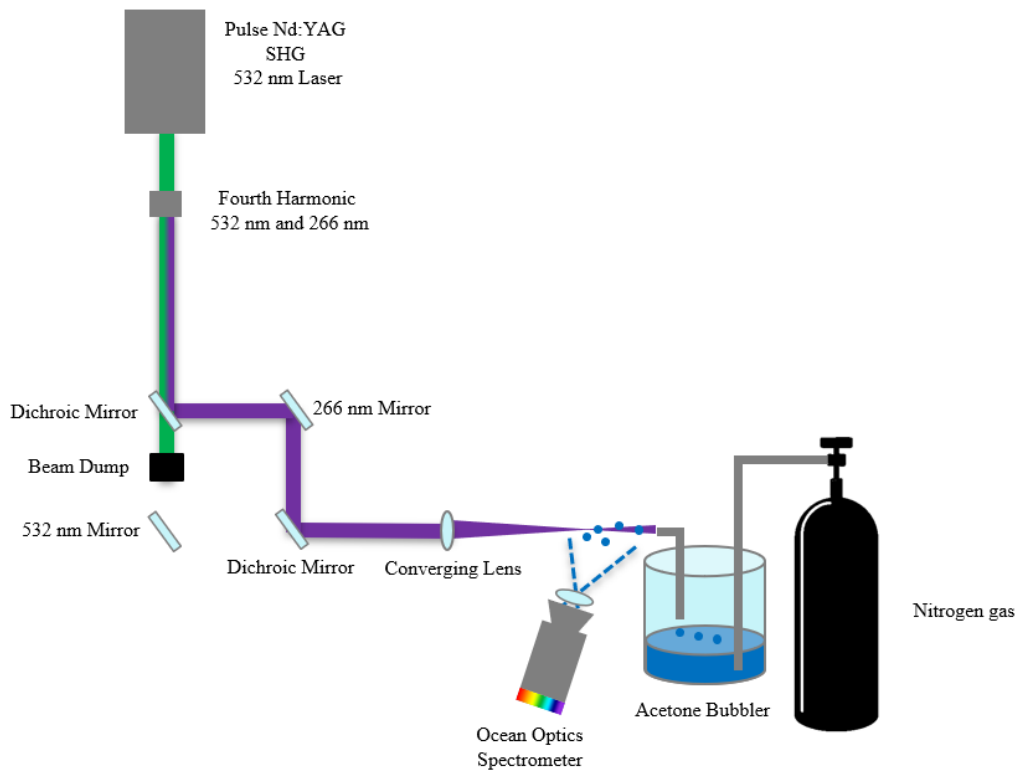


Figure 2.18: Schematic for spectroscopy of acetone doped nitrogen using 266 nm Nd:YAG laser.

Preliminary experiments of PLIF have shown two radiative de-excitation mechanisms in nitrogen gas: fluorescence, and phosphorescence. As observed in Figure 2.17, the fluorescence is blue in color and phosphorescence is green in color. Besides different spectral wavelengths, fluorescence was observed to occur 15 nanoseconds after the laser and was short-lasting, whereas the phosphoresce signal occurred after

1 microsecond and lasted for several microseconds. However, when acetone is doped in air, phosphorescence signals are significantly quenched and only fluorescence is observed. The quenching effect was related to the presence of oxygen, and its diamagnetic nature which favors fluorescence. When intensified CCD cameras were used, none of these phenomena were captured. This could be caused because the camera filters were not capturing the wavelengths observed for these phenomena.

Spectroscopy was done for the acetone planar laser induced fluorescence, using acetone bubbler, 266 nm laser light from Nd:YAG laser, and Ocean Optics Spectrometer to collect wavelength distribution of the PLIF signal. The schematic for the spectroscopy setup is shown in Figure 2.18.

Samples were recorded at 100 Hz for 300 seconds and summed to get an average distribution. However, only the intensities of 266 nm light and 532 nm light were observed, other wavelengths were indistinguishable from noise. The phone videos did however show a blue colored fluorescence zone as shown in Figure 2.19, but the intensity of signal was too low to be detected by Ocean Optics Spectrometer.

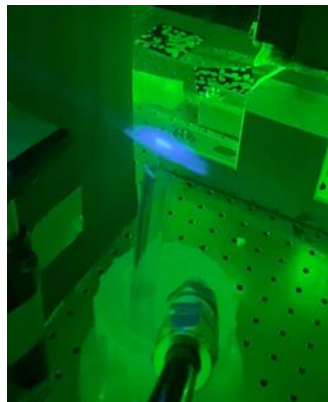


*Figure 2.19: Spectroscopy Image via Phone Camera*

### **2.3. Numerical Spray Simulations**

In this section, the methodologies outlined are the collaborative efforts of Dr. Lorenzo Nocivelli and Dr. Katherine J Asztalos from Argonne National Lab. The objective is to illustrate the practical utilization of experimental findings for the validation and refinement of spray models. The research at Argonne National Lab, conducted in close collaboration with the author, is also detailed in Windell et al. [100]. The simulation campaign was carried out with the commercial CFD software CONVERGE (v3.0)

[108]. The injection was modeled with a two-tiered approach: first, the simulation of the two-phase internal nozzle flow was carried out to provide insight into the trends in the mass flow rates and the initial development of the spray plumes for each fuel; then, the results were used to inform the Lagrangian parcel spray model, which was then implemented to simulate the full HPSC domain.

Both the steps in the simulation campaign were carried out by discretizing the transport equations with spatial second-order accuracy and Euler implicit scheme for the time integration. The velocity-pressure coupling was realized through the pressure implicit with splitting of operators (PISO) method. The following two sections describe the details of the numerical simulation.

### ***2.3.1. Nozzle-Flow Simulation Setup***

The first step taken follows the approach described in the author's previous work [109] to characterize the fuel jet dynamics produced by the nozzles. The nominal geometry of the injector defines the computational system, which was mated with a hemispheric open-outlet boundary, as shown in Figure 2.20. In the resulting domain, the multi-phase flow was handled with a single-fluid mixture model, considering that the relative velocity between the phases was in local equilibrium. With this assumption, a single set of transport equations – mass, momentum, total energy, and species – was solved based on the barycentric velocity of the mixture. The different phases were treated as species – liquid, gas, and fuel vapor – in a multi-component mixture, and the phase change was handled through source terms in the species equation. The magnitude of the source terms was determined with the homogeneous relaxation model (HRM) [98], which assumes that the local and instantaneous vapor quality evolves towards its equilibrium value according to a linear trend, based on a characteristic time scale. The characteristic time scale depends on the properties of the fluids and the local pressure and void fraction values, and its magnitude was determined according to an empirically obtained constant. According to previous results [110], the value of the constant allows to modify the speed of the phase-change, and the behavior of the spray in the near nozzle region. The grid was obtained via the cut-cell method with a base mesh of 240  $\mu\text{m}$ , and it was refined to 15  $\mu\text{m}$  in the regions of interest as shown by the center-plane of the injector reported in Figure 2.20b.

The dynamic grid refinement to track the plume evolution in the open chamber was obtained via adaptive mesh refinement based on the second derivative of the velocity and species mass fraction.



*Figure 2.20: (a) Eulerian nozzle flow CFD domain for the ECN's Spray-G injector, and (b) numerical grid on the centerline at full needle lift.*

For both iso-octane and propane, the needle motion was prescribed according to the X-ray measurement by Sforzo et al. [26], collected for different fuel at previously defined ECN's G2 conditions [28], initializing the motion from a minimum gap of  $6.6 \mu\text{m}$ , according to the setup proposed by Yue [111]. The turbulence was modeled with a large eddy simulation (LES) approach, using the dynamic structure model.

### **2.3.2. Lagrangian Spray Simulation Setup**

The simulation of the spray in the HPSC was obtained with the Lagrangian-Eulerian method and the liquid phase was modeled according to the discrete droplet model [91]. The geometry of the chamber was discretized with the Cartesian cut-cell method (Figure 2.21a), defining a base grid size of 1.6 mm, and relying on adaptive-mesh refinement (AMR) to refine the cells according to the second derivative of velocity and fuel vapor mass fraction, as shown in Figure 2.21b for 500  $\mu\text{s}$  ASI. The transport equations

were defined according to the unsteady Reynolds-average (URANS) framework, and the k- $\epsilon$  RNG was chosen for the turbulence modeling. The Lagrangian spray sub-models involve: Kelvin Helmotz Rayleigh Taylor (KH-RT) model [112] for primary and secondary break-up without the definition of a breakup length, Frössling correlation for phase-change, O'Rourke model [108] to introduce turbulent perturbation, and no-time-counter model [113] for droplet collision and coalescence. Moreover, to introduce the phase-change due to flash-boiling, the model proposed by Adachi et al. [99] is implemented in the code. This model accounts for local and instantaneous super-heat degree of the fuel in the chamber in terms of difference between the local temperature at the saturation temperature of the fuel at the local pressure. The implementation in CONVERGE is reported in previous work by the authors [33]. The spray parcels were initialized with the blob-injector model, which was informed with the results obtained by the nozzle-flow simulation in terms of mass flow rate and droplet momentum, plume direction, and plume angle to best represent the ensuing spray.

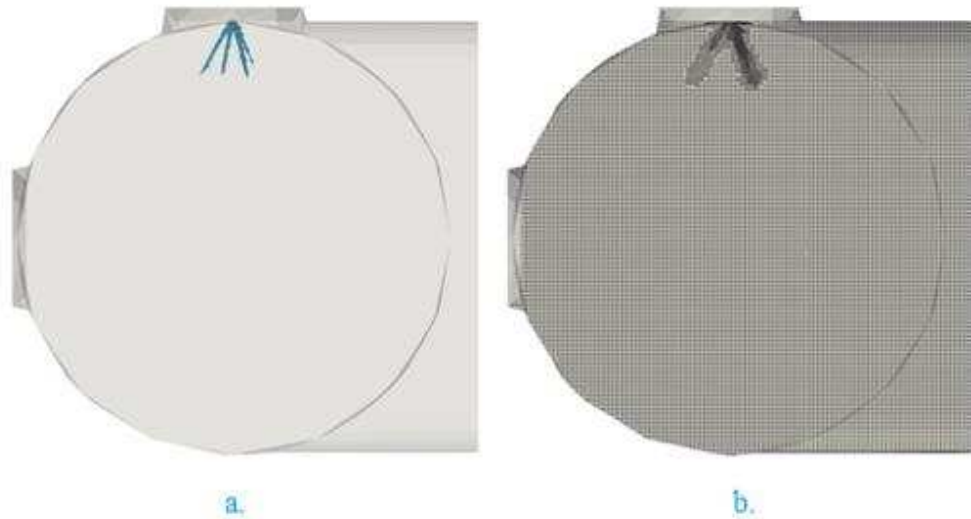


*Figure 2.21: Lagrangian spray CFD domain for the injection in HPSC (a), and (b) numerical grid on the centerline with AMR.*

### 2.3.3. Numerical Spray Processing

Given the unconventional propane spray behavior, where vaporization and collapse play a major role, the numerical spray results were processed to reproduce experimental Schlieren and Mie scattering

data. The two processing routines aim to describe the full spray morphology and the liquid phase development respectively.

The Schlieren images were reproduced by projecting the magnitude of the gradient of the gas-phase density along the line-of-sight, as shown in Figure 2.22a. The resulting 2D data was normalized on its maximum value to provide a qualitative image of the spray morphology as in Equation (2.1).

$$I_{Sch,norm} = \frac{\sum_i^{cell\_X} grad_X(\rho)}{max(\sum_i^{cell\_X} grad_X(\rho))} \quad (2.1)$$

On the other hand, the light scattered from the liquid phase was reproduced by projecting over the line-of-sight, with the frontal area of the spray parcels projected over the thickness of a sampling region representative of the laser sheet, as shown in Figure 2.22b. Then, the obtained 2D projection of the spray parcel frontal area was normalized on its maximum value to produce a qualitative representation of measured scattered light, according to Equation (2.2).

$$I_{norm} = \frac{\sum_i^{N\_parcels} n\_drop_i D_i^2}{max(\sum_i^{N\_parcels} n\_drop_i D_i^2)} \quad (2.2)$$

The location and thickness of the sampling region replicates the experimental setup. The resulting images from both routines are proportional to the measured light intensity trends, but without implementing the laser scattering detailed dynamics, the focus of the validation is set on the boundaries of the spray profiles. To do so, the obtained light intensity profiles are binarized to highlight the fuel jet evolution in the chamber. The vapor penetration was determined by the maximum axial distance computed from binarized images generated with a threshold of  $I_{Sch,norm} > 0.02$ . The proposed comparison is chosen to allow the spray morphology assessment to be consistent with the experiments, and to enable the validated simulation to provide further insight on the vapor and liquid distribution trends.

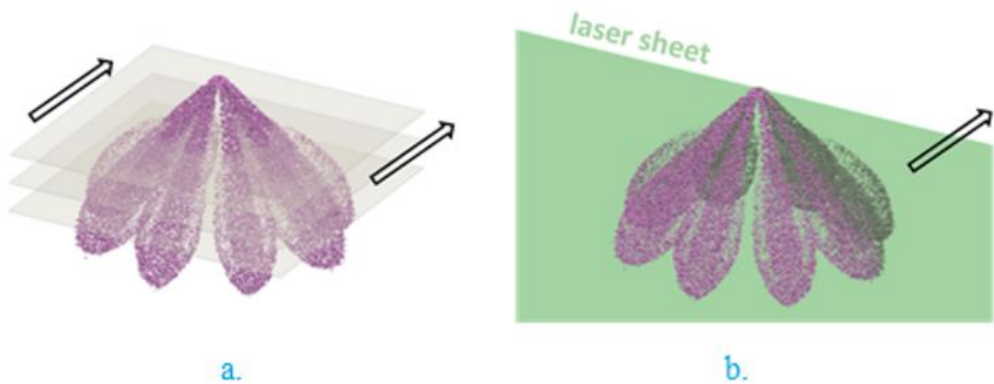


*Figure 2.22: Schematic of the spray simulation processing regions of interest: sampling region representing the (a) planar gradient density sampling of the gas phase to reproduce Schlieren data, and (b) the Mie laser sheet.*

In absence of accurate and reliable flash-boiling vaporization models for Lagrangian sprays, the enhanced atomization and vaporization are obtained by modifying the aerodynamic breakup constants to replicate the phenomena measured experimentally in the high-pressure spray-chamber (HPSC). The simulation has been compared to the HPSC measurements in terms of liquid and vapor morphology through consistent replication of schlieren and Mie-Scattering data, obtaining reasonable agreement across a wide range of operating conditions. Full collapse of the plumes is obtained for flashing sprays and a more conventional spray behavior is report when  $P_{amb}$  is higher. The influence of the injector geometry is captured in the injection dynamics and Lagrangian spray models for the CFD software CONVERGE-3.0 have been generated to be incorporated in engine simulations.

## CHAPTER 3 - RESULTS AND DISCUSSION

This section presents experimental and numerical measurements mapping out the spray morphology for iso-octane and propane over a range of engine-like conditions as mentioned above. The results from the experimental spray visualization techniques feed the numerical simulation results and aid in the validation and selection of a correct modeling technique, using a strong comparison of the qualitative and quantitative experimental results.

### 3.1. Experimental Spray Visualization Techniques Results

#### 3.1.1. *Experimental High-Speed Schlieren Results*

Figure 3.1 shows schlieren imaging for iso-octane and propane at G3C and G3 conditions at three timesteps: 200  $\mu$ s, 500  $\mu$ s, and 750  $\mu$ s ASI. As seen in Figure 3.1a - f, iso-octane has a wide injection angle, a typical spray pattern, and three individual plumes are clearly distinguishable. Majority of the spray appears to be symmetric at presented times stamps for both conditions. It can be seen that the spray structure, penetration lengths and widths of iso-octane are minimally affected by the increasing temperature from G3C ( $T_{fuel} = T_{amb} = 20^{\circ}\text{C}$ ) to G3 ( $T_{fuel} = 90^{\circ}\text{C}$  and  $T_{amb} = 60^{\circ}\text{C}$ ). There is a clear distinction between darker/liquid spray cores and lighter/vapor regions for iso-octane.

Whereas propane in Figure 3.1g - l, has a much narrower overall injection angle and plume-to-plume interactions are prevalent creating a large singular jet. The spray structure of propane is observed to have a strong dependence on temperature. At colder cases (G2C and G3C), Figure 3.1g - i, the spray starts with a wide angle and less vaporization, but the multiple plumes of the spray collapse into a singular jet as it propagates through time. This influence of temperature increases in orders of magnitude when the fuel is preheated and injected into hotter ambient conditions (G2 and G3), as seen in Figure 3.1j - l.

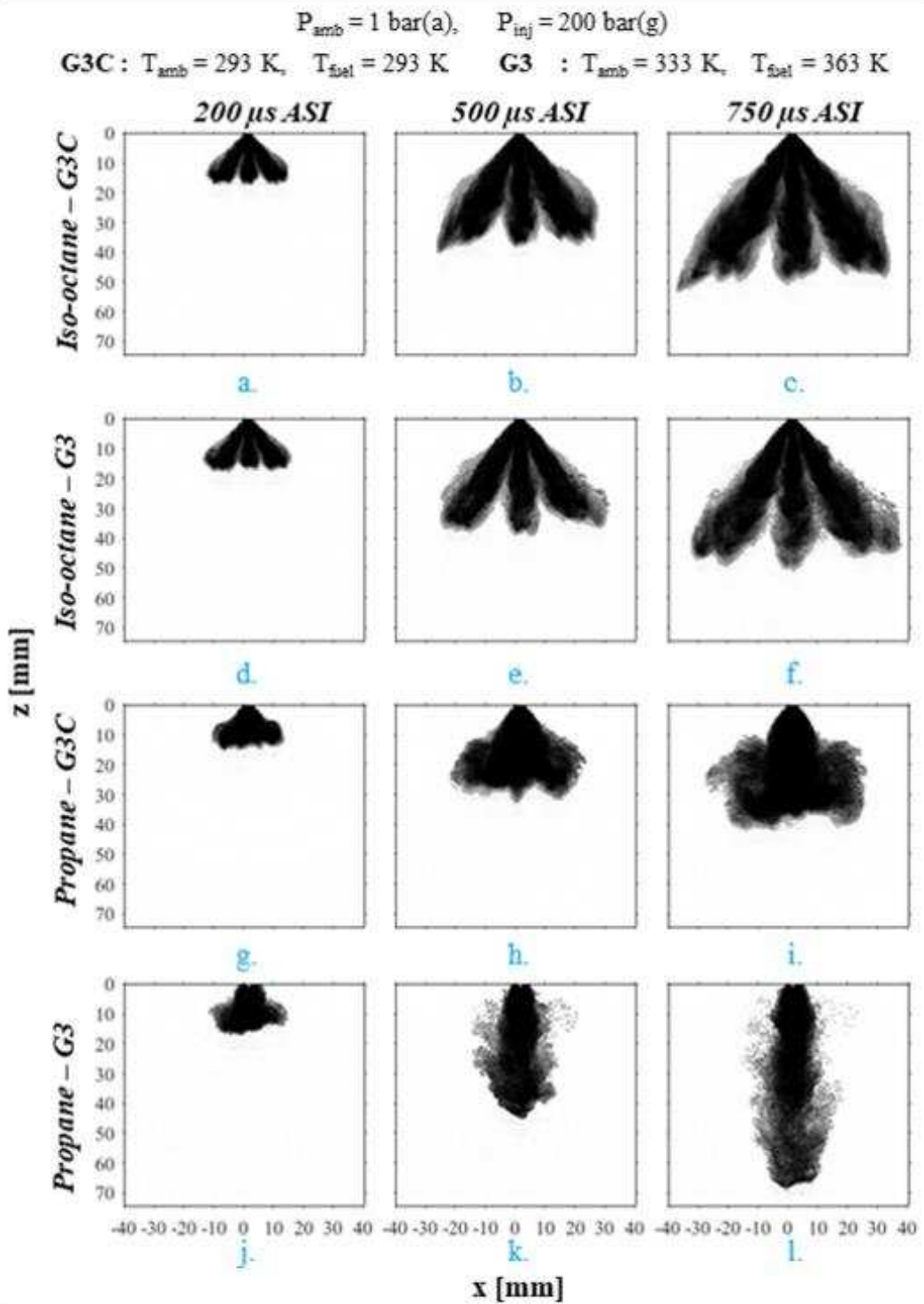
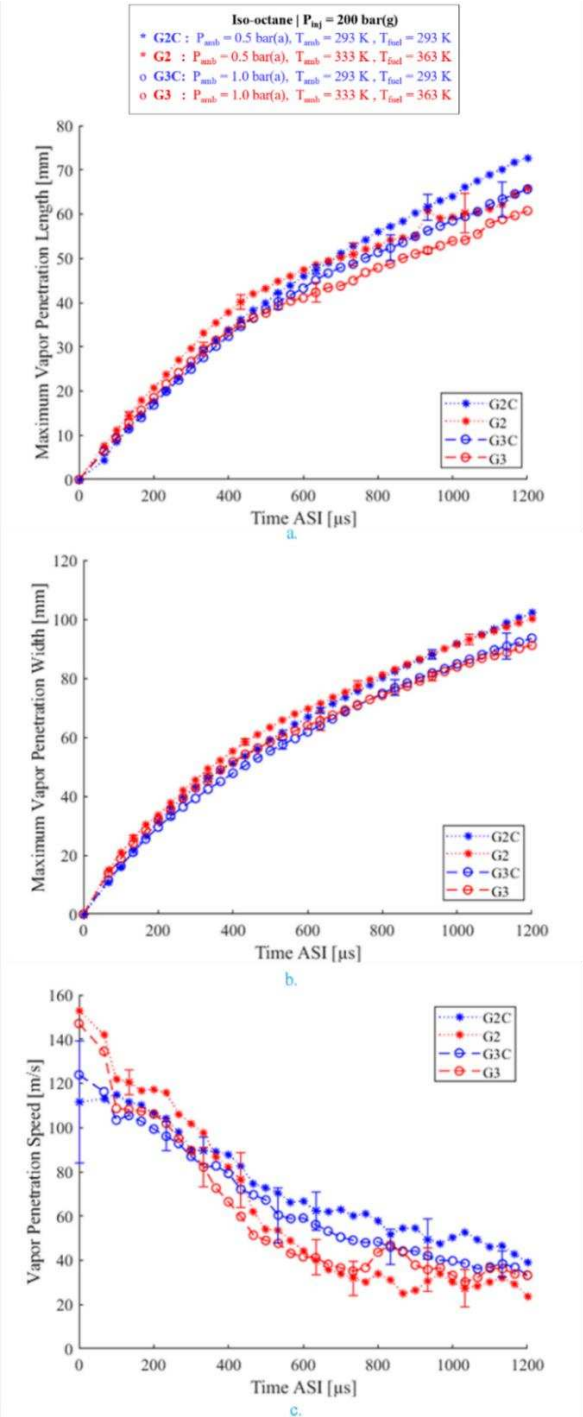


Figure 3.1: High-speed Schlieren images at various denoted timesteps (across) after the start of injection for various fuels and conditions (down), namely: (a) - (c) for iso-octane at G3C, (d) - (f) for iso-octane at G3, (g) - (i) for propane at G3C, and (j) - (l) for propane at G3 condition, respectively.

Contrary to the behavior observed in Figure 3.1g - i, propane's collapse is more evident at G3 conditions, seen in Figure 3.1j - l, as the width of the jet is narrower and stays consistent throughout the injection duration; propane also propagates further axially at hotter conditions. The axial penetration lengths of propane at G3 are much greater than iso-octane for all tested conditions. No clear distinction between liquid regions and vapor regions can be made for propane at both conditions.

The quantitative penetration measurements of iso-octane, agree strongly with the qualitative analysis presented. Penetration lengths and widths overlap well within the margin of experimental error throughout the injection duration, as seen in Figure 3.2a and Figure 3.2b. Small deviation can be observed after the end of injection, i.e., 870  $\mu$ s ASI, where differences in penetration lengths and widths start to appear and are within  $\pm 7.5$  mm. The penetration lengths increase in the order of G3 < G2  $\approx$  G3C < G2C, i.e., penetration lengths are inversely proportional to temperature and pressure. However, when observing penetration widths, temperature has negligible effects, whereas the widths are inversely proportional to pressure after the end of injection. Iso-octane, as seen in Figure 3.2c, is observed to have a high velocity at higher temperatures towards the start of injection but decreases at a faster rate compared to colder temperatures, resulting in slower propagations at the end of injection.

Unlike iso-octane, propane has a clear trend for penetration lengths and the influences of various conditions. The axial penetration length, as observed in Figure 3.3a, is seen to be increasing for the conditions in the order of G3C < G2C < G3 < G2, i.e., inversely proportional to pressure and directly proportional to temperature. The direct proportionality with temperature is unique to propane. In general, propane is seen to propagate farther than iso-octane by approximately 20 mm more at 1200  $\mu$ s. However, the penetration widths of propane, presented in Figure 3.3b, are significantly less as compared to iso-octane; approximately 50 mm less at 1200  $\mu$ s. This agrees well with the qualitative images (Figure 3.1g – l) which show a narrower singular jet for propane.



*Figure 3.2: Measurements for iso-octane including a) maximum axial vapor penetration length, b) maximum transverse vapor penetration width, and c) vapor penetration speed of iso-octane calculated using the time derivative of the maximum axial penetration length at corresponding conditions and timesteps measured using high-speed Schlieren imaging. Error bars are included at suitable timestamps for improved legibility. Mean error of  $\pm 2.0$  mm in vapor penetration lengths,  $\pm 1.8$  mm in vapor penetration widths, and  $\pm 8.3$  m/s in vapor speeds were observed over all tests for iso-octane.*

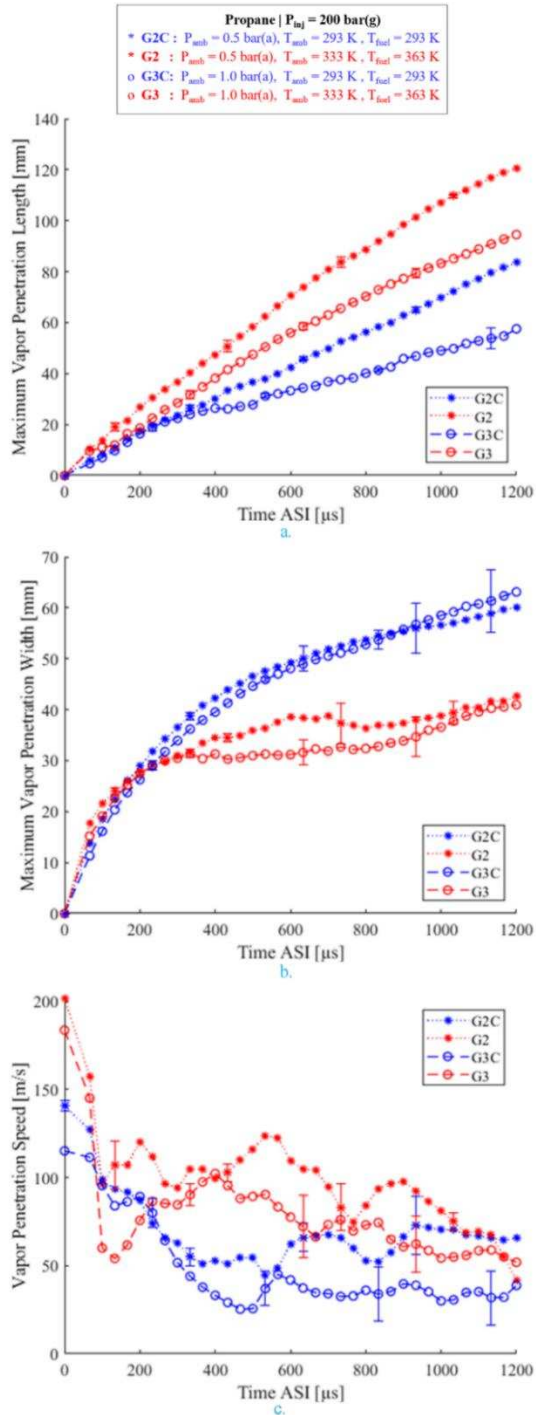


*Figure 3.3: Measurements for propane including a) maximum axial vapor penetration length, b) maximum transverse vapor penetration width, and c) vapor penetration speed of propane calculated using the time derivative of the maximum axial penetration length at corresponding conditions and timesteps measured using high-speed Schlieren imaging. Error bars are included at suitable timestamps for improved legibility. Mean error of  $\pm 1.5 \text{ mm}$  in vapor penetration lengths,  $\pm 2.4 \text{ mm}$  in vapor penetration widths, and  $\pm 8.6 \text{ m/s}$  in vapor speeds were observed over all tests for propane.*

Not only the widths are smaller, but propane also shows an influence of temperature, not pressure which was seen in iso-octane. These features of a narrower, longer jet of propane also impact the penetration speeds plotted in Figure 3.3c, which are approximately 30 m/s higher than that of iso-octane. Hotter temperature conditions (G2 and G3) have a higher initial axial velocity than colder temperatures (G2C and G3C), and this trend is generally consistent through the duration of the spray. The unique features observed of the propane's vapor penetration velocity (Figure 3.3c) are a steep drop at 100  $\mu$ s for each condition, and pulsating velocities after.

### ***3.1.2. Experimental Planar Mie Scattering Results***

Planar Mie scattering enhances the liquid regions of a singular spray plume which provides finer resolution of the spray morphology. Figure 3.4 shows planer Mie imaging of iso-octane and propane at G3C and G3 conditions at three timesteps: 200  $\mu$ s, 500  $\mu$ s, and 750  $\mu$ s ASI. As seen in Figure 3.4a - f, a singular plume of iso-octane is observed that has wide injection angle relative to the nominal axis of injection, i.e., vertical, and a distinct narrow liquid core for the front plume. It is also important to note that only one plume is seen in the plane of the laser sheet; this corresponds to the aforementioned effect of laser attenuation.

It is observed that the liquid penetration length is influenced by the temperature difference in G3C and G3 conditions, however, the injection spray angle and horizontal spray penetration remain unaffected. These results from planar Mie agree strongly with the results obtained for iso-octane using Schlieren imaging (Figures 7a – 7f). Figure 3.4g – i and Figure 3.4j – l, present planer Mie scattering imaging for propane at G3C and G3 conditions, respectively. Unlike iso-octane, propane in most presented cases is observed as a singular jet. This jet is unlike the singular front plume observed for iso-octane and is seen to be brighter, longer, more axial, and with a wider liquid core. This, however, is not true for propane at G3C conditions, as seen in Figure 3.4g, a singular liquid spray plume is observed, similar to iso-octane. But, as the spray progresses, shown in Figure 3.4h and Figure 3.4i, the spray structure begins to resemble a large singular spray jet, similar to that seen in the Schlieren imaging. At hotter G3 conditions, the liquid penetration length of propane is also observed to be much longer than that at colder temperature conditions.

The penetration length of propane is also observed to be longer than that of iso-octane for all tested conditions.

For iso-octane, as seen in Figure 3.5a, the liquid penetration lengths for all conditions overlap until 400  $\mu$ s ASI, with minor deviations approaching the end of injection. However, for hotter conditions (G2 and G3), liquid penetration lengths begin to fall around 800  $\mu$ s and become zero at 1200  $\mu$ s. This shows that temperature is inversely proportional to liquid penetration lengths for iso-octane but, only for spray propagation after the end of injection.

Unlike iso-octane, propane has a clear trend for penetration lengths and the influences of various conditions. The liquid penetration length is seen to be increasing for conditions in the order of G3C < G2C < G3 < G2, which is inversely proportional to pressure and directly proportional to temperature. This trend is identical for vapor penetration of propane as observed in Schlieren imaging. Similar to iso-octane, at hotter temperature conditions, propane's liquid penetration length, as seen in Figure 3.5b, begins to fall sharply at 1000  $\mu$ s, while at colder temperature conditions (G2C and G3C) the penetration lengths continue to increase. At colder conditions, liquid propane is seen to propagate farther than liquid iso-octane by approximately 15 mm more at 1200  $\mu$ s, however, at hotter conditions no liquid is observed for both fuels at 1200  $\mu$ s.

Both vapor and liquid penetration lengths are crucial measurements that define the spray morphology and provide useful information describing how the spray propagates through time. Figure 3.6a and Figure 3.6b present iso-octane and propane's vapor and liquid penetration lengths respectively, plotted at G3C and G3 conditions for a comparative analysis. For both the conditions, it is observed in Figure 3.6a that for iso-octane, the vapor leads the liquid by a small margin for the entire spray duration. However, for G3 condition, i.e., the hotter case, the liquid starts to fall significantly after the end of injection, causing the liquid-vapor difference to increase sharply. Unlike iso-octane, a clear distinction can be made between the penetrations for hot and cold conditions for propane, as observed in Figure 3.6b.

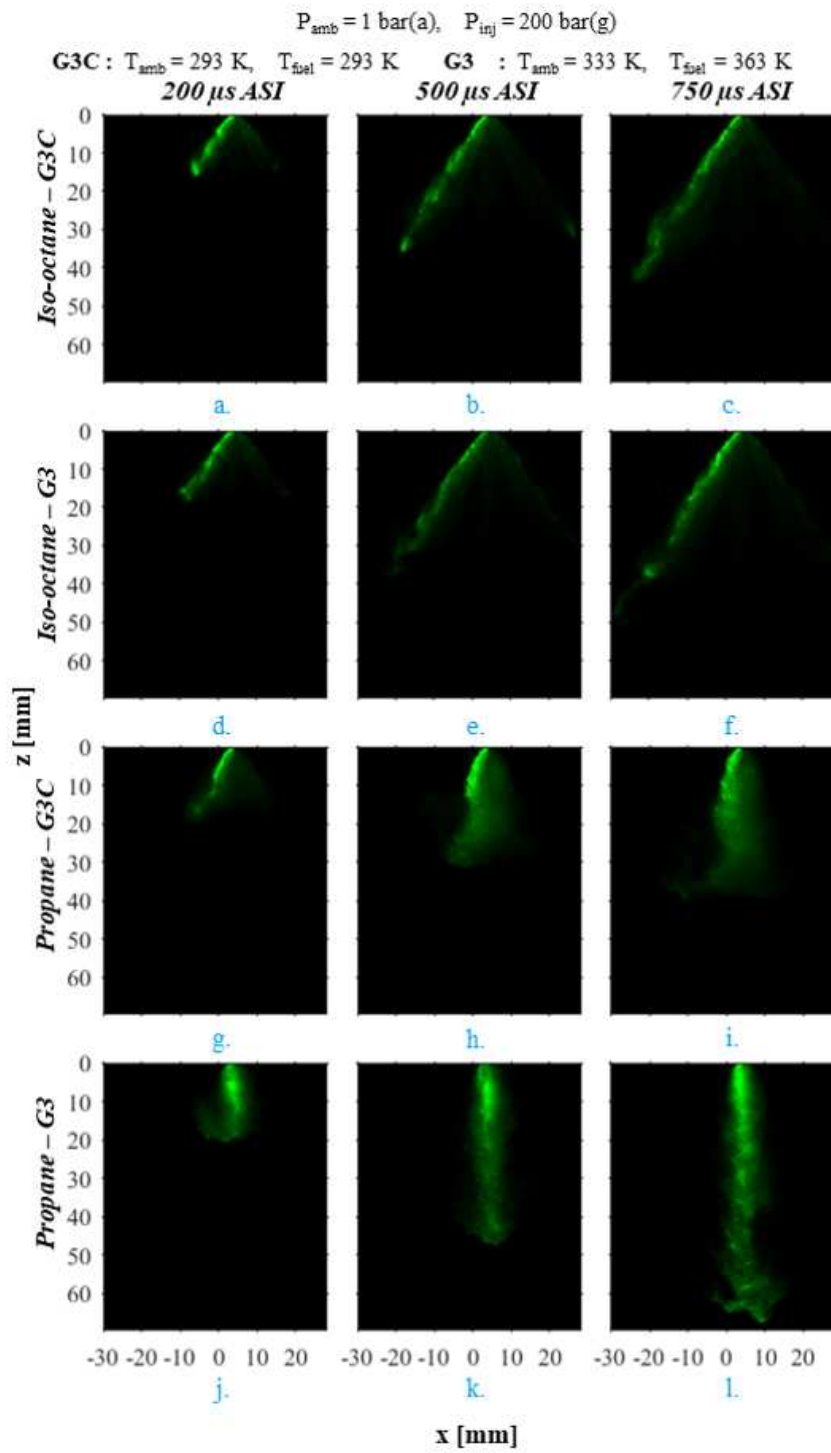


Figure 3.4: Planar Mie scattering images at various denoted timesteps (across) after the start of injection for various fuels and conditions (down), namely: (a) - (c) for iso-octane at G3C, (d) - (f) for iso-octane at G3, (g) - (i) for propane at G3C, and (j) - (l) for propane at G3 condition, respectively.

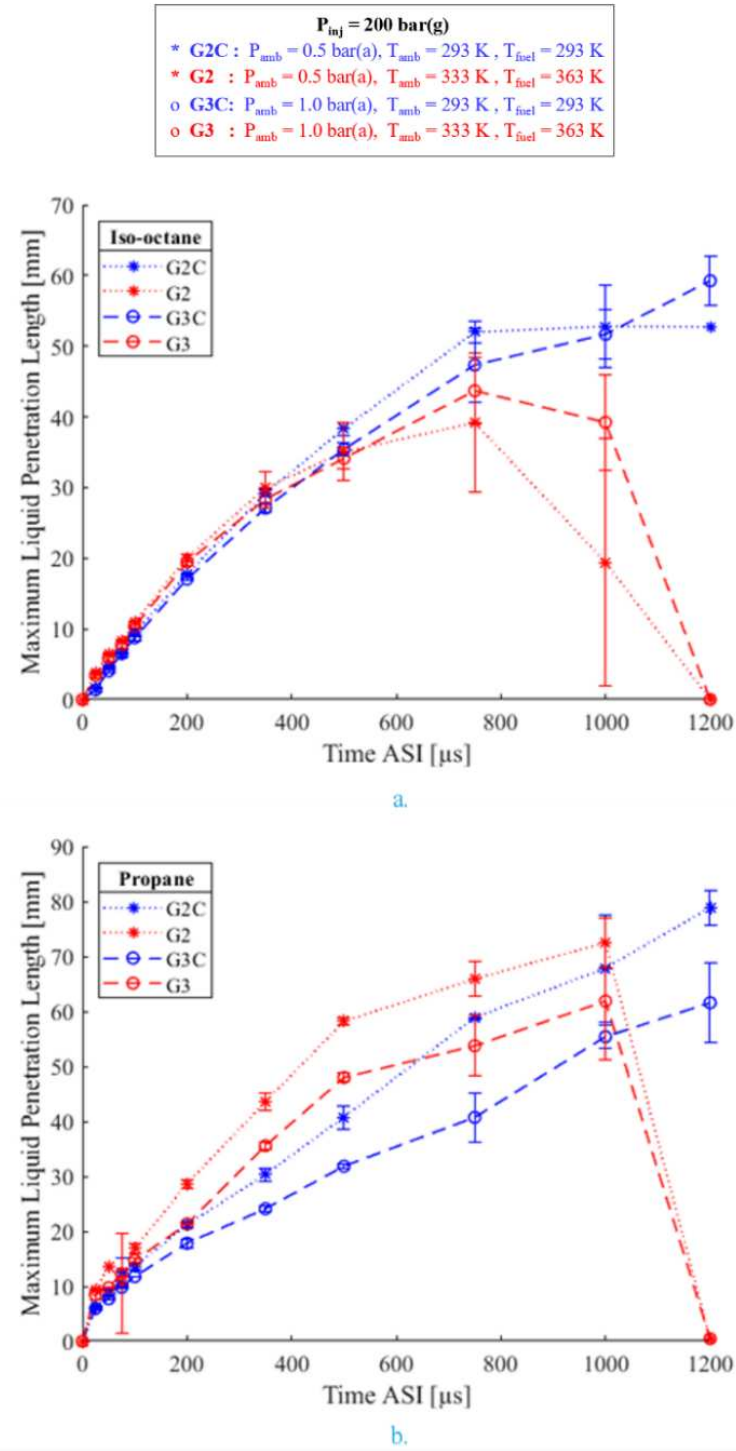


Figure 3.5: Maximum axial liquid penetration length measurements for a) iso-octane, and b) propane at corresponding conditions and timesteps measured using planar Mie Scattering imaging. Error bars are included at tested timestamps with a mean error in liquid penetration lengths of  $\pm 2.8 \text{ mm}$  for iso-octane,  $\pm 1.8 \text{ mm}$  for propane. A strong directly proportional relationship of the increased error and duration after start of injection was observed for both tested fuels.

For G3C conditions, liquid and vapor mostly overlap for the entirety of the spray propagation, however, the penetration length for the cold case is less than the hotter case, about 40 mm shorter at 1200  $\mu$ s. Unlike the overlap as seen in G3C, G3 shows a steep drop in liquid penetration after the end of injection, leading to vapor penetrating to 90 mm and no liquid at 1200  $\mu$ s.

As seen for both Schlieren and Mie imaging, crucial information from vapor and liquid penetration length, width, and speed measurements is used to define characteristics of the spray morphology. Iso-octane is minimally affected by temperature and pressure as seen in the qualitative and quantitative analysis from Schlieren and Mie imaging. It is also observed that most of iso-octane's spray propagation is contributed by its liquid cores, i.e., insignificant difference between liquid and vapor penetration lengths. This is largely due to the physical characteristics of iso-octane, namely, low volatility, high viscosity, and higher density than compared to that of propane. These properties help prolong the existence of the liquid phase of the fuel and produce a conventional spray pattern in iso-octane, i.e., wider spray angles and distinct plumes as observed in Figure 3.1a – f and Figure 3.4a - f, leading to a homogenous mixture both axially and transversely throughout the HPSC for all tested conditions. The observation of distinct plumes can be inferred to the absence of flash boiling effects in iso-octane, due to its low volatility, and high viscosity. A clear and consistent relationship between vapor and liquid penetration of iso-octane can also be observed by comparing Schlieren with planar Mie. Since iso-octane's spray does not experience severe flash boiling and collapse, the amount of liquid injected in the plane of the Mie laser sheet is only contributed by one plume of the 8-hole injector; therefore, decreasing the scattered laser intensity, and causing iso-octane to appear dimmer than propane in Mie images presented in Figure 3.4.

Unlike iso-octane, propane, due to its high volatility and low viscosity, experiences severe flash boiling at all tested conditions. This greatly impacts the spray morphology, structure, and mixing processes of the fuel. As seen in Schlieren imaging (Figure 3.1g – l), all of the eight individual plumes collapse into a singular jet due to its high super-heat degree.

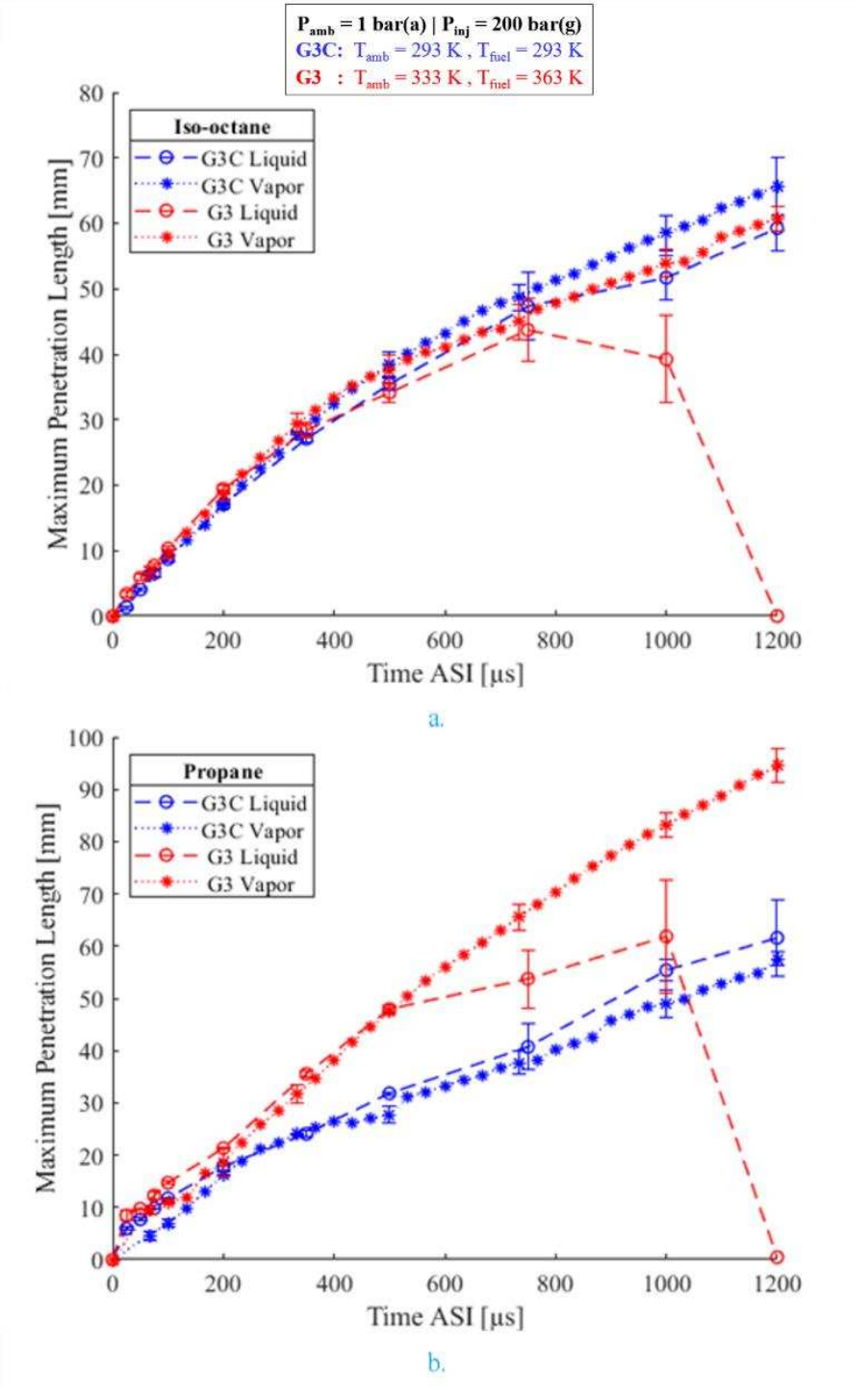


Figure 3.6: A comparison of maximum axial liquid vs. vapor penetration length for a) iso-octane, and b) propane at corresponding conditions and timesteps as a combined effort of high-speed Schlieren and planar Mie scattering imaging techniques. Error bars are included at suitable timestamps for improved legibility and comparison. The error ratios are same as observed in corresponding single phase experimental results.

Propane at colder conditions appears to have wider spray angles, minimal collapse, and some plume-to-plume distinction, whereas these features are completely absent at hotter conditions, signifying that the magnitude of super-heat degree of propane is strongly dependent on temperature. This also impacts the mixing processes of propane, as it transitions from semi-axially dependent mixing at colder conditions to strongly axially dependent mixing at hotter conditions. Another key feature to note about propane, contrary to iso-octane, is that at the tested conditions, the majority of propane's spray propagation is fed by its flash boiling, spray collapse, and high degree of vaporization. This also explains the direct proportionality of propane's penetration length with temperature. When comparing Mie images, propane's jet appears to be brighter compared to iso-octane's singular plume; this can be misleading as it might signify presence of more liquid in the cases of propane. However, it is worth noting that the collected Mie images in Figure 3.4 are for planar Mie, not global Mie, and unlike iso-octane where only one nozzle of the injector is contributing to the liquid concentration inside the laser plane, for propane, multiple nozzles collapse and contribute to its liquid concentration within the plane making it appear brighter. From Schlieren measurements in Figure 3.3c, it was also observed that propane's velocity pulsated after the first 100  $\mu$ s for all conditions, this effect was only seen in propane and can be attributed to the presence of shock structures within the fuel jet and gas-like injection of propane. All these unique features of propane and its variation from iso-octane's spray pattern, contribute to its classification as an unconventional spray.

### 3.1.3. Injection Rate Testing

#### 3.1.3.1. Current Profile Selection

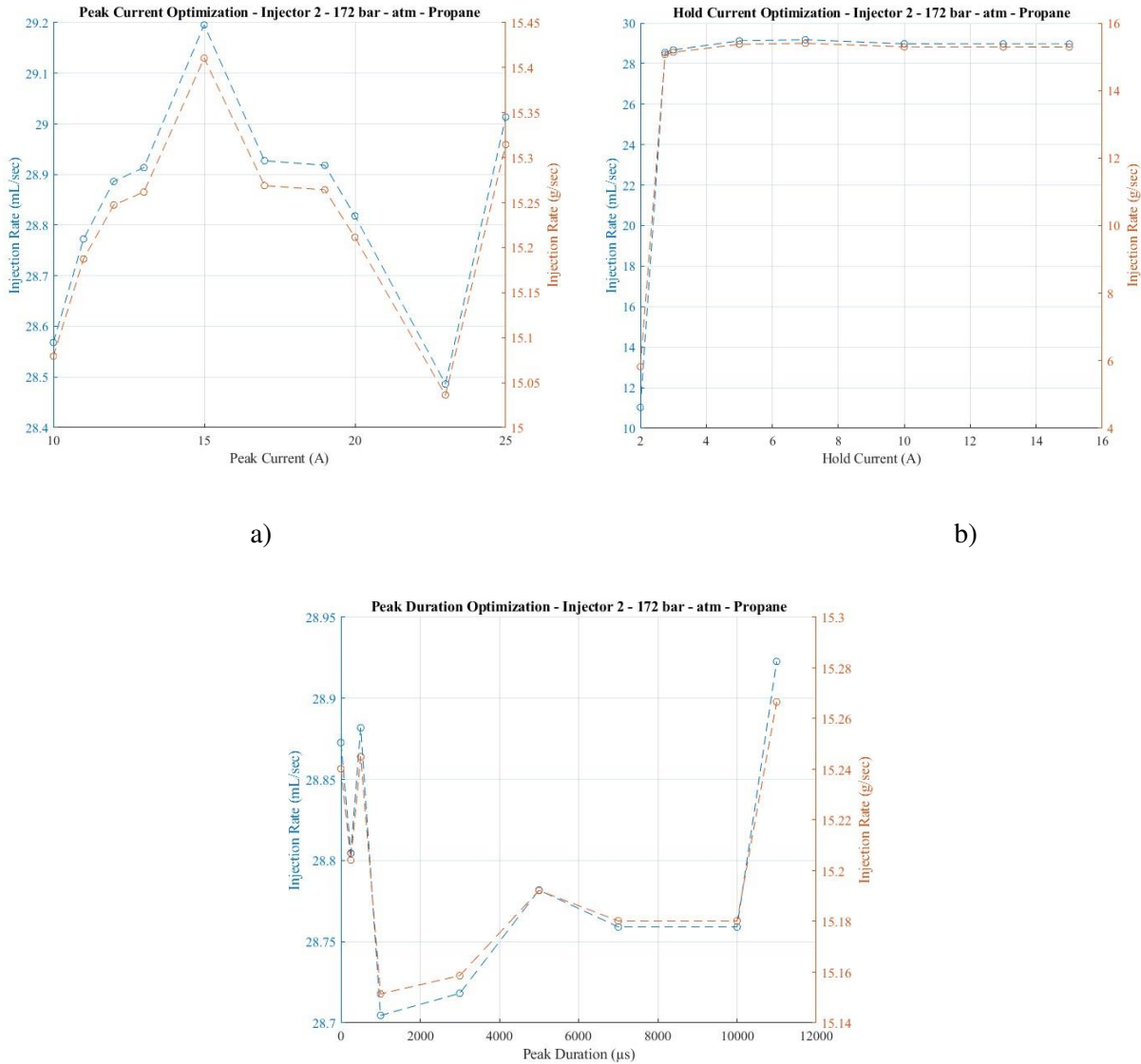


Figure 3.7: Injection rates of propane at various a) Peak current, b) Hold current, and c) Peak duration.

Figure 3.7 includes the injection rated measured at various current inputs. As seen in Figure 3.7a, the maximum flow rate was achieved at peak current of 15 A. Figure 3.7b shows that flow rates saturate for hold current greater than 3 A, with a maximum injection rate at 7 A. When these optimized peak and hold currents were used to measure the variability in the injection rate as a function of peak duration, as

seen in Figure 3.7c, the variability was minimal, hence the 500  $\mu$ s was considered as optimized peak duration.

Figure 3.8 highlights the significant effect of injection pressure on the injection rate for both propane (a), and iso-octane (b). For Delphi 5-hole #4, the maximum injection rate of 28.39 ml/sec for propane, and 23.77 ml/sec for iso-octane were achieved at the injection pressure for 350 bar.

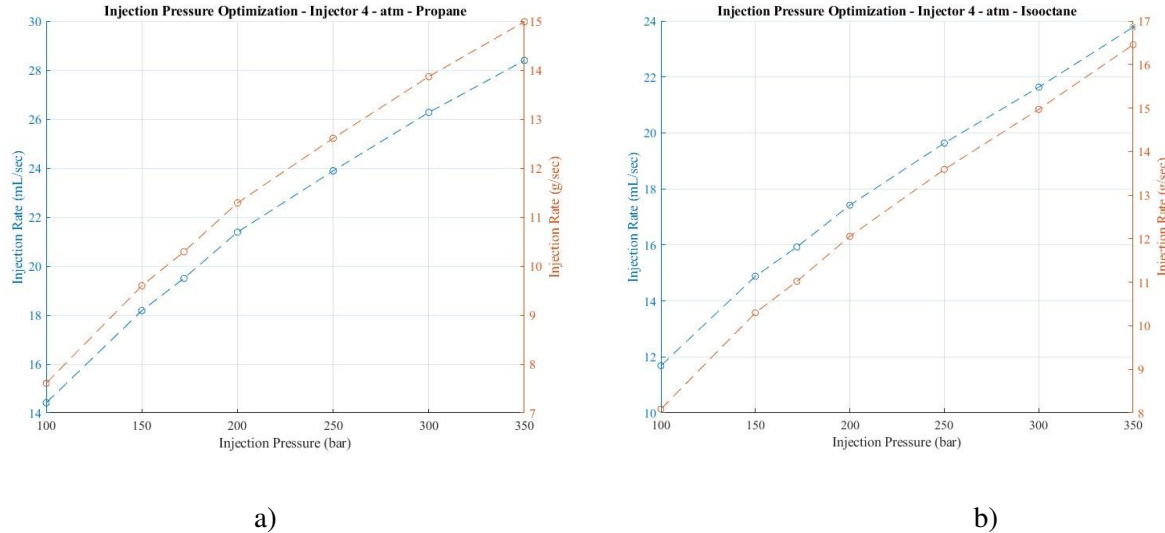
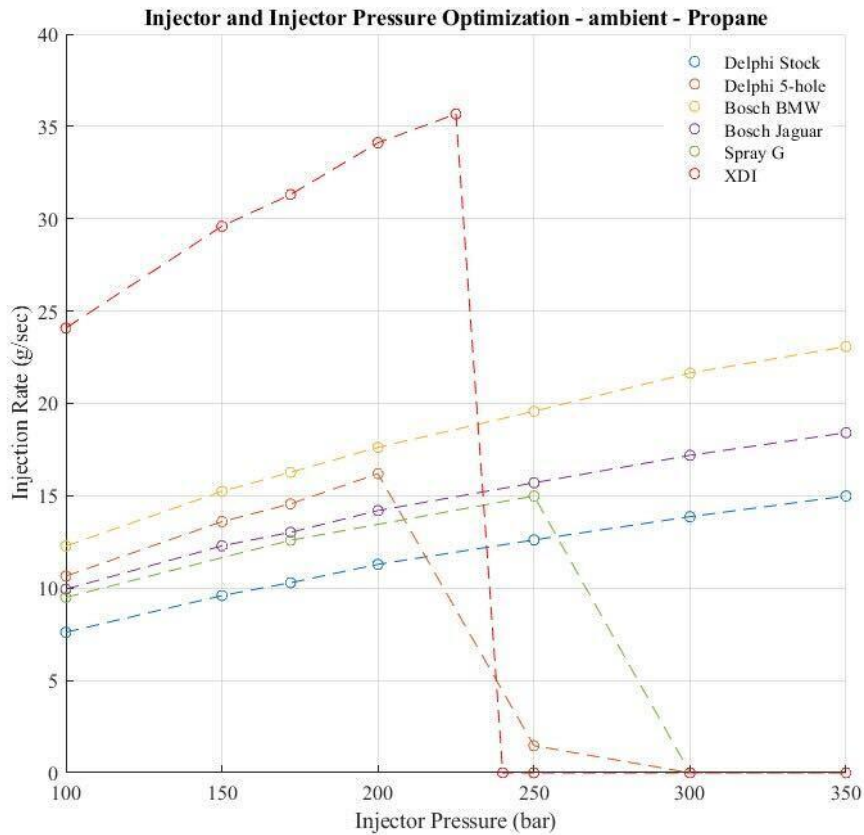


Figure 3.8: Injection rates at various injection pressures for a) propane and b) iso-octane.

### 3.1.4. Multi-Injector Testing

Four injectors including the Bosch BMW 325i EU5, Delphi 7-hole stock injector, ECN Spray-G injector, and modified 5-hole Delphi injectors have been tested at various engine-like conditions and high-speed schlieren and planar Mie imaging for propane and iso-octane fuels were carried out in the previous quarters. The data was processed and sent to Argonne National Lab for model tuning and validation.

Few other injectors: Bosch BMW 335 I injector, Bosch Jaguar Injector, and XDI +65 injector, were also tested along with the previously mentioned injectors and these injectors are shown in Figure 2.2. Injection testing was performed and a comparison of injection rate in grams per second are plotted in Figure 3.9.



*Figure 3.9: Injection rate as a function of Injection Pressure of Propane for various injectors at atmospheric conditions.*

As seen in the plot in Figure 3.9, XDI injector outperformed all the other injectors and was approximately had twice the injection rate compared to the second-best injector: Bosch BMW for pressures ranging from 100 to 240 bar. XDI injector, however, stops injecting for pressures higher than 240 bar. This maximum limit of injection is also seen for Delphi 5-hole injector, and Spray G injector where their injection rate drops after 200 bar and 250 bar, respectively. The best to worst performing injectors are: XDI, Bosch BMW, Delphi 5-hole, Bosch Jaguar, Spray G, and Delphi stock injectors. Further considerations are being made besides the injection rate for the selection of the injection to be used in the Cummins X-15 engine. These include adaptability to the engine head, and spray pattern.

### 3.1.4.1. Spray G

Schlieren images of iso-octane sprays and propane sprays at various chamber pressures (columns) ranging from 0.5 bar to 10 bar absolute are shown in Figure 3.10 and Figure 3.11, respectively. The top row contains spray for 20C for fuel and chamber temperatures and the bottom row for 90C for both at an injection pressure of 200 bar. For iso-octane, in Figure 3.10, it is observed that the spray collapse increases with pressure and temperatures. In contrast, spray collapse for propane, seen in Figure 3.11, decreases with chamber pressure but increases with chamber and fuel temperature.

The collapse results from plume-to-plume interaction between the individual jets for the 8-hole injector, which is more at low pressure and high temperatures as these jets expand more as they enter the chamber. Due to these interactions, the oblique/ or the transverse component of the jet gets canceled with that of another jet, leaving only the axial/ vertical part of the collapsed jet, which leads it to penetrate further downward in the chamber. Another critical feature observed in the collapsed jet is the darker central core indicating higher density (more liquid) due to the shielding effect. As chamber pressure is increased, these jets expand less and do not interact with each other, leading to a more traditional spray pattern.

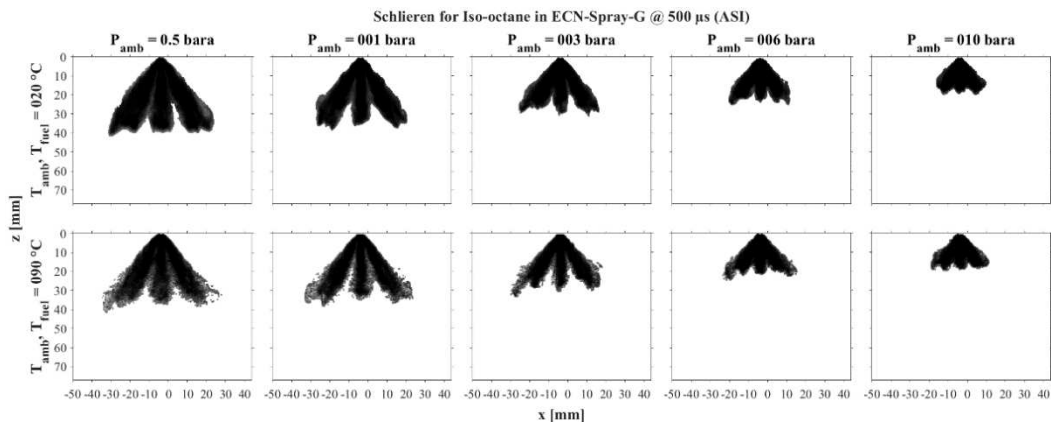


*Figure 3.10: High-speed Schlieren images for iso-octane at various denoted chamber pressures (columns) and fuel and chamber temperatures (rows) at  $500 \mu\text{s}$  after the start of injection for ECN Spray-G injector.*

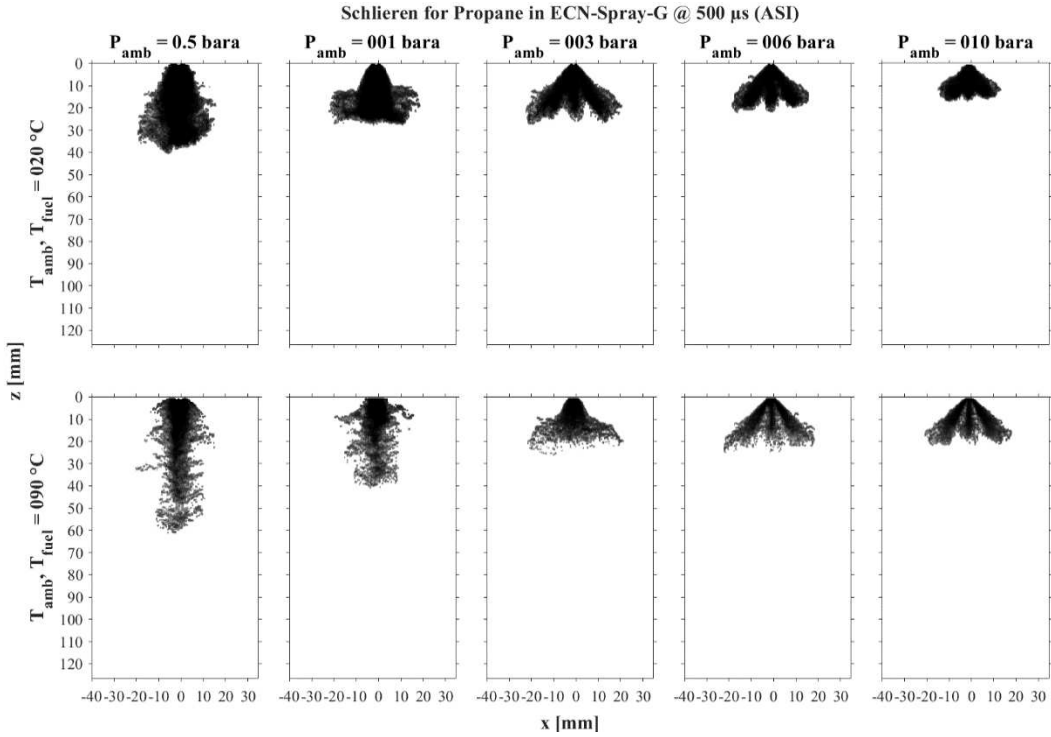


*Figure 3.11: High-speed Schlieren images for propane at various denoted chamber pressures (columns) and fuel and chamber temperatures (rows) at 500  $\mu$ seconds after the start of injection for ECN*

### 3.1.4.2. Delphi-5 hole

Schlieren images of iso-octane sprays and propane sprays at various chamber pressures (columns) ranging from 0.5 bar to 10 bar absolute are shown in Figure 3.12 and Figure 3.13, respectively. The top row contains spray for 20C for fuel and chamber temperatures, the middle row for 60C for both, and the bottom row for 90C for both at an injection pressure of 170 bar. For iso-octane, in Figure 3.12, it observed that the spray collapse increases with temperature and chamber pressure. In contrast, for propane, observed in Figure 3.13, spray collapse due to flash boiling increases with temperature while increasing chamber pressure shifts the collapse to plume-to-plume interactions.

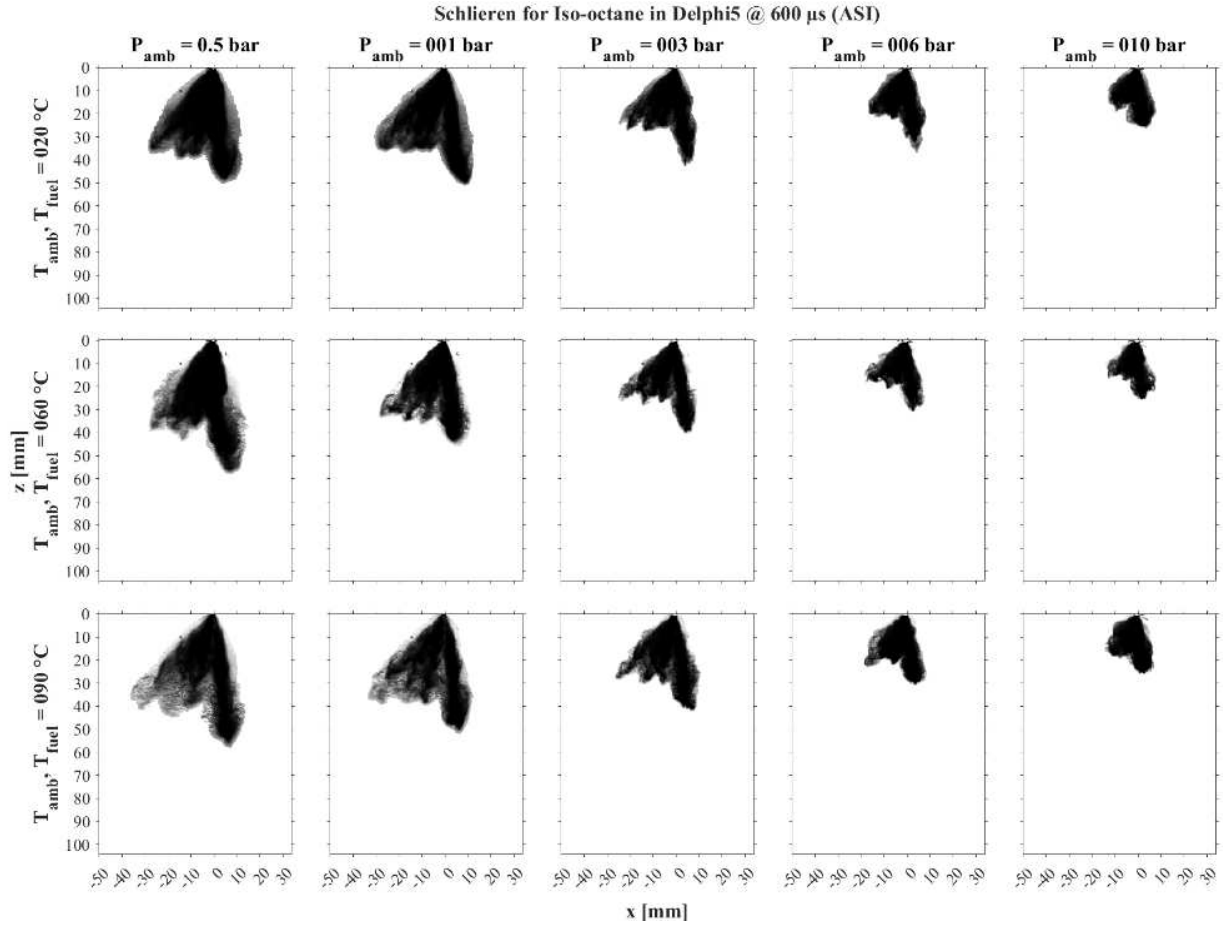


*Figure 3.12: High-speed Schlieren images for iso-octane at various denoted chamber pressures (columns) and fuel/chamber temperatures (rows) at 600  $\mu$ seconds after the start of injection for modified Delphi 5-hole injector.*

Spray collapse results from two phenomena: plume-to-plume interaction and flash boiling. The plume-to-plume interaction between individual jets can be seen as the combination of jets together, resulting in further penetration depths. In these interactions the transverse component of the jet is canceled with another jet leaving only the vertical component. The jets merge, resulting in greater momentum to penetrate deeper into the chamber. Another critical feature observed in the collapsed jet is the darker central core indicating higher density (more liquid) due to the shielding effect. The flash boiling collapse can be characterized by increased plume interaction and less defined plume boundaries. Similar to plume-to-plume collapse, flash boiling collapse also contributes to increase penetration depth and liquid depth.

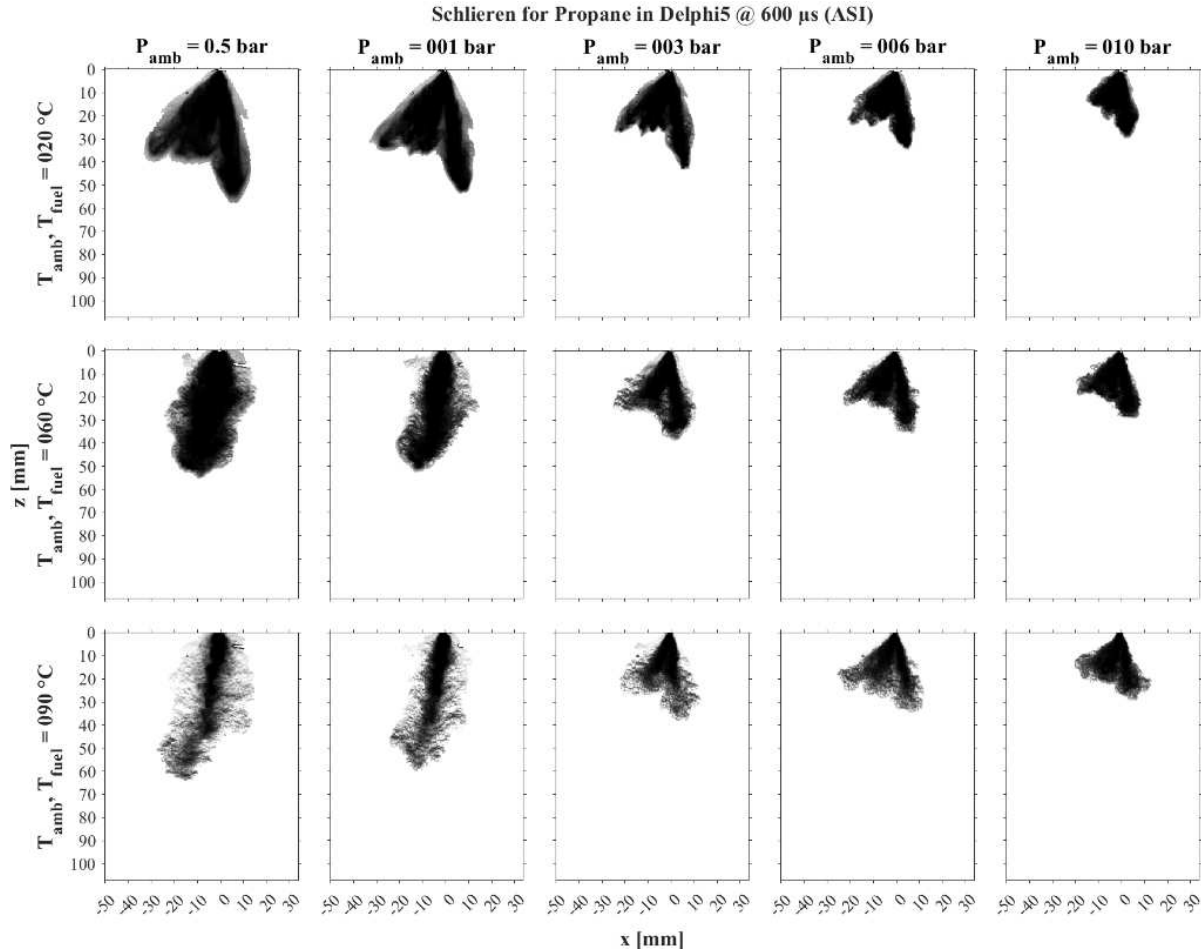


*Figure 3.13: High-speed Schlieren images for propane at various denoted chamber pressures (columns) and fuel and chamber temperatures (rows) at 600 microseconds after the start of injection for modified Delphi 5-hole injector.*

Schlieren gives a good visualization of the global spray dynamics. Spray development of propane is sensitive to chamber pressures and fuel and chamber temperatures. The liquid-vapor boundary is unclear in Schlieren. Schlieren is a 2D projection of a 3D phenomenon that makes it difficult to parse out individual plume behavior to develop high-fidelity spray models. Hence, a sophisticated imaging technique like the plane Mie scattering imaging is needed to define the difference within these structures.

The planar Mie scattering imaging setup was modified to capture images of liquid spray at smaller time increments of 33 microseconds for the entire injection duration (previously collected at only three time stamps). These recorded images correspond with the timestamps recorded in high-speed Schlieren imaging; hence good comparison in the vapor and liquid phase can be made when the images from both these imaging

techniques are overlapped. Mie data for the modified Delphi 5-hole injector was collected and is currently being processed in a more comprehensive manner.

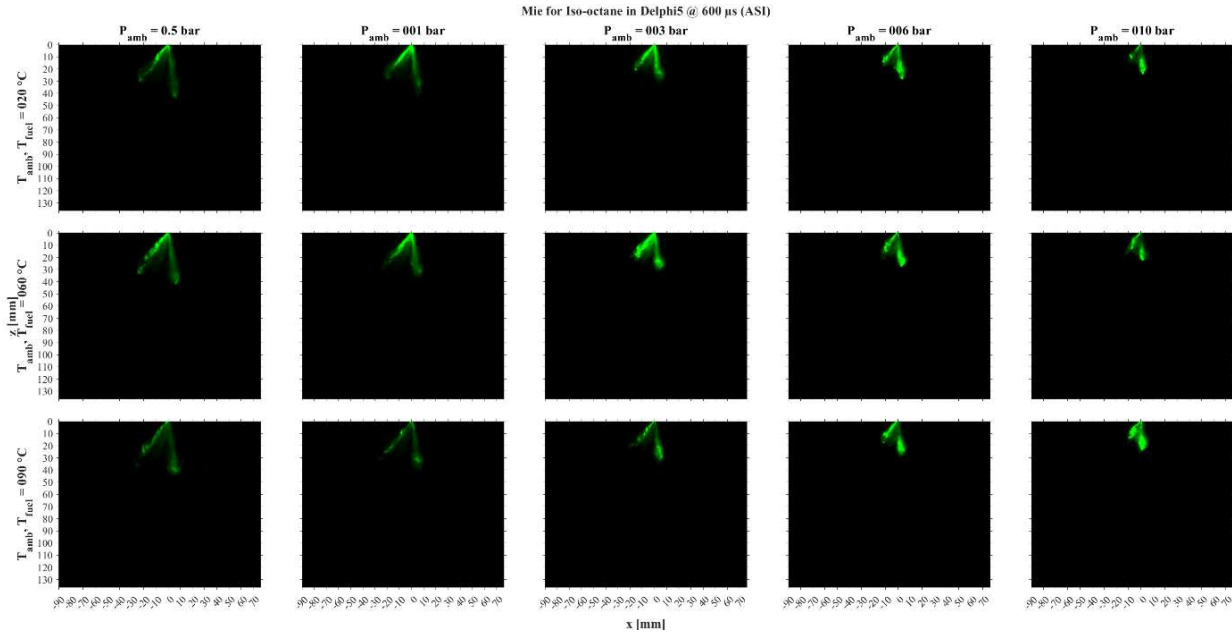


*Figure 3.14: Planar Mie images for iso-octane at various denoted chamber pressures (columns) and fuel and chamber pressures at 600  $\mu$ seconds after the start of injection for modified Delphi 5-hole injector*

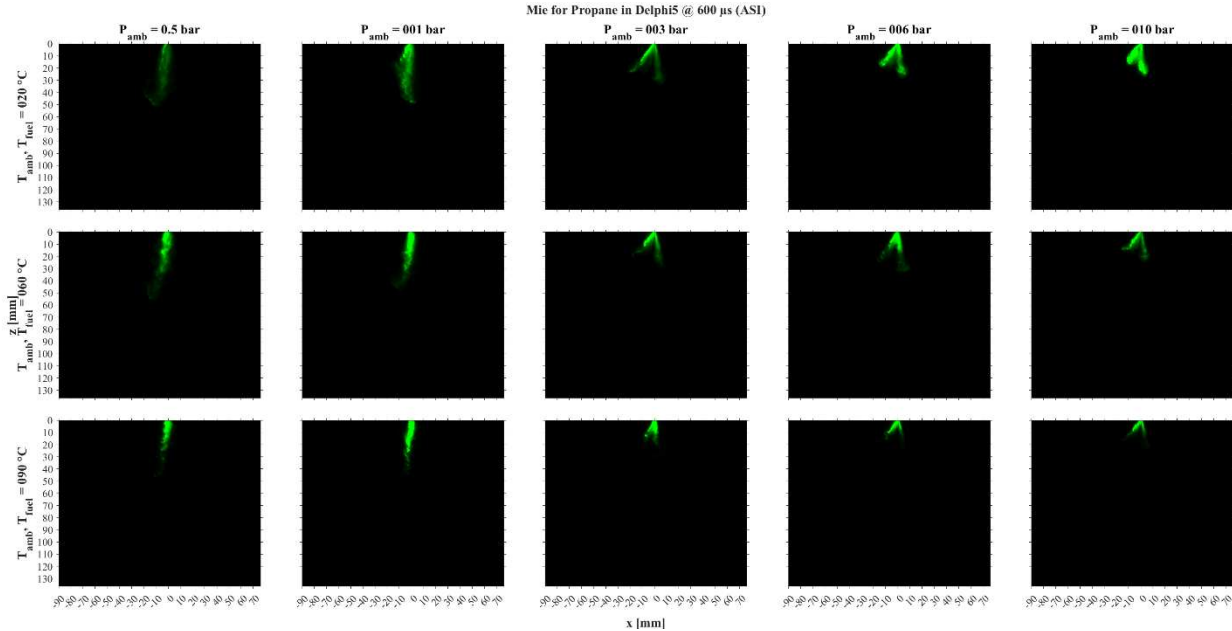


*Figure 3.15: Planar Mie images for propane at various denoted chamber pressures (columns) and fuel and chamber pressures at 600  $\mu$ seconds after the start of injection for modified Delphi 5-hole injector*

Mie images of iso-octane and propane sprays at various chamber pressures from 0.5 bar to 10 bar absolute are shown in Figure 3.14 and Figure 3.15, respectively. For iso-octane, observed in Figure 3.14, greater liquid concentrations are maintained throughout the spray duration for higher temperatures and pressures. Inversely, propane spray, shown in Figure 3.15, liquid concentrations permeated longer for higher temperatures and lower pressures.

The increased duration of liquid present in the spray is associated with the dominating collapse phenomenon. For iso-octane, the plume-to-plume interaction at higher temperatures and pressures leads to larger concentration gradients in the center of the collapsed jets. Due to the geometry of the injector, three spaced holes and two clumped holes, there are two distinct regions of liquid that form. Propane behaves oppositely, as the flash boiling is present under different conditions. The shielding of the flash boiling at lower pressures and high temperatures protects liquid regions throughout the injection duration. A comparison for both schlieren and planar Mie images are presented in Figure 3.17 that highlights the spray collapse phenomenon.

These recorded images correspond with the timestamps recorded in high-speed schlieren imaging; hence good comparison in the vapor and liquid phase can be made when the images from both these imaging techniques are overlapped. Due to the geometry of the 5-hole injector, three spaced holes and two clumped holes, there are two distinct regions of liquid that form. The propane behavior is opposite of iso-octane, as the flash boiling is present under different conditions. The shielding of the flash boiling at lower pressures and high temperatures protects liquid regions throughout the injection duration.

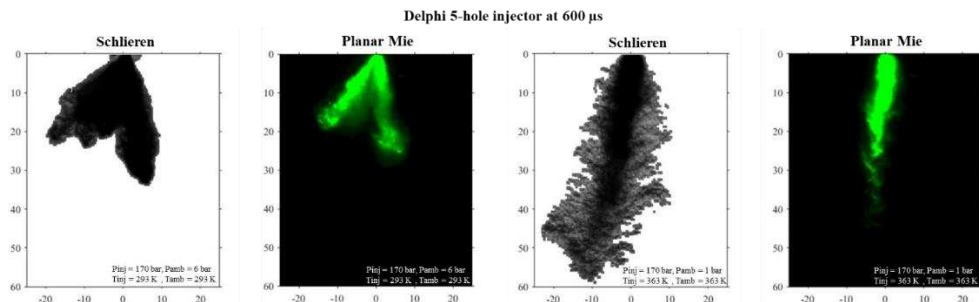


*Figure 3.16: Schlieren and Mie comparisons of propane for Delphi 5-hole injector.*

### **3.2. Numerical Spray Simulation Results**

Within this section, the outcomes outlined are a joint contribution from Dr. Lorenzo Nocivelli and Dr. Katherine J Asztalos at Argonne National Lab. The aim is to elucidate the pragmatic application of experimental discoveries in validating and enhancing spray models. The presented results encompass iterative tuning strategies and a comparative analysis with experimental outcomes. The collaborative research at Argonne National Lab, closely conducted with the author, is further expounded in Windell et al. [100]. The first step of the simulation campaign is to simulate nozzle flow to provide quasi-steady mass flow rate values that are to be imported in the initialization of the Lagrangian spray. Previous results [109] for iso-octane operated at  $P_{\text{inj}} = 200$  bar and  $T_{\text{fuel}} = 363$  K are compared with the values obtained in the G3C and G3 conditions, to scale the injection rate of the spray. Figure 3.17 shows the comparison between the different quasi-steady mass flow rates, which result 12.0% and 13.4% lower than iso-octane, for propane at G3C and G3 conditions, respectively. Moreover, the results from the nozzle flow simulation are used to guide the selection of the propane spray plumes entering the chamber, in terms of plume angle, which results in significantly higher values than experienced by GDI spray. In presence of an under-expanded jet, the rigorous calculation of a spray cone-angle in the near nozzle region is not trivial. The selection of the input for the Lagrangian spray parcels is therefore based on a sensitivity study on cone angles ranging from the standard gasoline reported by Payri [96] to  $40^\circ$ , which can reproduce the sudden expansion of the jet, clearly shown by the mixture density profile in Figure 3.18. Due to the higher temperature of the fuel, G3 conditions show a higher initial expansion, observed in Figure 3.18b, which is driven by the higher superheat degree of the fuel entering the chamber. This information is kept consistent in the setup of the Lagrangian spray.

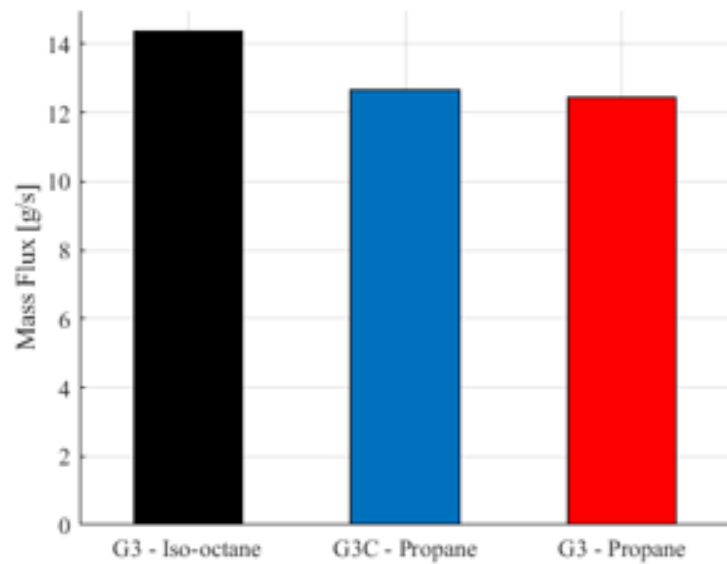


Figure 3.17: Comparison of the mass flow rate at quasi-steady needle lift operation for iso-octane at G3 (black) injection conditions, G3C (blue), and G3C (red) for propane.

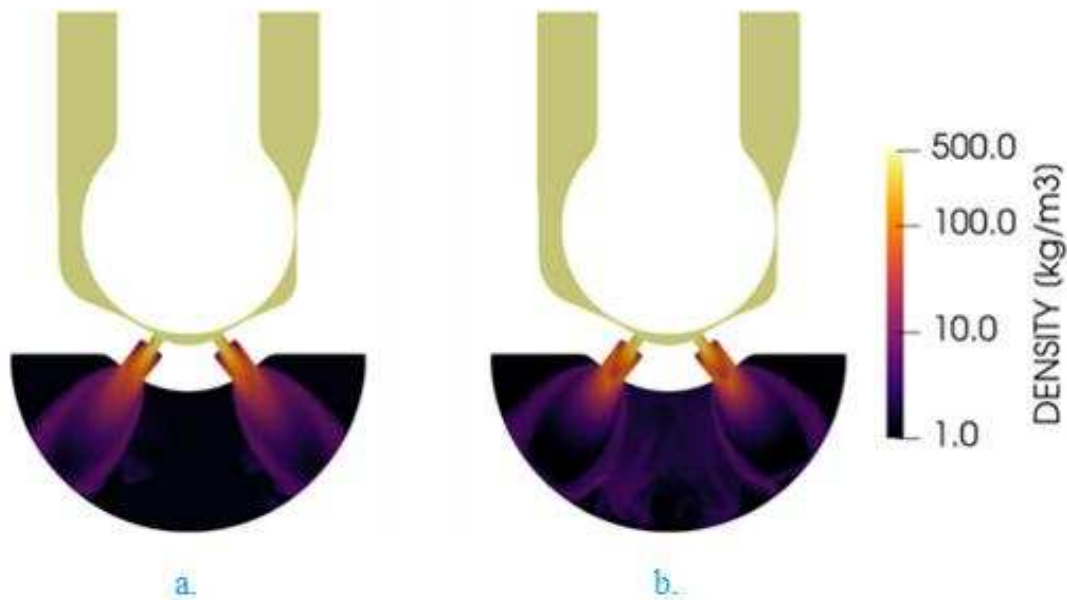


Figure 3.18: Mixture density profiles at quasi-steady injection condition for the injection of propane at (a) G3C, and (b) G3 conditions.

### **3.2.1. Lagrangian Spray Simulation Results**

#### *3.2.1.1. Spray G*

The Lagrangian spray simulations in this work present preliminary results from an effort to define a computational framework capable of reproducing the behavior of propane sprays for engine-like conditions. The focus of this simulation campaign is to capture fuel development in the HPSC, which will be validated against optimal experimental measurements. Three conditions have been simulated: (i) G3 with iso-octane, (ii) G3C with propane, and (iii) G3 with propane. As stated in the section describing the numerical simulation processing methods, the results are qualitatively compared with experimental results from the HPSC obtained through Schlieren and Mie scattering imaging techniques. The numerical results are compared with the experimental data in terms of spray morphology and axial penetration. The setup for the injection of iso-octane at G3 conditions is based on the work by Nocivelli et al. [33] and re-processed to replicate Schlieren and Mie scattering images. The injection of propane at G3C and G3 conditions implement the same flow rate profile, which is scaled on the simulated mass flows obtained from the nozzle-flow simulations as shown in Figure 3.17.

Preliminary studies on the mesh resolution reported that a minimum cell size of 0.2 mm, obtained through adaptive mesh refinement, was able to generate results comparable to the experiments with CPU-times compatible to engine simulations. The representation of the vaporization-driven collapse of the plumes is achieved by enlarging the initial cone angle ( $C_A$ ) of the blob injector to  $40^\circ$  and keeping the inclusion angle ( $I_A$ ) consistent with the nominal direction of the nozzles equal to  $37^\circ$ ; with the cone angle controlling the angle of the spread of the injectant and the inclusion angle being defined as the deviation from the injector axis for a single nozzle. Both of these variables produce an effect on the axial penetration and the morphology of the spray, as well as potentially influencing the spray breakup and atomization for different conditions.

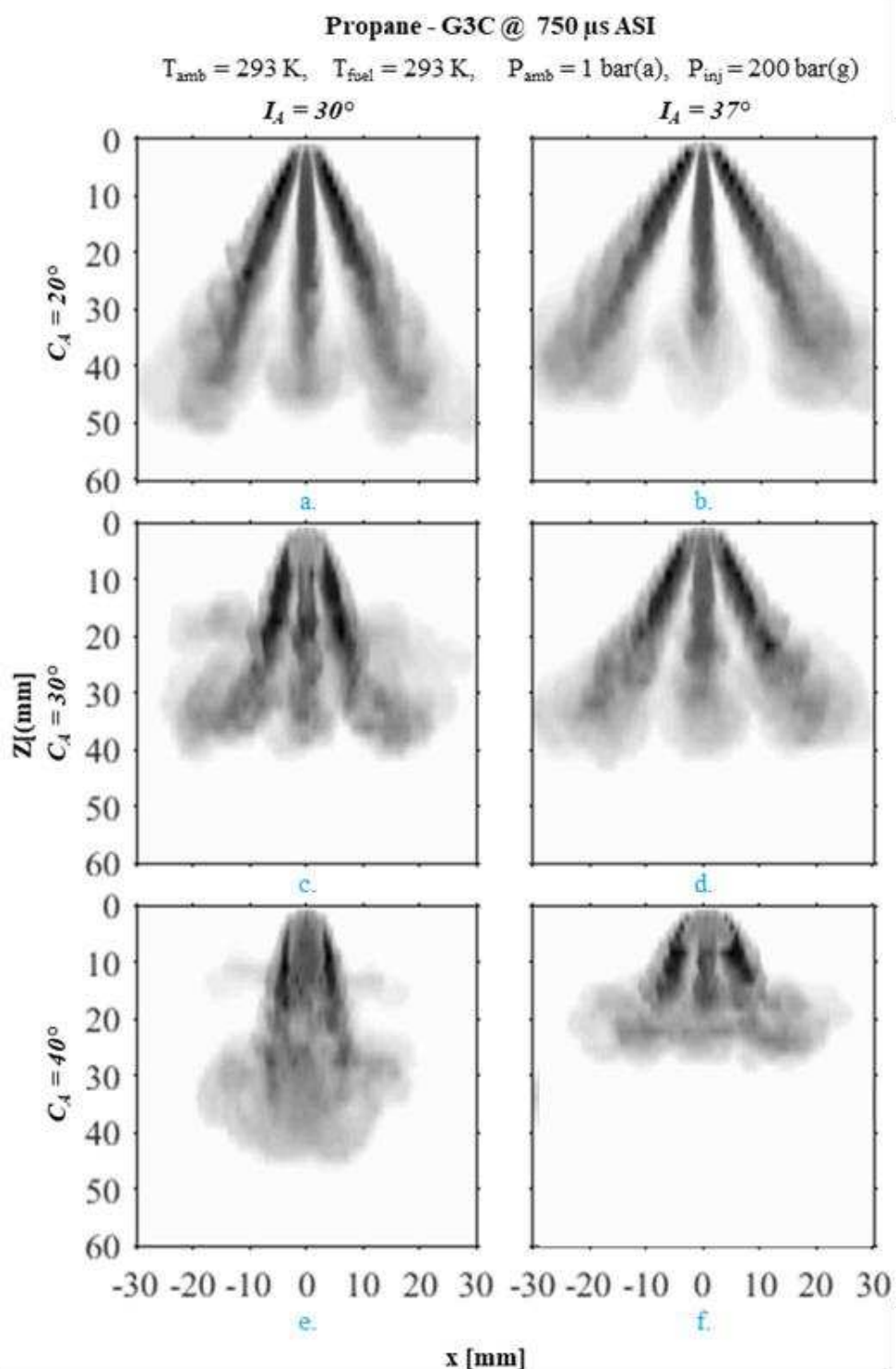


*Figure 3.19: Projected density gradient of the gas phase from Lagrangian spray simulations (simulated Schlieren) of injection of propane at G3C conditions modeled for variations in cone angle  $C_A$  (down) and inclusion angle  $I_A$  (across). Final geometry modeling decisions made for G3C conditions shown in (f).*

The simulation results for propane were found to be sensitive to both the  $I_A$  and the nominal direction of the nozzles; to illustrate this sensitivity, spray morphology comparisons are shown for a range of  $C_A$ , as well as  $I_A$ , for both G3C and G3 conditions in Figure 3.19 and Figure 3.20, respectively. Numerical results are shown in Figure 3.19 - Figure 3.22 at 750  $\mu\text{s}$  ASI, as this timestep corresponds to maximum axial penetration and is the time at which differences between setups are most apparent. Additional timesteps were also compared with experimental results, and each simulation was performed from 0 to 1200  $\mu\text{s}$  ASI.

The results in Figure 3.19 and Figure 3.20 illustrate the influence of  $C_A$  and  $I_A$  on the spray morphology; namely, spray collapse is promoted as  $C_A$  is increased. This can be seen clearly at the lower  $I_A$  shown in Figure 3.19e and Figure 3.20e. Whereas the effect of a higher  $I_A$  is seen as dissipation in the initial axial momentum component, thus reducing the maximum axial penetration, as observed in Figure 3.19f and Figure 3.20f. The noticeable differences in spray morphology can be addressed by further examining the breakup model. Comparing the simulations results with experimental Schlieren vapor penetration lengths and widths,  $I_A$  of  $37^\circ$  and  $C_A$  of  $40^\circ$  were found to model the penetration profile accurately for injection of propane at both G3C and G3 conditions. The final geometry modeling decisions made for the blob injector at G3C and G3 conditions are shown in Figure 3.19f and Figure 3.20f, respectively.

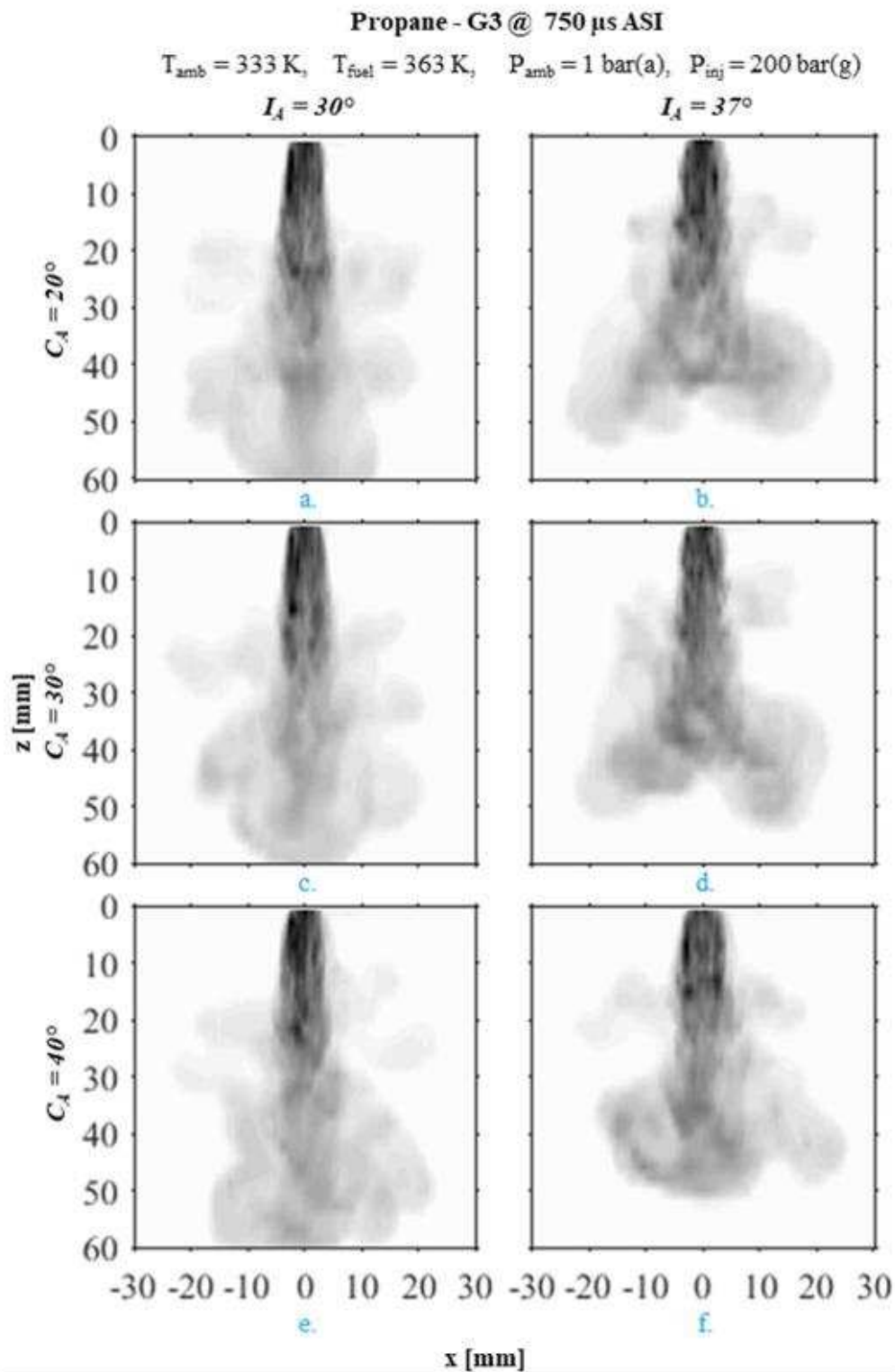


Figure 3.20: Projected density gradient of the gas phase from Lagrangian spray simulations (simulated Schlieren) of injection of propane at G3 conditions modeled for variations in cone angle  $C_A$  (down) and inclusion angle  $I_A$  (across). Final geometry modeling decisions made for G3 conditions shown in (f).

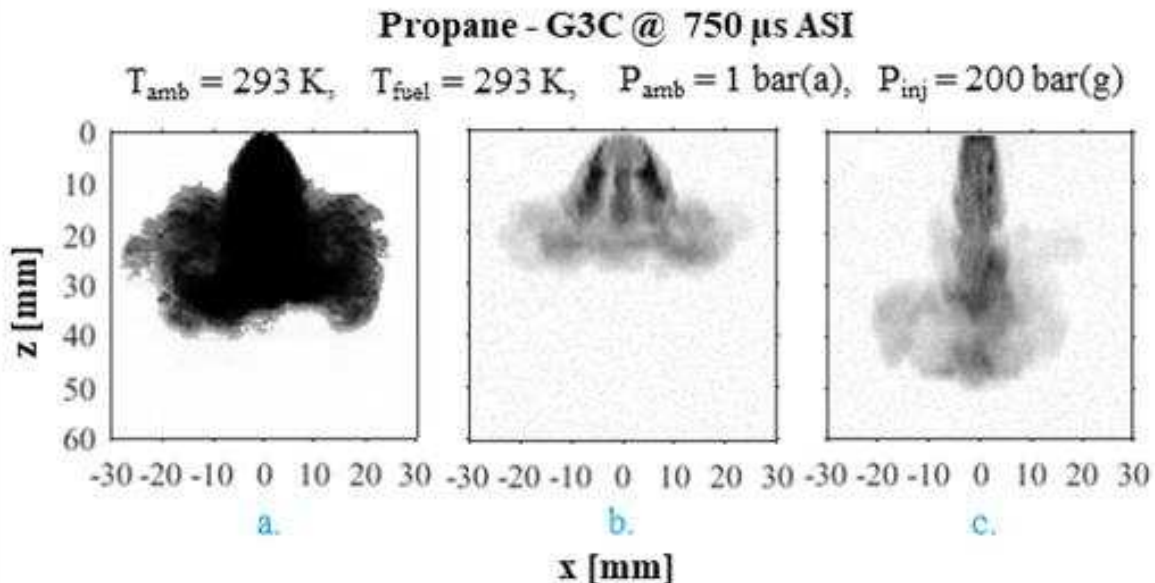


Figure 3.21: (a) Experimental Schlieren image of propane at G3C; projected density gradient of the gas phase from Lagrangian spray simulations (simulated Schlieren) of injection of propane at G3C conditions modeled with Rayleigh-Taylor breakup time and model size constants corresponding to (b) non-extreme flashing conditions, and (c) extreme flashing conditions. Final modeling decisions made for G3C conditions shown in (b).

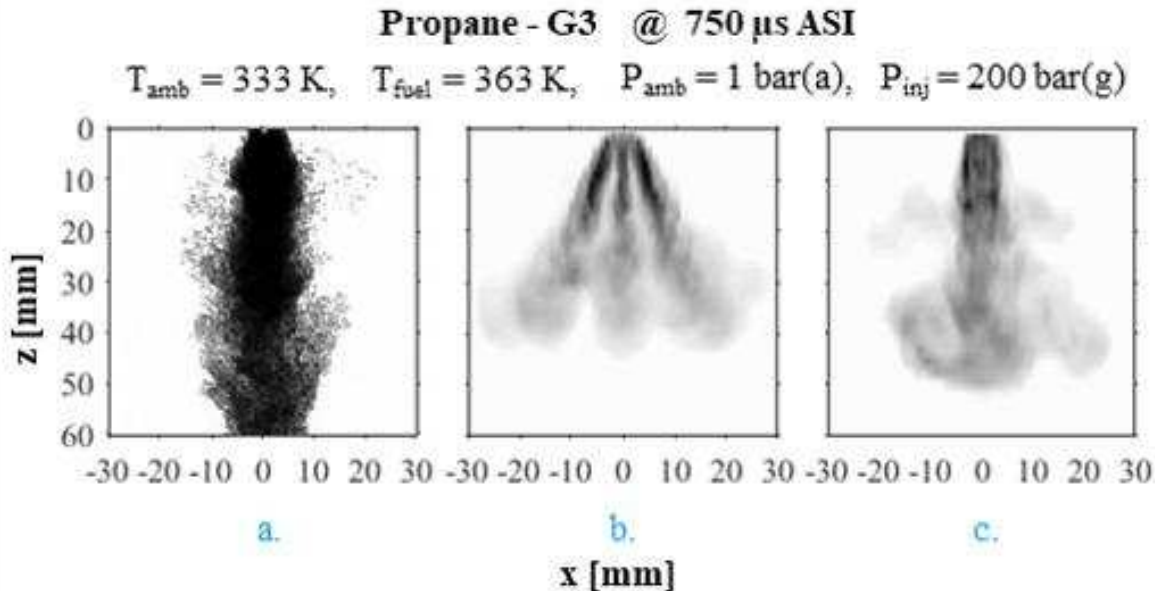
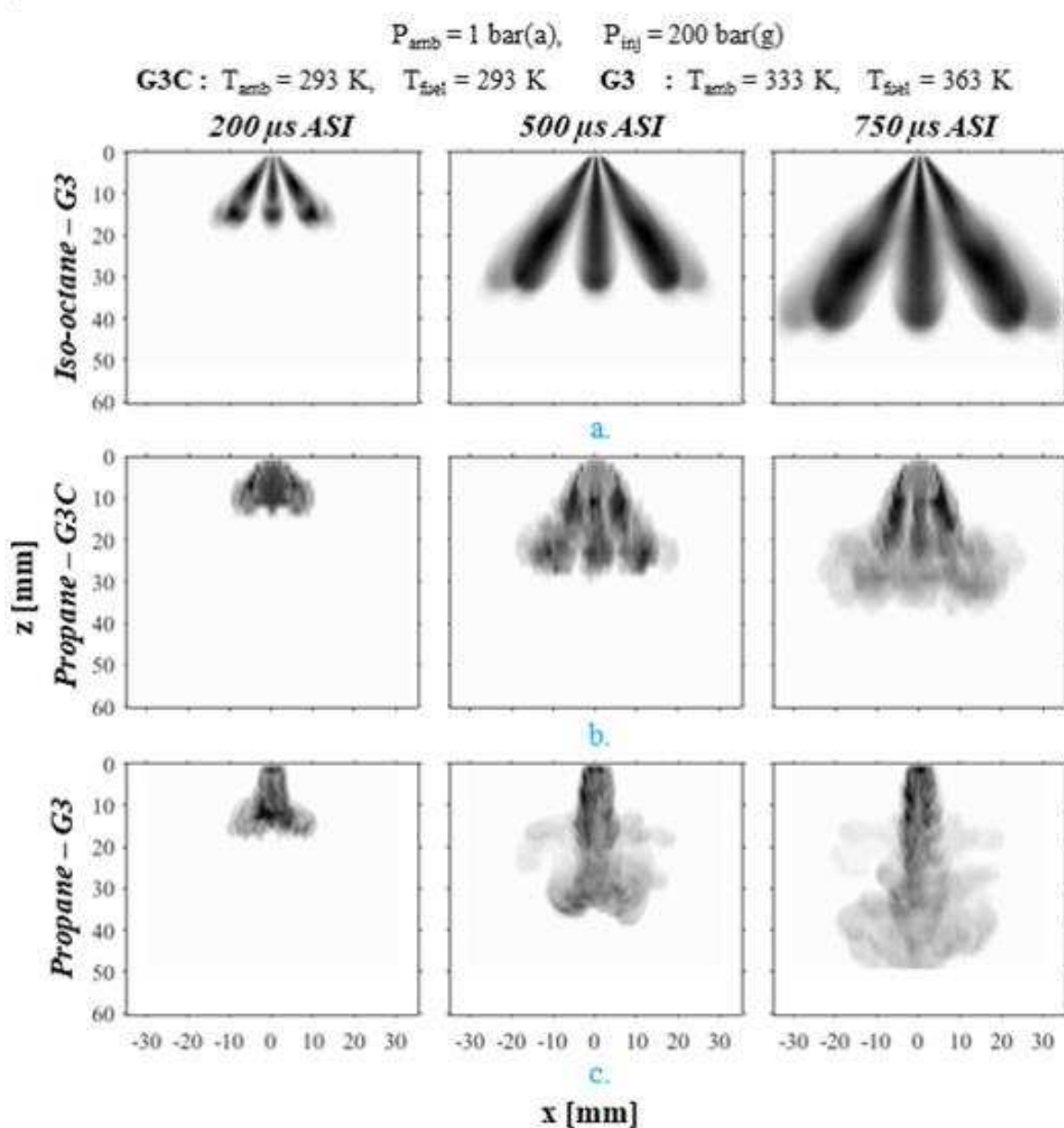


Figure 3.22: a) Experimental Schlieren image of propane at G3; projected density gradient of the gas phase from Lagrangian spray simulations (simulated Schlieren) of injection of propane at G3 conditions modeled with Rayleigh-Taylor breakup time and model size constants corresponding to (b) non-extreme flashing conditions, and (c) extreme flashing conditions. Final modeling decisions made for G3 conditions shown in (c).

Improvements can be made in capturing the spray morphology by considering the KH model breakup time and model size constant for the Rayleigh-Taylor (RT) model [114]. Extreme flashing conditions are simulated by decreasing the model breakup time constant from 1.0 (corresponding to non-extreme flashing conditions) to 0.1, and by decreasing the model size constant from 0.6 (corresponding to non-extreme flashing conditions) to 0.25. In particular, two conditions were simulated: (i) parameters corresponding to conditions without extreme flashing, and (ii) with extreme flashing. Results for propane injection at G3C conditions can be seen in Figure 3.21, with results for propane injection at G3 conditions shown in Figure 3.22. It was observed that at G3 conditions, accounting for extreme flashing improved the spray morphology in terms of comparison with experimental results seen in Figure 3.22a. It was found that at G3C conditions, improvement in terms of comparable morphology of the Lagrangian spray with experimental results was achieved for parameters corresponding to non-extreme flashing conditions, most notably in the spray collapse and in the maximum spray penetration. For the different conditions simulated, the chosen setup is given by Figure 3.21b for G3C, and Figure 3.22c for G3. The differences in modeling parameters are due to the different spray morphologies observed for the two conditions simulated. The model breakup effect is quite strong for higher temperatures; for G3 conditions it is necessary to account for rapid vaporization of small droplets, and modeling parameters corresponding to extreme flashing, to capture these effects. For lower temperature conditions, i.e., G3C, the vaporization rate is lower and does not drive morphology as severely, and the model breakup effect is less dominant.

The projected gradient of the gaseous phase density in the Eulerian domain, which includes both fuel vapor and ambient N<sub>2</sub>, is reported in Figure 3.23 for the three different conditions at 200 µs ASI, 500 µs ASI and 750 µs ASI. The results highlight that the Lagrangian simulation can capture the fuel effect for the tested conditions. Propane shows strong plume-to-plume interaction and complete collapse of the spray around the injector axis for both G3C and G3. The higher penetration measured in G3 conditions is reproduced by the simulations. This behavior is directly correlated to the temperature of the fuel and its consequent vaporization propensity. When injected at ambient temperature – both for fuel and ambient, at G3C conditions – the vaporization rate of the fuel decreases due to the lower vapor pressure and the reduced

thermal energy available in the chamber. The collapse is less abrupt, and the axial velocity of the resulting vapor jet is lower, generating a wider and shorter spray evolution.



*Figure 3.23: Projected density gradient of the gas phase from Lagrangian spray simulations (simulated Schlieren) of injection of (a) iso-octane at G3, (b) propane at G3C, and (c) propane at G3 condition at denoted timestamps.*

Quantitatively, the results capture the fuel effect, but the vapor penetration shown in Figure 3.24, calculated from the maximum axial distance from the injector location where the normalized gradient is higher 0.02 with binarized images, is under predicted for propane injection at G3C and G3 conditions (Figure 3.24b). This discrepancy is ascribed to the lack of a dedicated flash-boiling model for the parcels and to the simplified injector model used for the propane injection. The blob injector model in fact assumes only liquid injection, with droplet sizes defined as a function of the nozzle diameter and of a discharge coefficient. These assumptions are not valid for an extremely volatile fuel like liquid propane at the tested conditions.

This lack of accuracy in the simulation is visible in the comparison with the Mie scattering results which highlight that the phase-change trend is not consistent with the experiments as shown in Figure 3.25. It is possible to notice that at a low-vaporization condition – iso-octane at G3 conditions – the penetration of the liquid parcels is strongly correlated with the density gradients in the gas phase reported in Figure 3.23. For propane, and especially for the most superheated conditions – G3 – the vaporization is almost instantaneous and differs from the collapse spray core seen experimentally. These results underline the lack of accuracy of the Lagrangian spray models in representing extremely vaporizing sprays.

The current work represents a first assessment of the capability of the commonly available models for engine-spray simulations and highlight the fact that, despite the reasonable agreement obtained in the fuel vapor morphology, the representation of the liquid phase lacks accuracy. The addition of the flash-boiling vaporization terms on the phase-change modeling further reduces the liquid penetration without improving the representation of the vapor dynamics. For propane, both G3C and G3 conditions, are extreme flashing conditions: the super heat degree, defined in Equation (1.2), is respectively 0.12 and 0.03, and the empirical correlation tends to over-estimate the phase-change.

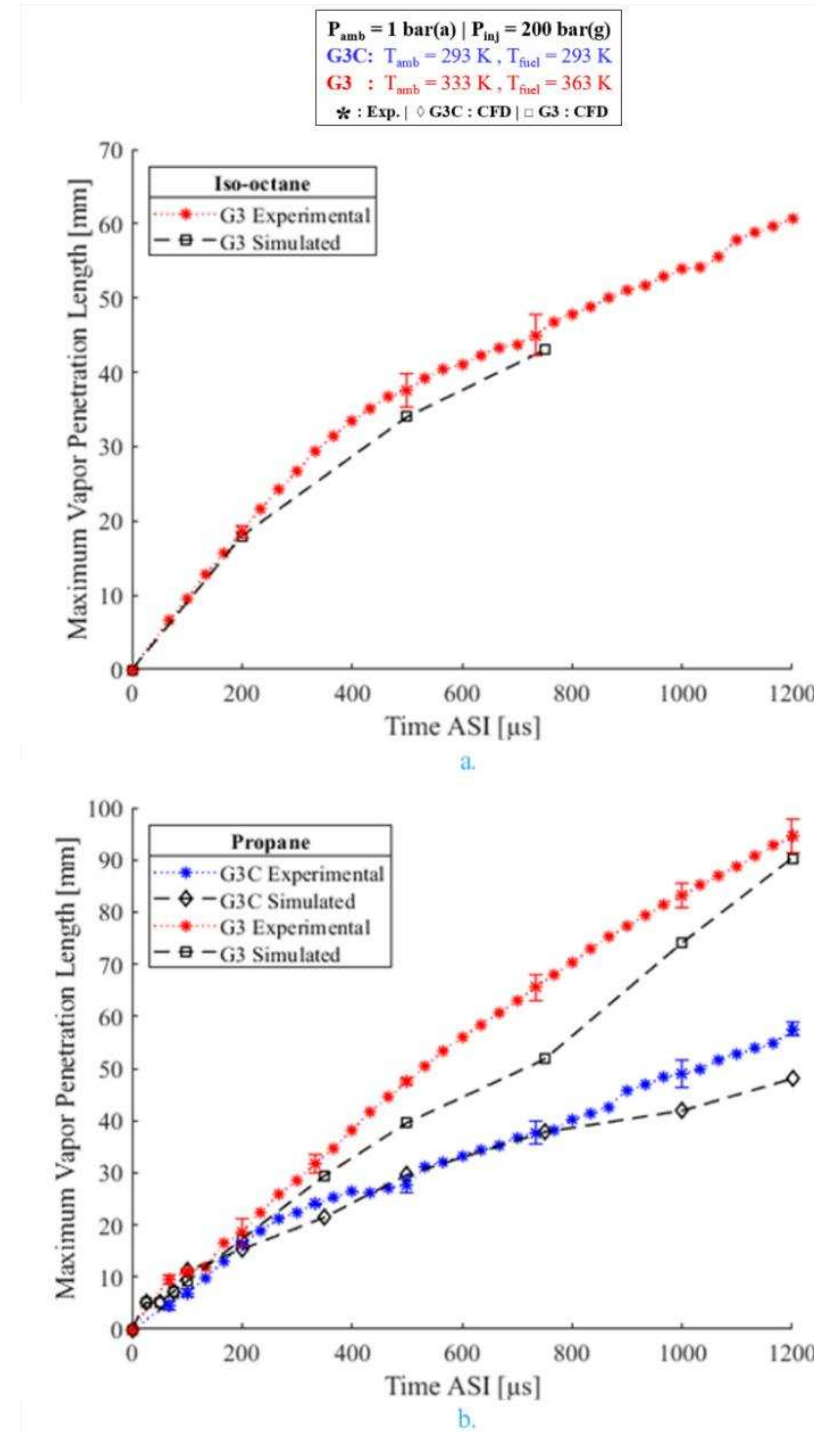


*Figure 3.24: Comparison between the experimental results of maximum axial vapor penetration of the spray from high-speed Schlieren imaging and computational results from projected density gradient of gas phase from Lagrangian spray simulations (simulated Schlieren) of (a) iso-octane at G3, and (b) propane at G3C and G3 conditions. Error bars are included at suitable timestamps in the experimental measurements for improved legibility and comparison. The error ratios are same as observed in corresponding single phase experimental results.*

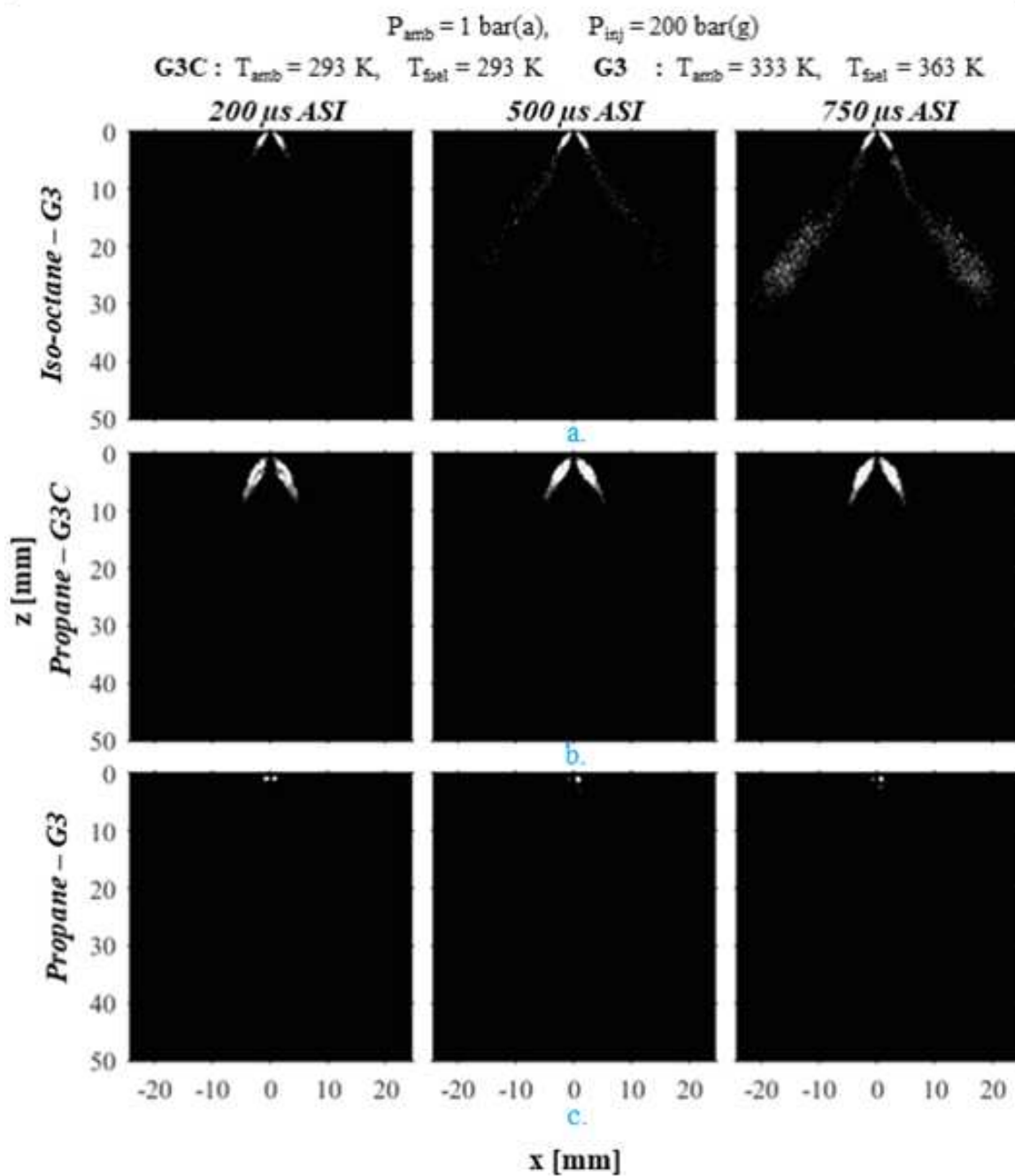


Figure 3.25: Projected density gradient over the line-of-sight of the liquid phase from Lagrangian spray simulations for the volume of the laser sheet (simulated planar Mie) of injection of (a) iso-octane at G3, (b) propane at G3C, and (c) propane at G3 conditions at denoted timestamps.

### 3.2.1.2. Delphi 5 hole

A two-tier approach based on three-dimensional (3-D) computational fluid dynamic (CFD) simulation has been defined to design a numerical model for LPG injection for engine-like domain and conditions using the commercial CFD software CONVERGE (v3.0). First, high-fidelity simulations of the injector nozzle-flow are carried out to determine the spray characteristics entering the chamber. Then, the obtained thermo-kinematic properties – e.g., jet momentum and angle – of the spray is introduced into the Lagrangian-Eulerian framework, which is a well-established approach for automotive sprays. The simulation effort focused on two GDI multi-hole injectors, the research-grade 8-hole Spray-G from the Engine Combustion Network (ECN) and the optimized 5-hole injector developed within this project, manufactured by C Zero. For further details regarding the computational setup, see Windell et al. [100].

An extensive simulation campaign has been generated to match the injection condition measured experimentally in the HPSC. The operating conditions considered for comparison to experimental results are shown in Table SprayCFD-1.

*Table 3.1: Operating conditions of the simulation campaign for the 8-hole SprayG and 5-hole optimized injector.*

Operating condition	#1	#2	#3	#4
$T_{Inj}$ (K)	293	363	293	363
$P_{amb}$ (bar)	0.5	0.5	6.852	6.852
$T_{amb}$ (K)	293	363	293	363
<b>SH degree</b>	0.06	0.01	0.89	0.20

Note that for the 8-hole Spray-G injector, the injection pressure was  $P_{inj} = 200$  bar, and for the optimized 5-hole injector the injection pressure was  $P_{inj} = 170$  bar. The high-fidelity nozzle flow simulations captured the response of vaporizing LPG spray to the ambient conditions (e.g.  $P_{amb}$ ,  $T_{amb}$  and super-heat degree) and its behavior has been translated to the Lagrangian injection model.

In absence of accurate and reliable flash-boiling vaporization models for Lagrangian sprays, the enhanced atomization and vaporization are obtained by modifying the aerodynamic breakup constants to replicate the phenomena measured experimentally in the high-pressure spray-chamber (HPSC). The simulation has been compared to the HPSC measurements in terms of liquid and vapor morphology through consistent replication of schlieren and Mie-Scattering data, obtaining reasonable agreement across a wide range of operating conditions. Full collapse of the plumes is obtained for flashing sprays and a more conventional spray behavior is report when  $P_{amb}$  is higher. The influence of the injector geometry is captured in the injection dynamics and Lagrangian spray models for the CFD software CONVERGE-3.0 [108] have been generated to be incorporated in engine simulations.

In the software CONVERGE v3.0 [108], the Kelvin-Helmholtz (KH) and Rayleigh-Taylor (RT) model are utilized for shear flow breakup. The KH instability in fluid dynamics is important for shear flows in which there is a velocity difference that occurs across the interface of two liquids, and the model is implemented in CONVERGE to simulate liquid jet breakup. The RT instability is an instability related the interface between two fluids of different densities and is relevant for droplet breakup behavior. The combined KH-RT breakup model utilizes these two liquid and gas instability mechanisms to simulate liquid jet breakup, and the model assumes that only KH instabilities are responsible for droplet breakup within a characteristic breakup length  $L_b$ , and that both KH & RT mechanisms contribute to droplet breakup beyond  $L_b$ . Figure 3.26 shows a diagram illustrating the characteristic breakup length and models controlling the droplet breakup.

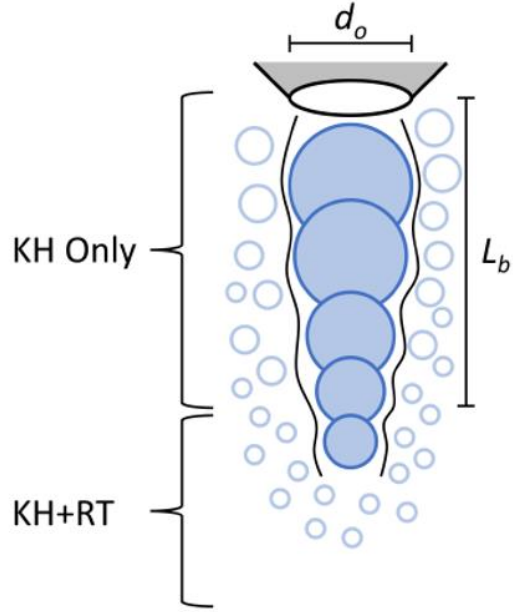


*Figure 3.26: Illustration [108] showing the characteristic breakup length and regime in which different instability models control droplet breakup.*

The important parameters are therefore the characteristic breakup length  $L_b$ , in which only KH instabilities are responsible for droplet breakup  $L_b$  as given in Equation (3.1) and the KH breakup length  $L_{KH}$  as expressed in Equation (3.2)

$$L_b = C_{bl} \sqrt{\frac{\rho_l}{\rho_g} d_0} \quad (3.1)$$

$$L_{KH} = B_1 \sqrt{\frac{\rho_l}{\rho_g} r_0} \quad (3.2)$$

By controlling the aerodynamic breakup models, the simulations are able to capture the behavior of the vapor phase and the overall morphology of the spray, reproducing the sudden plume-plume collapse driven by flash-boiling. The detailed analysis of the breakup dynamics and near-spray vapor diffusion performed improved the characterization of the liquid phase, and the limitations on the RT breakup which strongly drives atomization imposed by a breakup length found that the KH-RT instability-driven model

better represents the spray behavior. An optimal setup was determined based on relevant operating conditions to improve the characterization of the evolution of the liquid phase. The model parameters were chosen based on the superheat degree, computed as provided in Equation (1.2) so as to capture the strong spray collapse trends observed for propane which dependence on fuel temperature  $T_{inj}$ . For cases in which the superheat degree was high (as for operating conditions #1 & #2), parameters chosen for the RT breakup model time constant and model size constant corresponded to a “extreme flashing” scenario. For cases in which the superheat degree was low (as for operating conditions #3 & #4), parameters chosen for the model corresponded to a “moderate” flashing scenario. The time and model size constant parameters for the RT model utilized in the CFD simulation campaign are shown in Table 3.2.

*Table 3.2: RT breakup model parameters for the Lagrangian spray simulations developed for propane.*

RT Breakup Model	Time Constant	Model Size Constant
Non-extreme flashing	1.0	0.6
Extreme flashing	0.1	0.25

A sensitivity study on the aerodynamic breakup model parameters involving the breakup time constant  $B_1$  and the RT breakup length constant  $C_{bl}$  was performed. In general, the KH breakup time constant and RT breakup length constant need to be tuned together for accurate prediction of vaporizing sprays, such that  $C_{bl} = \frac{B_1}{2}$ . Results found that by tuning the KH breakup time constant  $B_1$  and RT breakup length constant  $C_{bl}$  together, an accurate prediction of vaporizing sprays can be achieved through control of the flash-boiling effects. The specific model constants correspond to appropriate settings based on operating condition, mainly driven by ambient pressure and fuel temperature, where lower ambient pressure with higher fuel temperature experiences stronger flash-boiling phenomena.

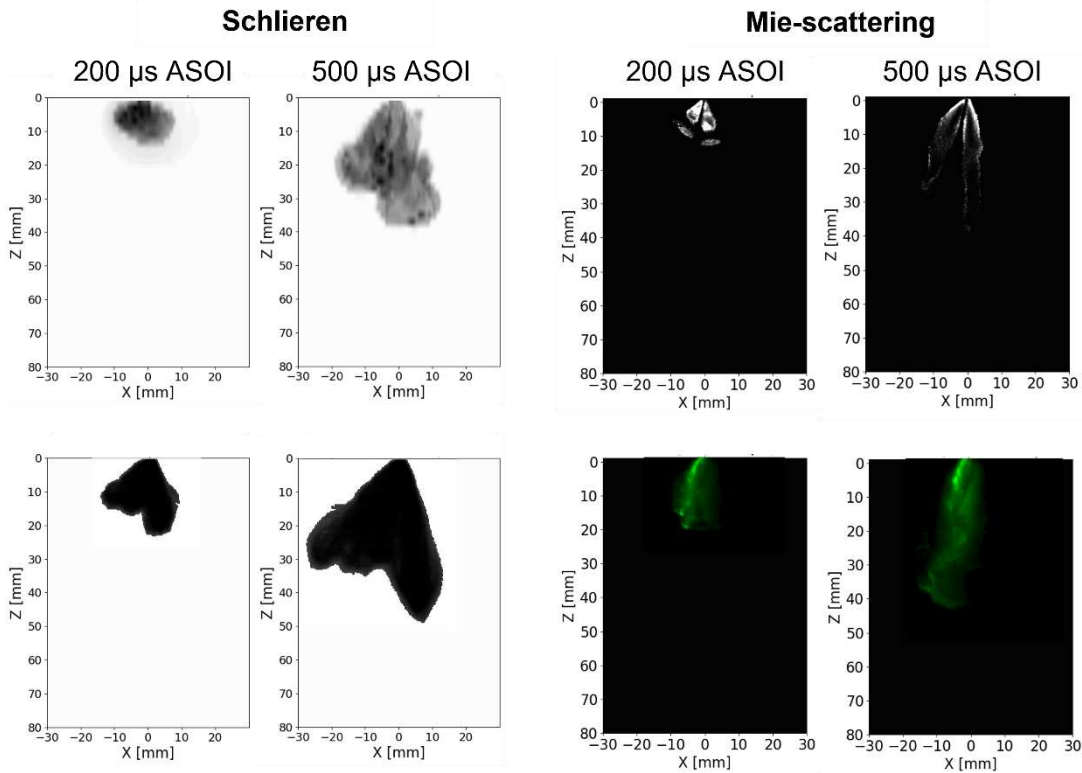


Figure 3.27: Results for the optimized 5-hole injector shown for “flashing” conditions (corresponding to operating conditions #1) for (top) CFD and (bottom) experiments.

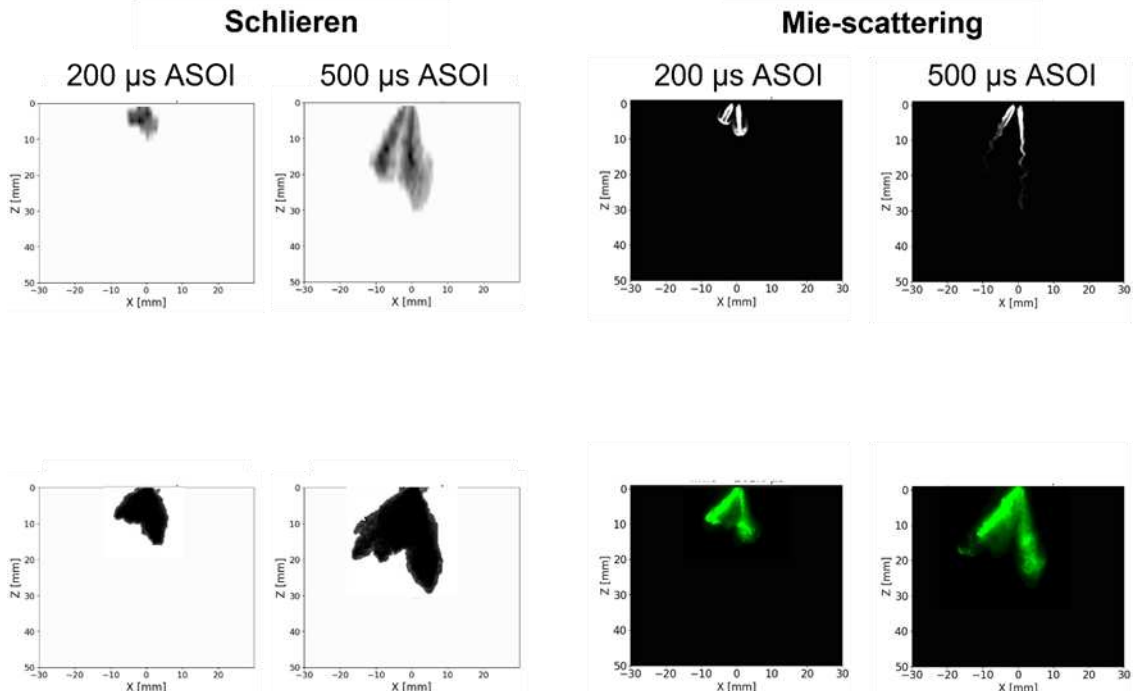


Figure 3.28: Results for the optimized 5-hole injector shown for “sub-cooled” conditions (corresponding to operating conditions #3) for (top) CFD and (bottom) experiments.

By focusing on an extreme condition in which the influence of the vaporization propensity is reflected in the high temperature of the fuel, the KH-RT model breakup setup from the Spray-G setup was implemented, with the model constants breakup time constant  $B_1$  and the RT breakup length constant  $C_{bl}$  determined by operating conditions. It was found that the KH-RT model breakup parameters  $B_1$  and  $C_{bl}$  only needed to be controlled for the simulations with a in which flash boiling dominates, thus utilizing the “extreme flashing” model parameters. The KH breakup time constant  $B_1 = 1$  and RT model breakup length constant  $C_{bl} = 0.5$  was found to work well in reproducing the flash-boiling driven atomization for the operating conditions tested here. Figure 3.27 shows the Mie and Schlieren comparison between CFD and experimental results for the flashing case (operating condition #1) and the optimized 5-hole injector, and Figure 3.28 shows the results for the sub-cooled case (operating condition #3). It can be seen that the CFD results are able to predict the spray morphology well as shown by a comparison in Schlieren imaging, as well as the liquid phase results, particularly in controlling the aggressive vaporization that dominates for extreme flashing conditions.

## CHAPTER 4 - CONCLUSIONS AND FUTURE WORK

### 4.1. Conclusions

In this study, iso-octane and propane, serving as surrogates for gasoline and LPG, were experimentally tested and computationally simulated for direct injections at a wide range of conditions corresponding to early injection, and part load, throttled conditions as seen in a direct injected spark ignited engine. These engine-like conditions were reproduced by controlling fuel and ambient temperatures and pressures, and the governing mechanisms of liquid and vaporous fuel sprays were examined in a quasi-quiescent, optically capable, HPSC. The results from the experimental spray diagnostics fed the numerical simulations for its model validation, selection, and tuning.

Optical imaging techniques revealed that iso-octane was minimally affected by temperature and pressure and exhibited a conventional spray pattern specifically, wider spray angles and explicit plume-to-plume distinctions. Iso-octane's penetration lengths were inversely proportional to both pressure and temperature, and a similar trend on pressure dependence was observed for propane. Propane at colder conditions had wider spray angles, minimal collapse, and some plume-to-plume distinction, whereas these features were completely absent at hotter conditions, signifying the strong dependence of temperature or super-heat degree of propane on spray formation. Propane's spray propagation was fed by its flash boiling, spray collapse, and high degree of vaporization, resulting in a direct proportionality of propane's penetration length to temperature. These unique features of propane and its variation from iso-octane's spray pattern, contribute to its classification as an unconventional spray.

Best practices from standard gasoline direct injection models were imported in the framework and modified to capture the strongly collapsing propane spray dynamics. The simulations were based on a Lagrangian spray framework, and the characteristics of the injected droplets were modified according to higher-resolution multi-phase nozzle flow results. The simulation results were found to be sensitive to cone and inclusion angles of the blob injector, hence, the spray morphologies were mapped for various  $C_A$  and  $I_A$ , and the final selection was made by comparison with the experimental results. The current work

represents a first assessment of the capability of the commonly available models for engine-spray simulations and highlight the fact that, despite the reasonable agreement obtained in the fuel vapor morphology, the representation of the liquid phase lacks accuracy. The addition of the flash-boiling vaporization terms on the phase-change modeling further reduces the liquid penetration without improving the representation of the vapor dynamics. For propane, both G3C and G3 conditions, are extreme flashing conditions: the super heat degree, defined in Equation (1.2), is respectively 0.12 and 0.03, and the empirical correlation tends to over-estimate the phase-change.

## 4.2. Future Work

To enhance the distinction between vapor and liquid regions of propane, the current planar Mie scattering imaging will be coupled with planar laser induced fluorescence, carried out using acetone as a tracer, to increase resolution and obtain further insight into the mixing processes of propane. Higher ambient pressure conditions will also be incorporated into the data set, to explore the high load, homogenous charge, early injection and part load/idle, stratified charge, late injection conditions observed in DISI engines, for various commercially available GDI injectors, with and without modified nozzle geometries.

The simulation framework is currently being extended introducing more information from high-resolution nozzle flow simulations, such as vapor formation in the nozzle, estimation of the initial droplet size distribution, and detailed multi-phase flow momentum initialization. Ultimately the one-way coupling approach [115] will be implemented. Moreover, since flash-boiling dominates the dynamics of the spray, in terms of atomization and phase-change, detailed modeling of the phase-change will be addressed to predict the LPG and liquid propane injection. Finally, processing of the CFD results will be improved including the fuel dependency on the scattered light and possible dense fuel vapor effects to allow for more meaningful comparison to experimental data. The efforts from the experimental and numerical spray campaign for LPG, will aid to identify an optimal DI nozzle geometry for homogenous and stratified charge mixture, and to find the ideal coupling between the in-cylinder motion, and timed injections events, using robust spray models to serve the overarching goal of achieving near diesel engine efficiency for a Cummins X-15 heavy-duty diesel engine using LPG.

## BIBLIOGRAPHY

- [1] K. Kim, J. Kim, S. Oh, C. Kim, and Y. Lee, “Evaluation of injection and ignition schemes for the ultra-lean combustion direct-injection LPG engine to control particulate emissions,” *Appl Energy*, vol. 194, pp. 123–135, 2017.
- [2] P. Jadun, C. McMillan, D. Steinberg, M. Muratori, L. Vimmerstedt, and T. Mai, “Electrification futures study: End-use electric technology cost and performance projections through 2050,” National Renewable Energy Lab.(NREL), Golden, CO (United States), 2017.
- [3] “FACT SHEET: President Biden Sets 2030 Greenhouse Gas Pollution Reduction Target Aimed at Creating Good-Paying Union Jobs and Securing U.S. Leadership on Clean Energy Technologies | The White House.” Accessed: Nov. 05, 2023. [Online]. Available: <https://www.whitehouse.gov/briefing-room/statements-releases/2021/04/22/fact-sheet-president-biden-sets-2030-greenhouse-gas-pollution-reduction-target-aimed-at-creating-good-paying-union-jobs-and-securing-u-s-leadership-on-clean-energy-technologies/>
- [4] J. Lacey *et al.*, “Optical characterization of propane at representative spark ignition, gasoline direct injection conditions,” SAE Technical Paper, 2016.
- [5] S. Rengarajan, Z. Liu, C. Lerin, J. Stetter, V. Narang, and C. Lana, “LPG direct injection engine for medium duty trucks,” SAE Technical Paper, 2020.
- [6] V. Pradeep and R. P. Sharma, “Evaluation of performance, emission and combustion parameters of a CI engine fuelled with bio-diesel from rubber seed oil and its blends,” SAE Technical Paper, 2005.
- [7] P. Kotsopoulos, R. Papagiannakis, P. Tsakalou, I. Gazinou, and E. Yfantis, “Experimental investigation concerning the effect of the use of biodiesel and F-34 (JP-8) aviation fuel on performance and emissions of a DI diesel engine,” SAE Technical Paper, 2007.
- [8] H. Kojima, E. Takahashi, T. Tsujimura, H. Furutani, and T. Kashiwazaki, “Acetone PLIF measurements of temperature and concentration distributions in a high-temperature and high-pressure spray,” SAE Technical Paper, 2015.

- [9] “Petroleum & Other Liquids - U.S. Energy Information Administration (EIA).” Accessed: Nov. 05, 2023. [Online]. Available: <https://www.eia.gov/petroleum/index.php>
- [10] K. J. Morganti, T. M. Foong, M. J. Brear, G. da Silva, Y. Yang, and F. L. Dryer, “The research and motor octane numbers of liquefied petroleum gas (LPG),” *Fuel*, vol. 108, pp. 797–811, 2013.
- [11] “Alternative Fuels Data Center: Fuel Properties Comparison.” Accessed: Nov. 05, 2023. [Online]. Available: <https://afdc.energy.gov/fuels/properties>
- [12] “Alternative Fuels Data Center: Propane Basics.” Accessed: Nov. 05, 2023. [Online]. Available: [https://afdc.energy.gov/fuels/propane\\_basics.html](https://afdc.energy.gov/fuels/propane_basics.html)
- [13] J. Lacey *et al.*, “Flash vaporization of propane in an optically accessible, directly injected engine,” *International Journal of Engine Research*, vol. 22, no. 2, pp. 685–696, 2021.
- [14] A. Kalwar and A. Agarwal, “Overview, Advancements and Challenges in Gasoline Direct Injection Engine Technology,” 2020, pp. 111–147. doi: 10.1007/978-981-15-0368-9\_6.
- [15] Y. Huang, G. Hong, and R. Huang, “Investigation to charge cooling effect and combustion characteristics of ethanol direct injection in a gasoline port injection engine,” *Appl Energy*, vol. 160, pp. 244–254, 2015.
- [16] C. Baumgarten, *Mixture formation in internal combustion engines*. Springer Science & Business Media, 2006.
- [17] F. Poursadegh, “An Experimental and Theoretical Investigation of Direct Fuel Injection,” DISS, 2017.
- [18] F. Zhao, M.-C. Lai, and D. L. Harrington, *Automotive spark-ignited direct-injection gasoline engines*. Elsevier, 2000.
- [19] M. A. Kalam and H. H. Masjuki, “An experimental investigation of high performance natural gas engine with direct injection,” *Energy*, vol. 36, no. 5, pp. 3563–3571, 2011.
- [20] R. D. Oza and J. F. Sinnamon, “An experimental and analytical study of flash-boiling fuel injection,” *SAE transactions*, pp. 948–962, 1983.

- [21] N. Ashgriz, *Handbook of atomization and sprays: theory and applications*. Springer Science & Business Media, 2011.
- [22] E. Sher, T. Bar-Kohany, and A. Rashkovan, “Flash-boiling atomization,” *Prog Energy Combust Sci*, vol. 34, no. 4, pp. 417–439, 2008.
- [23] B. S. Park and S. Y. Lee, “An experimental investigation of the flash atomization mechanism,” *Atomization and sprays*, vol. 4, no. 2, 1994.
- [24] R. D. Oza, “On the mechanism of flashing injection of initially subcooled fuels,” 1984.
- [25] J. Serras-Pereira, Z. Van Romunde, P. G. Aleiferis, D. Richardson, S. Wallace, and R. F. Cracknell, “Cavitation, primary break-up and flash boiling of gasoline, iso-octane and n-pentane with a real-size optical direct-injection nozzle,” *Fuel*, vol. 89, no. 9, pp. 2592–2607, 2010.
- [26] B. A. Sforzo, A. Tekawade, K. Matusik, A. Kastengren, J. Ilavsky, and C. Powell, “X-ray Characterization and Spray Measurements of ECN Spray G Using Alternative Fuels at Flashing Conditions,” 2019.
- [27] H. Guo, L. Nocivelli, and R. Torelli, “Numerical study on spray collapse process of ECN spray G injector under flash boiling conditions,” *Fuel*, vol. 290, p. 119961, 2021.
- [28] “Parametric Variation – Engine Combustion Network.” Accessed: Nov. 05, 2023. [Online]. Available: <https://ecn.sandia.gov/gasoline-spray-combustion/target-condition/spray-g-parametric-variation/>
- [29] J. Lacey *et al.*, “Generalizing the behavior of flash-boiling, plume interaction and spray collapse for multi-hole, direct injection,” *Fuel*, vol. 200, pp. 345–356, 2017.
- [30] D. K. Huzel and D. H. Huang, “Design of liquid propellant rocket engines,” 1967.
- [31] P. P. Nair, A. Suryan, and H. D. Kim, “Computational study on flow through truncated conical plug nozzle with base bleed,” *Propulsion and Power Research*, vol. 8, no. 2, pp. 108–120, 2019.
- [32] H. Guo, L. Nocivelli, R. Torelli, and S. Som, “Towards understanding the development and characteristics of under-expanded flash boiling jets,” *International Journal of Multiphase Flow*, vol. 129, p. 103315, 2020.

- [33] L. Nocivelli, J. Yan, K. Saha, G. M. Magnotti, C.-F. Lee, and S. Som, “Effect of ambient pressure on the behavior of single-component fuels in a gasoline multi-hole injector,” in *Internal Combustion Engine Division Fall Technical Conference*, American Society of Mechanical Engineers, 2019, p. V001T02A012.
- [34] W. Zeng, M. Xu, M. Zhang, Y. Zhang, and D. J. Cleary, “Macroscopic characteristics for direct-injection multi-hole sprays using dimensionless analysis,” *Exp Therm Fluid Sci*, vol. 40, pp. 81–92, 2012.
- [35] M. Mojtabi, N. Chadwick, G. Wigley, and J. Helie, “The effect of flash boiling on break up and atomization in GDI sprays,” in *Proceedings of the 22nd European Conference on Liquid Atomization and Spray Systems. ILASS Europe. Como Lake, Italy*, 2008, pp. 8–10.
- [36] F. Zhao, D. L. Harrington, and M.-C. Lai, *Automotive gasoline direct-injection engines*. SAE International, 2002.
- [37] R. D. Reitz, “A photographic study of flash-boiling atomization,” *Aerosol Science and Technology*, vol. 12, no. 3, pp. 561–569, 1990.
- [38] G. Delay, R. Bazile, G. Charnay, and H. Nuglisch, “Temporal dependency of air entrainment to liquid flow rate variations for gasoline direct injection sprays,” in *Temporal dependency of air of laser tecnicas to fluid mechanics. International Symposia on Applications of Laser Techniques to Fluid Mechanics. Lisbon*, Citeseer, 2004.
- [39] L. Allocca and G. Valentino, “Droplet Size and Velocity Distributions of a Transient Hollow-Cone Spray for GDI Engines,” *Part Part Syst Charact*, vol. 18, no. 5-6, pp. 262–270, 2001.
- [40] F. Poursadegh *et al.*, “On the phase and structural variability of directly injected propane at spark ignition engine conditions,” *Fuel*, vol. 222, pp. 294–306, 2018.
- [41] J. Mizia, “Micro-liter Quantity Pilot Injection Studies in a Constant Volume Combustion Test Chamber,” 2003.

- [42] M. A. Ratcliff *et al.*, “Impact of ethanol blending into gasoline on aromatic compound evaporation and particle emissions from a gasoline direct injection engine,” *Appl Energy*, vol. 250, pp. 1618–1631, 2019.
- [43] A. G. Hockett, G. Hampson, and A. J. Marchese, “Natural gas/diesel RCCI CFD simulations using multi-component fuel surrogates,” *International Journal of Powertrains*, vol. 6, no. 1, pp. 76–108, 2017.
- [44] H. S. Johnston and J. Heicklen, “Photochemical Oxidations. III. Acetone,” *J Am Chem Soc*, vol. 86, no. 20, pp. 4249–4254, 1964.
- [45] G. A. Hussein, A. K. Jasuja, and R. S. Fletcher, “ASME Gas Turbine Division (1982),” paper 82-GT-25.
- [46] A. J. Yule, C. AhSeng, P. G. Felton, A. Ungut, and N. A. Chigier, “A laser tomographic investigation of liquid fuel sprays,” *Symposium (International) on Combustion*, vol. 18, no. 1, pp. 1501–1510, 1981, doi: [https://doi.org/10.1016/S0082-0784\(81\)80152-X](https://doi.org/10.1016/S0082-0784(81)80152-X).
- [47] A. R. Chraplyvy, “Nonintrusive measurements of vapor concentrations inside sprays,” *Appl Opt*, vol. 20, no. 15, pp. 2620–2624, 1981.
- [48] Y. Li, H. Guo, Z. Zhou, Z. Zhang, X. Ma, and L. Chen, “Spray morphology transformation of propane, n-hexane and iso-octane under flash-boiling conditions,” *Fuel*, vol. 236, pp. 677–685, 2019.
- [49] L. A. Melton, “Spectrally separated fluorescence emissions for diesel fuel droplets and vapor,” *Appl Opt*, vol. 22, no. 14, pp. 2224–2226, 1983.
- [50] R. Alsulami, S. Lucas, M. Hageman, M. Knadler, J. M. Quinlan, and B. Windom, “Coupling effects of physical and chemical properties on jet fuel spray flame blowout,” *Proceedings of the Combustion Institute*, vol. 38, no. 2, pp. 3333–3341, 2021.
- [51] A. Korpel, D. Mehrl, and H. H. Lin, “Schlieren imaging of sound fields,” in *IEEE 1987 Ultrasonics Symposium*, IEEE, 1987, pp. 515–518.

- [52] S. A. Brown, L. Greenbaum, S. Shtukmaster, Y. Zadok, S. Ben-Ezra, and L. Kushkuley, “Characterization of nonthermal focused ultrasound for noninvasive selective fat cell disruption (lysis): technical and preclinical assessment,” *Plast Reconstr Surg*, vol. 124, no. 1, pp. 92–101, 2009.
- [53] C. V Raman and N. S. Nagendra Nathe, “The diffraction of light by high frequency sound waves: Part I.,” in *Proceedings of the Indian Academy of Sciences-Section A*, Springer, 1935, pp. 406–412.
- [54] G. S. Settles, *Schlieren and shadowgraph techniques: visualizing phenomena in transparent media*. Springer Science & Business Media, 2001.
- [55] “Laminar–turbulent transition - Wikipedia.” Accessed: Nov. 05, 2023. [Online]. Available: [https://en.wikipedia.org/wiki/Laminar%20%93turbulent\\_transition](https://en.wikipedia.org/wiki/Laminar%20%93turbulent_transition)
- [56] “Matt Staymates schlieren composite.” Accessed: Nov. 05, 2023. [Online]. Available: <https://www.nist.gov/image/matt-staymates-schlieren-composite>
- [57] P. Prasanna Simha and P. S. Mohan Rao, “Universal trends in human cough airflows at large distances,” *Physics of Fluids*, vol. 32, no. 8, 2020.
- [58] Y. L. Qi, B. Y. Xu, and S. L. Cai, “An application of digital image processing techniques to the characterization of liquid petroleum gas (LPG) spray,” *Meas Sci Technol*, vol. 17, no. 12, p. 3229, 2006.
- [59] D. W. Hahn, “Light Scattering Theory,” 2009.
- [60] G. Mie, “Beiträge zur Optik trüber Medien, speziell kolloidaler Metallösungen,” *Ann Phys*, vol. 330, no. 3, pp. 377–445, 1908.
- [61] J. A. Stratton, *Electromagnetic Theory*. in International series in physics. McGraw-Hill book Company, Incorporated, 1941. [Online]. Available: <https://books.google.com/books?id=nBIJAQAAIAAJ>
- [62] S. T. Surjikov, “MIE SCATTERING,” *A-to-Z Guide to Thermodynamics, Heat and Mass Transfer, and Fluids Engineering*, Jun. 2011, doi: 10.1615/ATOZ.M.MIE\_SCATTERING.
- [63] Z. Ye, X. Jiang, and Z. Wang, “Measurements of Particle Size Distribution Based on Mie Scattering Theory and Markov Chain Inversion Algorithm.,” *J. Softw.*, vol. 7, no. 10, pp. 2309–2316, 2012.

- [64] S. Barnhart and S. Gunasekaran, “Design and Development of a Coherent Detection Rayleigh Doppler Lidar System for Use as an Alternative Velocimetry Technique in Wind Tunnels,” 2020. doi: 10.13140/RG.2.2.32670.15688.
- [65] S. E. Parrish, “Evaluation of liquid and vapor penetration of sprays from a multi-hole gasoline fuel injector operating under engine-like conditions,” *SAE Int J Engines*, vol. 7, no. 2, pp. 1017–1033, 2014.
- [66] B. D. Ritchie, J. Seitzman, T. Lieuwen, J. Jagoda, A. Glezer, and S. Menon, “Quantitative Acetone PLIF Measurements of Jet Mixing with Synthetic Jet Actuators.” Georgia Institute of Technology, Apr. 11, 2006. Accessed: Nov. 05, 2023. [Online]. Available: <http://hdl.handle.net/1853/10536>
- [67] G. Kychakoff, R. D. Howe, R. K. Hanson, and J. C. McDaniel, “Quantitative visualization of combustion species in a plane,” *Appl Opt*, vol. 21, no. 18, pp. 3225–3227, 1982.
- [68] C. S. Goldenstein, V. A. Miller, and R. K. Hanson, “Infrared planar laser-induced fluorescence with a CW quantum-cascade laser for spatially resolved CO<sub>2</sub> and gas properties,” *Applied Physics B*, vol. 120, no. 2, pp. 185–199, 2015.
- [69] S. Wang and R. K. Hanson, “Quantitative 2-D OH thermometry using spectrally resolved planar laser-induced fluorescence,” *Opt Lett*, vol. 44, no. 3, pp. 578–581, 2019.
- [70] R. E. Hunt and W. A. Noyes Jr, “Photochemical studies. XXXIX. A further study of the fluorescence of acetone,” *J Am Chem Soc*, vol. 70, no. 2, pp. 467–476, 1948.
- [71] J. Heicklen, “The fluorescence and phosphorescence of biacetyl vapor and acetone vapor1,” *J Am Chem Soc*, vol. 81, no. 15, pp. 3863–3866, 1959.
- [72] J. Heicklen and W. A. Noyes Jr, “The Photolysis and Fluorescence of Acetone and Acetone-Biacetyl Mixtures1,” *J Am Chem Soc*, vol. 81, no. 15, pp. 3858–3863, 1959.
- [73] G. M. Breuer and E. K. C. Lee, “Fluorescence decay times of cyclic ketones, acetone, and butanal in the gas phase,” *J Phys Chem*, vol. 75, no. 7, pp. 989–990, 1971.

- [74] A. Gandini and P. A. Hackett, “Electronic relaxation processes in acetone and 1, 1, 1-trifluoroacetone vapor and the gas phase recombination of the acetyl radical at 22. degree. C,” *J Am Chem Soc*, vol. 99, no. 19, pp. 6195–6205, 1977.
- [75] M. Baba and I. Hanazaki, “The S1, 1A2 (n, π\*) state of acetone in a supersonic nozzle beam. Methyl internal rotation,” *Chem Phys Lett*, vol. 103, no. 2, pp. 93–97, 1983.
- [76] G. D. Greenblatt, S. Ruhman, and Y. Haas, “Fluorescence decay kinetics of acetone vapour at low pressures,” *Chem Phys Lett*, vol. 112, no. 3, pp. 200–206, 1984.
- [77] R. A. Copeland and D. R. Crosley, “Radiative, collisional and dissociative processes in triplet acetone,” *Chem Phys Lett*, vol. 115, no. 4–5, pp. 362–368, 1985.
- [78] A. Costela, M. T. Crespo, and J. M. Figuera, “Laser photolysis of acetone at 308 nm,” *Journal of photochemistry*, vol. 34, no. 2, pp. 165–173, 1986.
- [79] H. Zuckermann, B. Schmitz, and Y. Haas, “Dissociation energy of an isolated triplet acetone molecule,” *J Phys Chem*, vol. 92, no. 17, pp. 4835–4837, 1988.
- [80] H. Zuckermann, B. Schmitz, and Y. Haas, “Acetone photophysics in seeded supersonic molecular beams,” *J Phys Chem*, vol. 93, no. 10, pp. 4083–4091, 1989.
- [81] H. Zuckermann, B. Schmitz, and Y. Haas, “The radiative lifetime of acetone: resolution of an apparent discrepancy,” *Chem Phys Lett*, vol. 151, no. 4–5, pp. 323–327, 1988.
- [82] M. J. G. Borge, J. M. Figuera, and J. Luque, “Study of the emission of the excited acetone vapour at intermediate pressures,” *Spectrochim Acta A*, vol. 46, no. 4, pp. 617–621, 1990.
- [83] A. Lozano, B. Yip, and R. K. Hanson, “Acetone: a tracer for concentration measurements in gaseous flows by planar laser-induced fluorescence,” *Exp Fluids*, vol. 13, no. 6, pp. 369–376, 1992.
- [84] A. Lozano, *Laser-excited luminescent tracers for planar concentration measurements in gaseous jets*. Stanford University, 1992.
- [85] D. B. Olsen and B. D. Willson, “The impact of cylinder pressure on fuel jet penetration and mixing,” in *Internal Combustion Engine Division Fall Technical Conference*, 2002, pp. 233–240.

- [86] J. M. Seitzman and R. K. Hanson, “Planar fluorescence imaging in gases,” *Instrumentation for flows with combustion*, p. 405, 1993.
- [87] J. P. Crimaldi, “Planar laser induced fluorescence in aqueous flows,” *Exp Fluids*, vol. 44, pp. 851–863, 2008.
- [88] T. Ueda, M. Shimura, M. Tanahashi, and T. Miyauchi, “Measurement of three-dimensional flame structure by combined laser diagnostics,” *Journal of mechanical science and technology*, vol. 23, pp. 1813–1820, 2009.
- [89] F. Grisch and M. Orain, “Role of Planar Laser-Induced Fluorescence in Combustion Research.,” *Aerospace Lab*, no. 1, p. p-1, 2009.
- [90] T. Zhao, S. Tan, X. Wang, Y. Yang, and R. Wang, “Application of planar laser-induced fluorescence to measurement of concentration field in the downcomer,” in *Proceedings of The 20th Pacific Basin Nuclear Conference: Volume 3*, Springer, 2017, pp. 681–690.
- [91] J. K. Dukowicz, “A particle-fluid numerical model for liquid sprays,” *J Comput Phys*, vol. 35, no. 2, pp. 229–253, 1980.
- [92] C. Price, A. Hamzehloo, P. Aleiferis, and D. Richardson, “Numerical modelling of droplet breakup for flash-boiling fuel spray predictions,” *International Journal of Multiphase Flow*, vol. 125, p. 103183, 2020.
- [93] R. Schlüßler, J. Gürtler, J. Czarske, and A. Fischer, “Planar fuel velocity measurements in the near-nozzle region of a high pressure Diesel injection nozzle,” in *18th International Symposium on the Application of Laser and Imaging Techniques to Fluid Mechanics*, 2016, pp. 1–13.
- [94] J. B. Ghandhi, P. G. Felton, B. F. Gajdeczko, and F. V Bracco, “Investigation of the fuel distribution in a two-stroke engine with an air-assisted injector,” SAE Technical Paper, 1994.
- [95] H. Fujimoto, D. Choi, Y. Shima, and J. Senda, “Two-dimensional imaging of fuel-vapour concentration by use of LIEF technique during mixture formation process in a DI diesel engine,” *Meas Sci Technol*, vol. 13, no. 3, p. 391, 2002.

- [96] R. Payri, J. Gimeno, P. Martí-Aldaravi, and M. Martínez, “Nozzle flow simulation of GDI for measuring near-field spray angle and plume direction,” SAE Technical Paper, 2019.
- [97] P. Rogler, R. Grzeszik, S. Arndt, and M. Aigner, “3D analysis of vapor and liquid phase of GDI injectors using laser induced exciplex fluorescence tomography in a high pressure/high temperature spray chamber,” SAE Technical Paper, 2007.
- [98] P. Downar-Zapolski, Z. Bilicki, L. Bolle, and J. Franco, “The non-equilibrium relaxation model for one-dimensional flashing liquid flow,” *International journal of multiphase flow*, vol. 22, no. 3, pp. 473–483, 1996.
- [99] M. Adachi, V. G. McDonell, D. Tanaka, J. Senda, and H. Fujimoto, “Characterization of fuel vapor concentration inside a flash boiling spray,” SAE Technical Paper, 1997.
- [100] B. Windell *et al.*, “Bulk Spray and Individual Plume Characterization of LPG and Iso-Octane Sprays at Engine-Like Conditions,” Daniel B. Olsen, Colorado State University, 2022.
- [101] P. H. Mesman and B. Veenhuizen, “The spray behavior of liquid LPG at different back pressures during injection in a constant volume chamber,” SAE Technical Paper, 2009.
- [102] B. Mohan, J. Badra, J. Sim, and H. G. Im, “Coupled in-nozzle flow and spray simulation of Engine Combustion Network Spray-G injector,” *International Journal of Engine Research*, vol. 22, no. 9, pp. 2982–2996, 2021.
- [103] J. Hwang, L. Weiss, I. K. Karathanassis, P. Koukouvinis, L. M. Pickett, and S. A. Skeen, “Spatio-temporal identification of plume dynamics by 3D computed tomography using engine combustion network spray G injector and various fuels,” *Fuel*, vol. 280, p. 118359, 2020.
- [104] C. K. Mohapatra *et al.*, “Collaborative investigation of the internal flow and near-nozzle flow of an eight-hole gasoline injector (Engine Combustion Network Spray G),” *International Journal of Engine Research*, vol. 24, no. 6, pp. 2297–2314, 2023.
- [105] L. Sileghem *et al.*, “Laminar burning velocity of gasoline and the gasoline surrogate components iso-octane, n-heptane and toluene,” *Fuel*, vol. 112, pp. 355–365, 2013.

- [106] L. Allocca *et al.*, “ECN Spray G injector: assessment of numerical modeling accuracy,” SAE Technical Paper, 2018.
- [107] A. Montanaro, L. Allocca, and M. Lazzaro, “Iso-octane spray from a GDI multi-hole injector under non-and flash boiling conditions,” SAE Technical Paper, 2017.
- [108] K. J. Richards, P. K. Senecal, and E. Pomraning, “CONVERGE 3.0,” *Convergent Science, Madison, WI*, 2021.
- [109] L. Nocivelli *et al.*, “Analysis of the spray numerical injection modeling for gasoline applications,” SAE Technical Paper, 2020.
- [110] L. Nocivelli *et al.*, “Comparison Between a Center-Mounted and a Side-Mounted Injector for Gasoline Applications: A Computational Study,” in *Internal Combustion Engine Division Fall Technical Conference*, American Society of Mechanical Engineers, 2020, p. V001T05A007.
- [111] Z. Yue, M. Battistoni, and S. Som, “Spray characterization for engine combustion network Spray G injector using high-fidelity simulation with detailed injector geometry,” *International Journal of Engine Research*, vol. 21, p. 146808741987239, Sep. 2019, doi: 10.1177/1468087419872398.
- [112] J. C. Beale and R. D. Reitz, “Modeling spray atomization with the Kelvin-Helmholtz/Rayleigh-Taylor hybrid model,” *Atomization and sprays*, vol. 9, no. 6, 1999.
- [113] D. P. Schmidt and C. J. Rutland, “A new droplet collision algorithm,” *J Comput Phys*, vol. 164, no. 1, pp. 62–80, 2000.
- [114] P. K. Senecal *et al.*, “A new parallel cut-cell Cartesian CFD code for rapid grid generation applied to in-cylinder diesel engine simulations,” SAE Technical Paper, 2007.
- [115] S. Quan *et al.*, “A one-way coupled volume of fluid and Eulerian-Lagrangian method for simulating sprays,” in *Internal Combustion Engine Division Fall Technical Conference*, American Society of Mechanical Engineers, 2016, p. V001T06A014.